Czech Technical University in Prague
Faculty of Electrical Engineering
Department of Electromagnetic Field

Measurement of Fast-flying Targets in Near-zone

Doctoral Thesis

Vojtěch Jeník

Prague, August 2017

Ph.D. Programme: Electrical Engineering and Information Technology
Branch of study: Radioelectronics

Supervisor: Doc. Ing. Přemysl Hudec, CSc.

Acknowledgement

I would like to express gratitude to Přemysl Hudec, my supervisor, for his guidance and advices. In addition, I must express my sincere gratitude to colleagues at the Department of Electromagnetic Field for having expanded my horizons in the area of electromagnetic field and many discussions about this topic.

And last but not least, I would like to thank Markéta and my close family for their support and motivating me to accomplish this work.

Declaration

I hereby declare that I have authored this thesis independently, that I have not used other than the declared sources/resources, and that I have explicitly marked all material which has been quoted either literally or by content from the used sources, according to Methodical instructions on ethical principles for writing academic thesis. Moreover I declare that I have not violated any copyrights.

Done in Prague, 28 August 2017

Vojtěch Jeník

Abstract

This thesis deals with the problem of detection, identification and tracking of fast flying objects close to radar sensors, which reflects a current set-up in radar based active defense systems (ADS). Furthermore, a comprehensive noise analysis of CW radar is presented.

Various configurations of CW radar are proposed and evaluated – from multiple installations of identical CW radar sensors to a set of receivers sharing the same HW component (e.g. local oscillator or the whole transmitter) – with the aim of finding the best and simplest possible configuration to fulfill the demanding requirements of ADS. Since the radar sensors are very complicated systems, the best solution cannot be identified without considering individual requirements on the system and available technology (i.e. frequency range, modulation, etc.). Therefore the thesis only concludes the principal properties of the proposed configurations.

Another topic investigates available methods for in-field radar sensor testing and calibration. With regard to various methods and their limitations, the selected solution uses an antenna with an electronically controlled phase shifter and short-end stub.

The last part is dedicated to the comprehensive noise analysis of a homodyne CW radar system with quadrature demodulation, which includes the amplitude and phase noise of local oscillator, noise of linear and quasi-linear RF components and noise of low frequency circuits. Even though the analysis has been developed on homodyne CW radar, the results are applicable to a much wider range of CW radar sensors. The follow-up research into this topic may be focused on behavior of SDR-based radar systems.

Abstrakt

Disertační práce se věnuje problémům detekce, identifikace a sledování rychle letících objektů v blízké oblasti radarů. Dále je v práci řešena komplexní šumová analýza radaru s kontinuální vlnou.

V práci jsou navrženy a zhodnoceny různé konfigurace radarových senzorů – od jednoduchých s kontinuální vlnou, které jsou instalovány ve větším počtu až po radarové senzory sdílející některé části HW (místní oscilátor nebo celou vysílací část). Cílem je nalézt co nejlepší a zároveň nejjednodušší řešení, které vyhoví náročným podmínkám aktivní ochrany. Vzhledem k tomu, že radarové senzory představují komplikované systémy, je vždy nutné přihlédnout k daným požadavkům a parametrům použitých senzorů (pracovní frekvenci atd.). Tato práce tedy pouze shrnuje klíčové vlastnosti jednotlivých konfigurací.

Další část práce je věnována způsobu testování jednoduchých radarových senzorů před měřením na venkovním pracovišti. Po zvážení několika možností a jejich omezení byla zvolena varianta využívající změnu fáze vlny odražené od antény s elektronickým fázovacím článkem zakončeným zkratovaným vedením. Toto řešení je s dobrými výsledky otestováno dvěma typy radarů (s kontinuální vlnou a s modulovanou kontinuální vlnou).

Poslední část práce je zaměřena na komplexní šumovou analýzu radarového senzoru s kontinuální vlnou s kvadraturní demodulací. Analýza zahrnuje amplitudový a fázový šum místního oscilátoru, šum lineárních a kvazi-lineárních vysokofrekvenčních obvodů a šum nízkofrekvenčních obvodů radaru. Přestože byla analýza odvozena na jednoduchém radaru s kontinuální vlnou, lze ji aplikovat i na mnohem složitější radarové systémy. V dalším výzkumu by bylo možné se zaměřit na radarový systém založený na SDR (softwarově definovaném rádiu).

Contents

Abbreviations

ADC	Analog to Digital Converter
ADS	Active Defense System
ATT	Attenuator
BB	Base Band
BPSK	Binary Phase Shift Keying
BW	Bandwidth
CW	Continuous Wave
DAC	Digital to Analog Converter
DRO	Dielectric Resonator Oscillator
DOA	Direction of Arrival
ESPRIT	Estimation of Signal Classification via Rotational Invariance Technique
FMCW	Frequency Modulated Continuous Wave
I	In-Phase
IF	Intermediate Frequency
IP	Impact Point
LF	Low Frequency
LFA	Low Frequency Amplifier
LNA	Low Noise Amplifier
LO	Local Oscillator
LPF	Low Pass Filter
LWA	Leaky Wave Antenna
MC	Microwave Curtain
MCU	Micro Controller Unit
MISO	Multi-input Single-output
MIX	Mixer
MMIC	Microwave Integrated Circuit
MUSIC	Multiple Signal Classification

OA	Operation Amplifier
PA	Power Amplifier
PLL	Phase-locked Loop
PNS	Pseudo-Noise Sequence
PS	Phase Shifter
PSD	Power Spectrum Density
Q	Quadrature
RCS	Radar Cross Section
RF	Radio Frequency
RFI	Radio Frequency Interference
RX	Receiving / Receiver
SDR	Software Defined Radio
SNR	Signal to Noise Ratio
SR	Surveillance Radar
SW	Switch
TX	Transmitting / Transmitter
USB	Universal Serial Buss
VCO	Voltage Controlled Oscillator
VNA	Vector Network Analyzer

List of Figures

List of Tables

1 Introduction

The detection and measurement of fast-flying objects in near-zone by means of a set of microwave sensors constitutes a typical theoretical problem. It has very important practical applications, out of which probably the most significant one can be found in the military field in the form of defense systems intended to be employed against extremely dangerous anti-armor missiles [1]. The said microwave sensors are part of so-called active defense systems (hereinafter referred to as ADS) developed especially for protection of military vehicles. These defense systems are based on detection and measurement of approaching thread missiles and activation of suitable counter-measures. ADSs have been developed at a number of technical workplaces for at least 20 years. Yet the concerned issues are so extensive and complex that, to date, no ADS has been introduced to a genuinely wide practical employment. Very specific and, to a significant degree perhaps even extreme, requirements applying to detection and measurement sensors are very likely the crucial reasons for this state of affairs.

As it has been already stated, the sensors are supposed to detect approaching thread missile, and within the proper time period, to activate suitable counter-measures. The known ADSs differ significantly in sensors and counter-measures used. Recent developments are focused on ability to react even in a very difficult urban environment, where any attack can arise from very near distances. That is why the sensors should be able to detect thread missiles in a very near-zone (approx. 20-30 m from protected vehicles), trace their trajectories and measure their parameters on the path to immediate distance from the vehicles. Since the flight of thread missiles can be very fast (100 – 1700 m/s), the radar sensors have to be able to operate extremely fast and show a zero blind-zone. In addition, the sensors have to be capable of detecting and measuring targets coming from different angles and distinguishing thread missiles from other targets. According to the gathered information, ADSs that are being developed and tested employ both microwave and optical detection and measurement sensors. Optical sensors can provide a very good resolution and precise measurement of many important parameters, but can show substantial difficulties in the case of dense dust or heavy rain. On the other hand, microwave sensors can be very effectively resistant to dust and rain, yet in general, they suffer from poor resolution. Optimal choice of sensors, processing of their output signals and coordination of their functions in very short time represent other significant requirements.

1.1 State-of-the-art

1.1.1 CW Doppler radar

Since the concerned targets do not radiate any electromagnetic field in the microwave region, they have to be irradiated by an external source if intended to be detected and measured. As a result, the required sensors have to be based on a standard radar structure (transmitter + coherent receiver). In the microwave field, there are two basic types of radar structures — pulse radars and CW radars. Given that pulse radar show non-negligible blind-zones, CW radars were chosen as

the most suitable structures. Indeed, the range of CW radar structures is wider. It involves, *inter alia*, basic analog radars, digitally-modulated radars and FMCW radars. As all more complex types are based on basic analog structures, the latter were chosen for initial development steps and tests [2-4]. Apart from the instantaneous reaction and zero blind-zone, the analog CW radar structure is relatively simple and provides signals with frequency equal to the Doppler frequency shift at its output. It is, therefore, able to measure velocity of moving targets and to distinguish fast moving ones from stationary or slow moving objects. Nevertheless, it is vital to take into account that pure analog CW radars have only limited detection ranges and are unable to measure sensor-to-target distances. Yet it is shown that these relatively simple sensors show many positive features and are widely applicable to detection and measurement of moving objects.

1.1.2 Moving Target Simulator for CW Radar Sensors

The development of CW radar sensors is demanding as to the quality of equipment, which can be used for testing of such sensors. Given that CW radars are immune to static targets, we needed equipment that could simulate defined RCS at predefined velocities in ranges from ones to hundreds of meters per second. For testing a sensor with I/Q demodulation, the simulated velocities should be both positive and negative, which put demands on the testing device regarding the spectral purity. The testing device is further referred to such as calibrator, because it is used for radar calibration.

Currently, various radar testing equipment are commercially available (see Fig. 1.1). However, a signal coherency required by radar front ends is highly demanding in terms of the testing equipment, which is reflected in their considerable prices. Moreover, this type of equipment is usually difficult to set-up (or even requires days of programming to provide correct functionality) and excludes antennas from the test set-up. On the other hand, such equipment has functions that are not needed for our purposes. All arguments mentioned above resulted in searching for a simple and less expensive solution.

Fig. 1.1 Radar testing equipment (signal analyzer + signal generator) from Gigatronix.

After the search for a simple radar testing device capable of providing single target simulation, we ended up finding the device consisting of a revolving helix [5], which represented the only available solution. Among others, its major disadvantages involved low simulated v_r values, high price and dissatisfactory level of stability and reliability.

1.1.3 Noise Analysis of CW Radar

Although there are many publications dealing with the radar noise analysis (see references [6-9]), they mostly refer merely to the noise of linear microwave components or just add some extra noise power for non-linear effects. In fact, none of those descriptions can be used for complete analysis and synthesis of the subjective CW radar sensors.

To the best knowledge of thesis author, there are only three papers dedicated to the impact of local oscillator noise on the noise power at radar receiver analogue output; see [10-12]. They provide a certain insight into the oscillator noise, but the scope of results application is limited. Due to this fact, a substantial effort was made to derive a more complex noise analysis of the respective radar types.

1.2 Dissertation Goals

This thesis further extends the already undertaken research focused on initial ADS development (see e.g. [2-4]). The complexity of the topic leads to define three different areas of the research; each of them is treated separately in one chapter.

The first research area is focused on various radar system concepts and evaluates their capabilities regarding fast object detection in distances close to the sensor. The cooperation of asynchronous CW radar sensors as well as multi-input radar sensors with coherent signal processing is assessed and conclusions are drawn. The results from previously analyzed radar

sensor concepts are used to subsequently define the system and estimate its capabilities. The system is then built up and its performance is evaluated so that the follow-up research can be undertaken.

The second area is dedicated to the equipment developed for the radar sensor calibration. The radar calibration equipment is usually very expensive and highly time-demanding in terms of programming in order to provide target performance. Given that, the short range CW radars are usually tested in real situations (measurement of e.g. a person in motion, car etc.). However, the testing in real situations is quite time demanding and is limited to a dedicated shooting range (considering ADS). In regard to the above-mentioned statements, the measurement method designed for radar sensor parameters without using complex testing equipment was devised.

The third area deals with a complex noise analysis, which is shown on a CW radar sensor, but is applicable in principle to any radar with coherent mixing. Aside the noise of linear RF components, the analysis counts with the amplitude and phase noise of local oscillator. Although demonstrated on a homodyne CW radar, the analysis works on a heterodyne system as well.

2 Continuous Wave Radar Sensors

2.1 Introduction

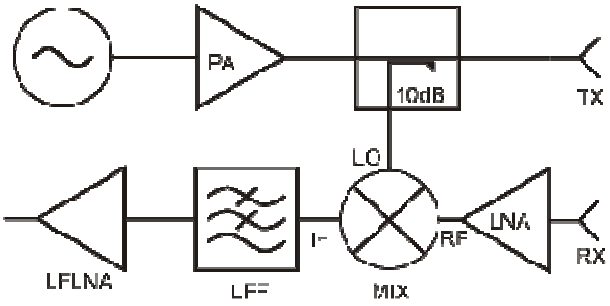

Fig. 2.1 Block diagram of basic analog CW radar sensor.

The block diagram of basic analog version of CW radar sensor is shown in Fig. 2.1. The structure is bi-static (i.e. employs separate TX and RX antennas; this is beneficial from the point of view of overloading receiver input and influence of local oscillator phase noise) and is based on direct coherent mixing of the input signal to the base-band. Thus the frequency of output signal is directly equivalent to the Doppler frequency shift. The signal transmitted by the CW radar sensor can be expressed as follows [13]:

$$s_{TX}(t) = A_{TX}\cos(\omega t + \Psi_{TX}) \tag{2.1}$$

In this equation, Ψ_{TX} represents the general signal phase shift and $\omega = 2\pi f$ stands for the angular frequency, where f is the transmitted frequency. Antennas of the CW radar sensor in question can be generally tilted with respect to the trajectory of the flying target; see Fig. 2.2 and 2.3. Hence the time-dependent distances R_{TX} and R_{RX} (i.e. distances between the target on one hand and the transmitting and receiving antennas on the other) can be indicated using formulae (2.2) and (2.3):

$$R_{TX} = R_{0TX} + v_m t \sin\alpha\cos\beta_{TX} \tag{2.2}$$

$$R_{RX} = R_{0RX} + v_m t \sin\alpha\cos\beta_{RX} \tag{2.3}$$

The R_{0TX} and R_{0RX} values denote initial distances of the target at the time $t = 0$. The β_{TX} and β_{RX} angles correspond to the Fig. 2.2 and 2.3, while v_m stands for the module of target velocity. The received signal can be described as:

$$s_{RX}(t) = A_{RX}\cos[\omega(t - \tau_{bi}) + \Psi_{RX}] \tag{2.4}$$

Using equations (2.2) and (2.3), the bi-static time delay τ_{bi} can be formulated as:

$$\tau_{bi} = \frac{R_{TX} + R_{RX}}{c} = \frac{R_{TX0} + R_{RX0} + v_m t \sin\alpha(\cos\beta_{TX} + \cos\beta_{RX})}{c} \tag{2.5}$$

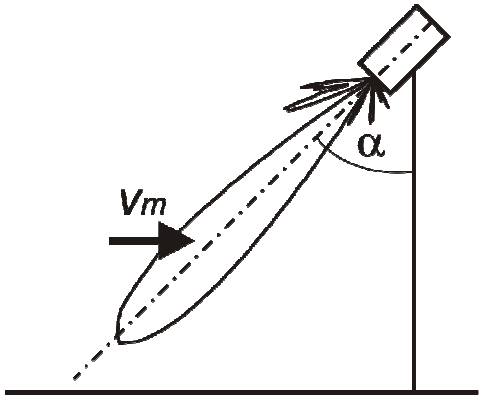

Fig. 2.2 Orientation of radar sensor with respect to flying target (vertical plane).

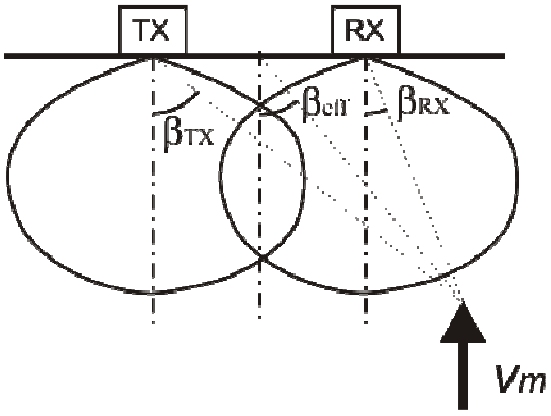

Fig. 2.3 Orientation of bi-static radar sensor with respect to flying target (horizontal plane).

In order to simplify further descriptions, the sensor can be approximated using (2.6) and (2.7) and hence can be considered as a pseudo-mono-static sensor, which detects the missile at the distance R_0 and at the effective angle β_{eff}:

$$2R_0 = R_{0TX} + R_{0RX} \tag{2.6}$$

$$\cos\beta_{eff} = \frac{\cos\beta_{TX} + \cos\beta_{RX}}{2} \tag{2.7}$$

Since the subjective sensors are supposed to operate at a very close target-to-sensor distances, the analysis of this approximation was performed and the existing approximation error is discussed in Chapter 2.1.1.

In the CW radar sensor, the signal $s_{RX}(t)$ received by the RX antenna is mixed with a copy of transmitted signal $s_{TX}(t)$. At the mixer output and additional low-pass filter, the base-band signal s_{bb} is available:

$$s_{bb}(t) = A_{bb}\cos(\omega\tau + \Psi_{bb}) \tag{2.8}$$

Using (2.5) - (2.7), the signal (2.8) can be expressed as:

$$s_{bb}(t) = A_{bb}\cos(\frac{2\omega R_0}{c} + \frac{2\omega v_m t \sin\alpha\cos\beta_{eff}}{c} + \Psi_{bb}) \tag{2.9}$$

Formula (2.9) designates the base-band signal with the Doppler frequency f_d defined by formula (2.10):

$$f_d = \frac{2fv_m \sin\alpha\cos\beta_{eff}}{c} \tag{2.10}$$

The equation (2.10) shows the relations among target's speed, its trajectory with respect to the sensor and frequency of the output baseband signal. Dependences of f_d on α and β_{eff} can be used for localization of the target.

2.1.1 Monostatic Approximation Error

Although the approximation described by (2.7) is not valid for the entire range of possible angles, it can be used in most cases. The exact Doppler frequency shift can be articulated in the following manner:

$$f_d = \frac{vf_t \sin\alpha(\cos\beta_{TX} + \cos\beta_{RX})}{c} \tag{2.11}$$

Using (2.7), the well-known formula for the sum of cosines leads to:

$$f_d = \frac{2vf_t \sin\alpha\cos\beta_{eff}\cos\left(\frac{\beta_{TX} - \beta_{RX}}{2}\right)}{c} \tag{2.12}$$

This indicates that the approximation is valid only under the condition (2.13).

$$\cos\left(\frac{\alpha_{TX} - \alpha_{RX}}{2}\right) \approx 1 \tag{2.13}$$

The relative error Δf can be therefore described as:

$$\Delta f = 1 - \cos\left(\frac{\alpha_{TX} - \alpha_{RX}}{2}\right) \tag{2.14}$$

For instance, the 1% error in frequency leads to the maximum angle difference $\alpha_{TX} - \alpha_{RX} < 8°$. Under the worst-case scenario, the minimum range for 1% error equals R = 1 m (assuming TX-RX antennas distance d = 0.32 m). See Fig. 2.4 for the complete error distribution.

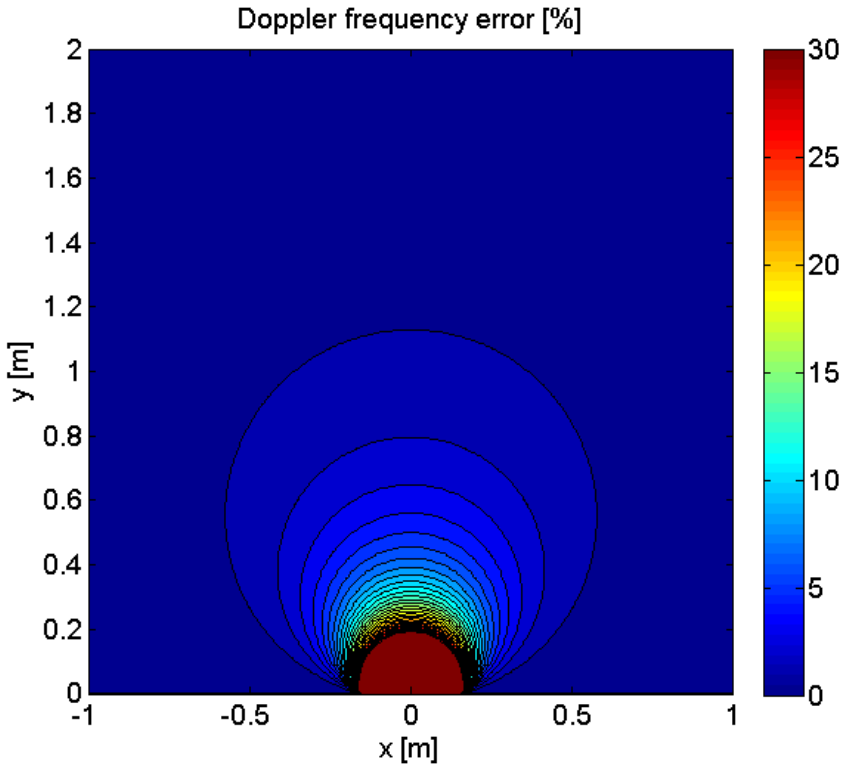

Fig. 2.4 **Mono-static approximation error in [%] for bi-static radar with antenna distance 0.32 m.**

Commonly, radar sensors operate in medium to far ranges. Given that, the above-described approximation error usually attains negligible levels. In the given application, where the concerned targets fly in a very close vicinity of radar sensors, it is common that the error described by (2.14) has to be taken into consideration.

2.2 Multi-sensor microwave curtain

The configuration of sensors, which is subject to the further research, can be seen in Fig. 2.5. The sensors are fixed alongside one of the walls of protected vehicle. For simplicity, let us assume that the missile is flying horizontally and perpendicularly towards the protected wall.

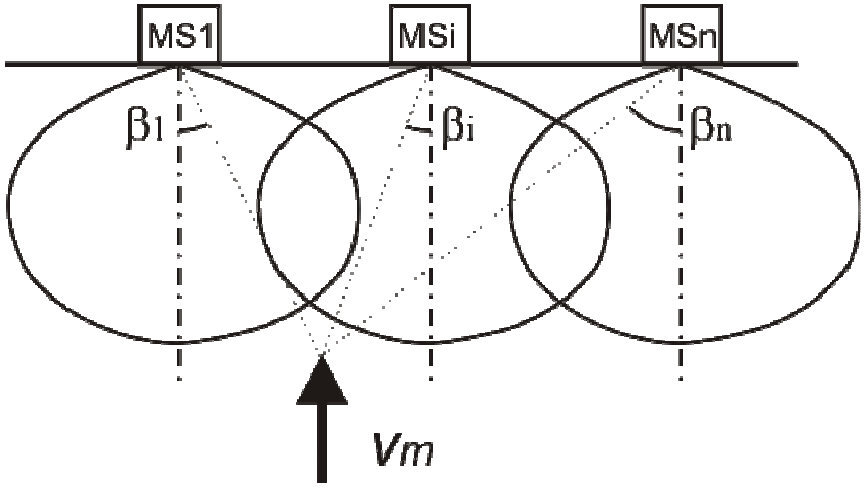

Fig. 2.5 Multi-sensor MC with approaching missile (top view).

The baseband signal at the output of the *i*-th sensor can be expressed in the following way:

$$s_{bbi} = A_{bbi}\cos(\omega\tau_i + \Psi_{bbi}) \tag{2.15}$$

$$\tau_i = \frac{2(R_{0i} + v_m t \sin\alpha\cos\beta_i)}{c} \tag{2.16}$$

In this formula, α stands for the vertical tilt of radar antennas (see Fig. 2.2) and β_i denoted the *i*-th azimuth of the target with respect to the MS.

Similarly to (2.9), the output signal Doppler frequency can be expressed as:

$$f_{di} = \frac{2vf}{c}\cos(\beta_i)\sin(\alpha) \tag{2.17}$$

In conformity with formula (2.17) and Fig. 2.5, the highest Doppler frequency is generated by the MS, which is in the closest proximity to the instantaneous position of flying target. This is also the main idea used for estimation of the searched horizontal position. Though the information on amplitudes of MS output signals are available, they are far too much dependent on unknown distances of the target and also on poorly predictable RCS (Radar Cross-Section) values. Given that, the developed method is focused on Doppler frequencies. The developed algorithm finds the sensor, which measures the highest Doppler frequency (i.e. the nearest sensor to the missile trajectory). Considering signals from the neighboring sensors, the algorithm strives to decide whether the missile flies right under the given MS or within the zone between two MSs.

Fig. 2.6 shows the situation when the missile is approaching the area somewhere between two neighboring MSs. The protected area is divided into zones with the width equal to d_z and the sensor distance $d=2d_z$. The sensor measuring the highest Doppler frequency is marked as MS_i, whereas the sensor with the second highest Doppler frequency as MS_j, where $j = i \pm 2$. Supposing

the instantaneous position of the missile to be at the boundary of the *i*-th zone, it is possible to define the boundary Doppler frequency ratio:

$$k_b = \frac{f_{di}}{f_{dj}} \tag{2.18}$$

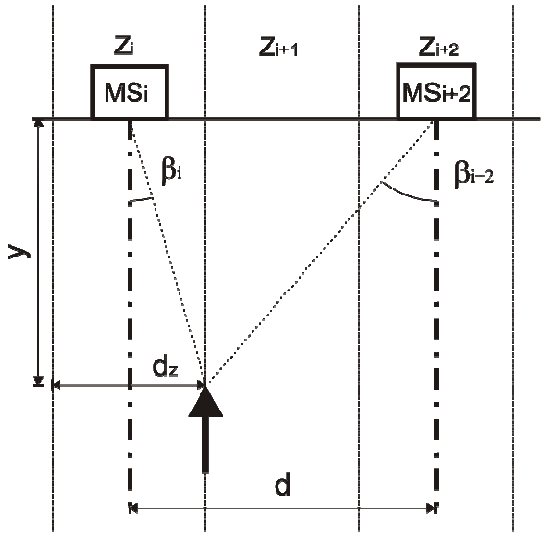

Fig. 2.6 Situation of two neighboring MSs (top view).

This boundary frequency ratio can be expressed using formula (2.17):

$$k_b = \frac{f_{Ti}\cos(\beta_i)}{f_{Tj}\cos(\beta_j)} = \frac{f_{Ti}\sqrt{y^2 + (d_z/2)^2}}{f_{Tj}\sqrt{y^2 + (d - d_z/2)^2}} \tag{2.19}$$

where *y* stands for the distance of point the detected missile intersects the radiation pattern from the MS. In fact, it is the function of vertical position of the missile with respect to the protected wall. Since the vertical position is unknown, the simple statistical method was used for finding the optimum k_m value:

$$k_m = E(k_b(y)) \tag{2.20}$$

In this calculation, *y* was treated as a random variable with uniform distribution in <0.59, 2.38> ranges. Limits of k_b for $y = 0.59$ *m* and $y = 2.38$ *m* are equal to 1.48 and 1.04, respectively. The aforementioned values lead to $k_m = 1.15$. The decision borders were established using formulae (2.19) and (2.20). The missile flies through the zone *i* provided that:

$$\frac{f_{di}}{f_{dj}} > k_m \tag{2.21}$$

Otherwise the detected missile flies through the zone $i \pm 1$.

Although the described method seems to be simple and reliable, in practice, it is faced with problems of determination of proper values of the subjective Doppler frequencies. During the flight of missile through the EM field of antennas, the angles α and β vary in time. As a result, the generated Doppler frequencies also vary in time. In addition, due to the illumination of longer and relatively thick flying missiles by the EM wave, a more complex distribution of surface currents can be expected. Moreover, each part of the current distribution shows slightly different angles and distances with respect to the TX and RX antennas. Consequently, a group of slightly different Doppler frequencies appears at outputs of sensors. This phenomenon gives rise to beats in the output signals, too. Therefore, relatively complex output signals can be expected; see Figs 2.8 and 2.12. The determination of proper Doppler frequency from the existing group of frequencies has not been satisfactorily managed yet. Some improvements could be achieved by using a narrow beam antenna. However, this implies a high directivity, which is connected to high antenna dimensions and/or a high radar frequency.

2.2.1 Experimental results

The tested MC set-up consisted of the set of three Doppler radar sensors (No.1, 3 and 5, from left to right; see Fig. 2.7) installed at the top of 2.5 m high and 3 m wide gate. The TX and RX antennas were fixed 400 mm apart; distances between the sensors being equal to 1 m. Three types of targets listed below were used for the tests:

- 9 mm gun projectiles simulating nearly dot targets,
- 500 mm long crossbow missile simulating thin linear targets,
- RPG-7 military missiles..

The targets were shot horizontally and perpendicularly to the plane of the gate. A set of impact points in area below the MC was chosen. The real coordinates were measured according to penetrations into a sheet of paper. All signals were recorded and subject to further processing.

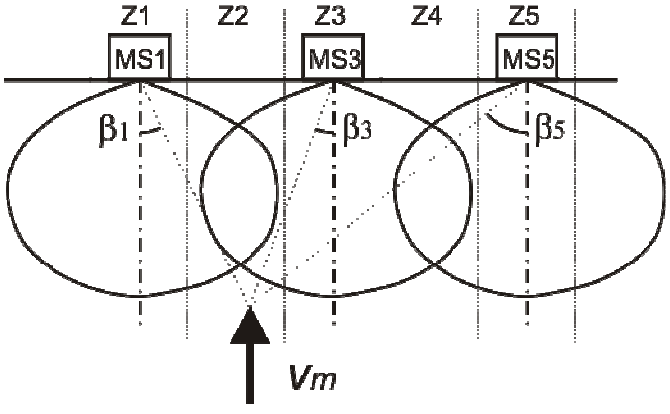

Fig. 2.7 Currently tested MC set-up (top view).

During the practical tests, signals corresponding to the number of shots were recorded, each record including data from channels 1, 2, 3 (MS 1, 3, 5). In order to show the previously described phenomena, some of them are presented in this work. The first set of figures (Figs. 2.8 – 2.11) contains data related to the flight of the 9 mm thick gun bullet between sensors 2 and 3, and 0.5 m below the gate top. Fig. 2.8 depicts the time dependences of all three channels.

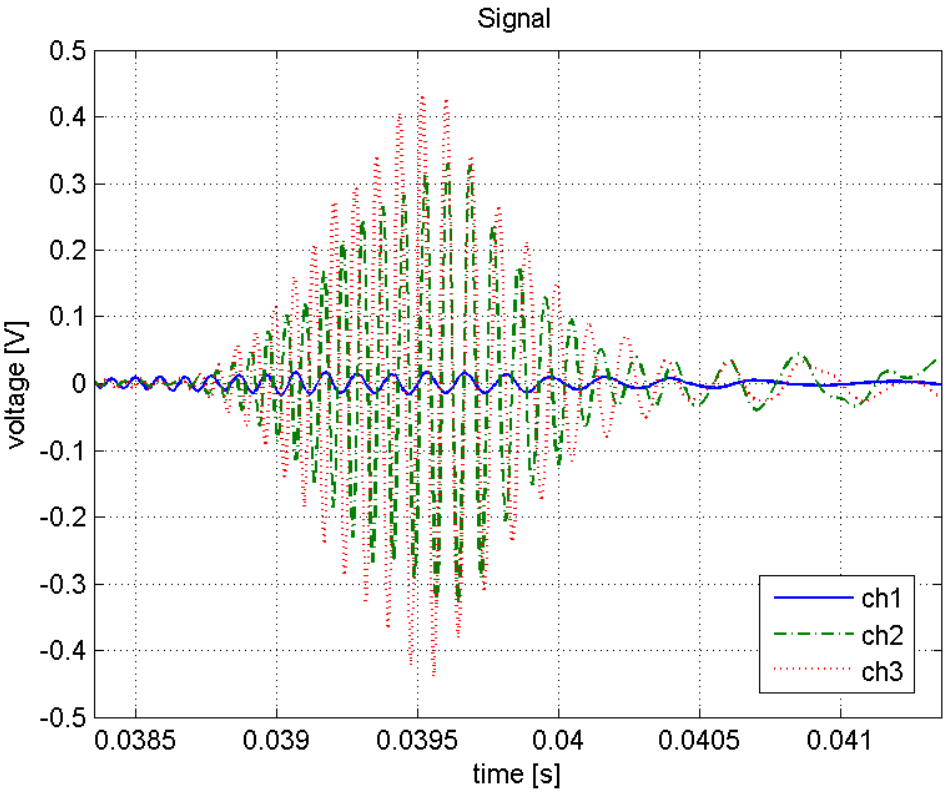

Fig. 2.8 9 mm bullet, time dependences of output voltages.

The corresponding calculated spectrograms can be found in Figs. 2.9 – 2.11. All of them demonstrate the expected drop in the Doppler frequencies in time. The horizontal position (center between the MS3 and MS5 = zone 4) can be determined comparing the spectrograms in Figs. 2.10 and 2.11, which indicate nearly identical frequencies and amplitudes. The bullet fulfils the idea of flying point reflector. Its spectrograms are understandable and the Doppler frequencies are easily readable.

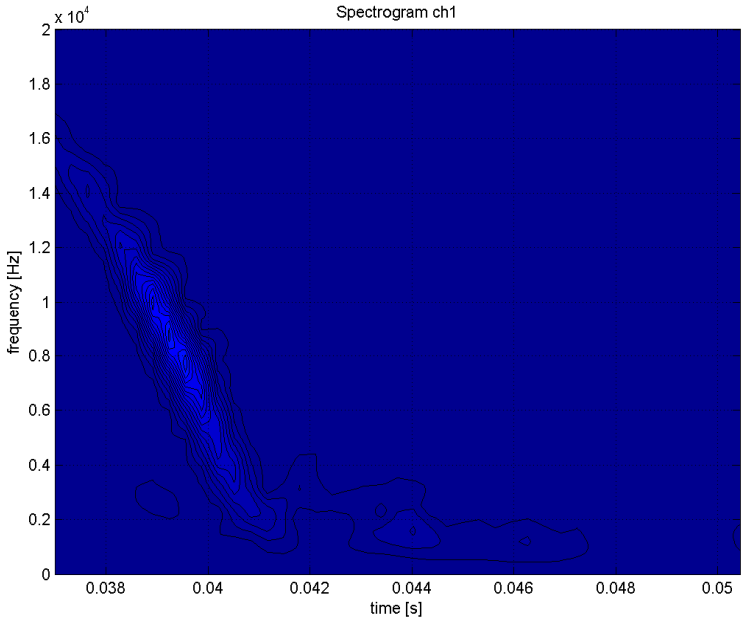

Fig. 2.9 9 mm bullet, calculated spectrogram, sensor 1 (ch1).

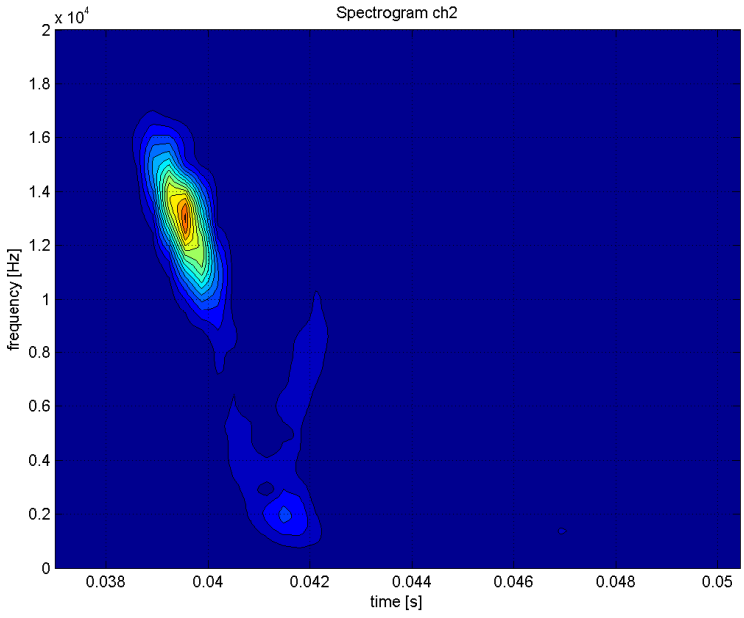

Fig. 2.10 9 mm bullet, calculated spectrogram, sensor 3 (ch2).

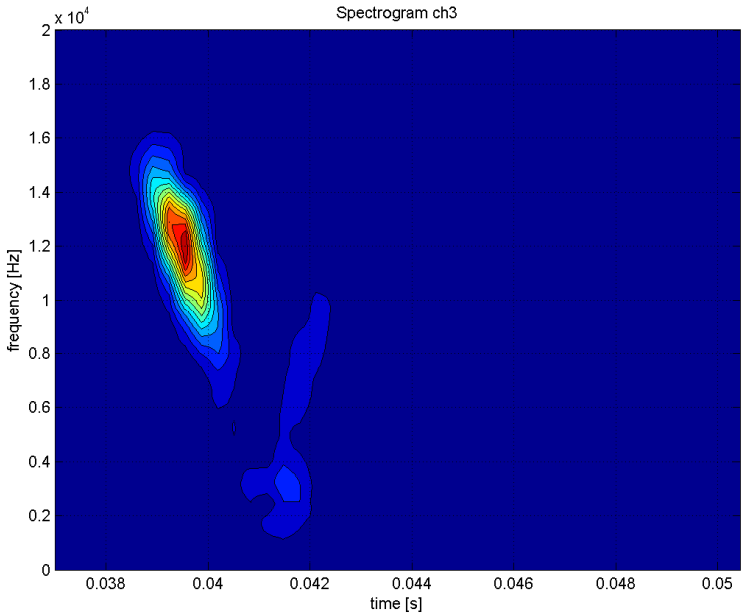

Fig. 2.11 9 mm bullet, calculated spectrogram, sensor 5 (ch3).

More complex signals were obtained from measurements of RPG-7 missiles. Fig. 2.12 illustrates the time dependences of recorded voltages, while Figs. 2.13 – 2.15 demonstrate the calculated spectrograms. In this case, the missile was shot directly under MS3 and, again, about 0.5 m below the gate top.

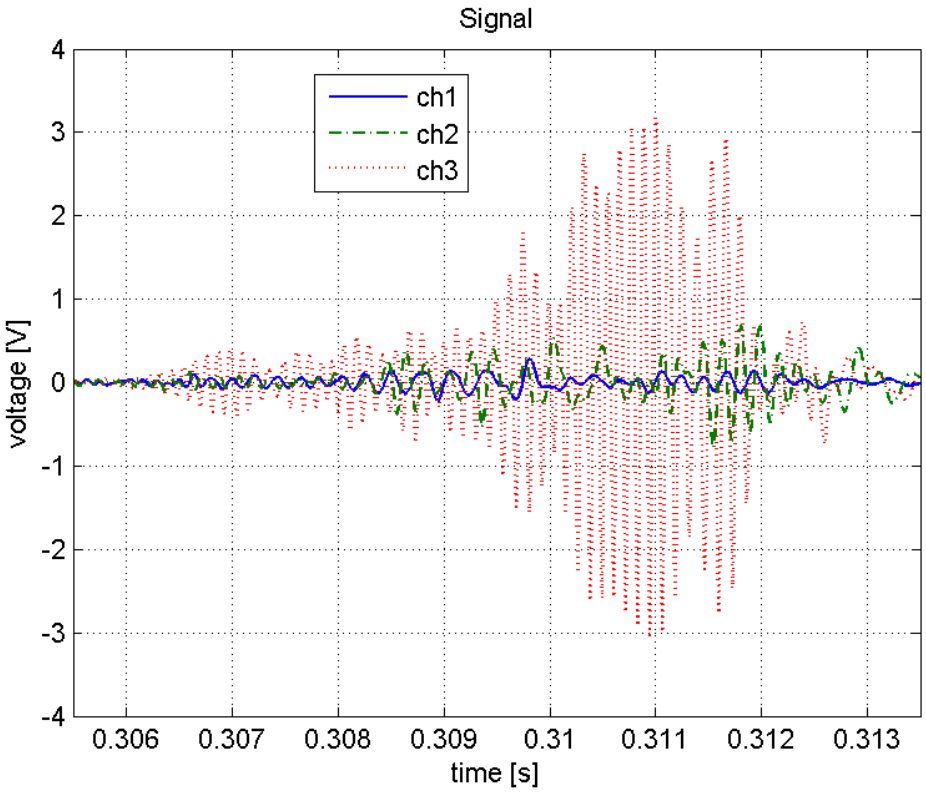

Fig. 2.12 RPG-7 missile, time dependences of output voltages.

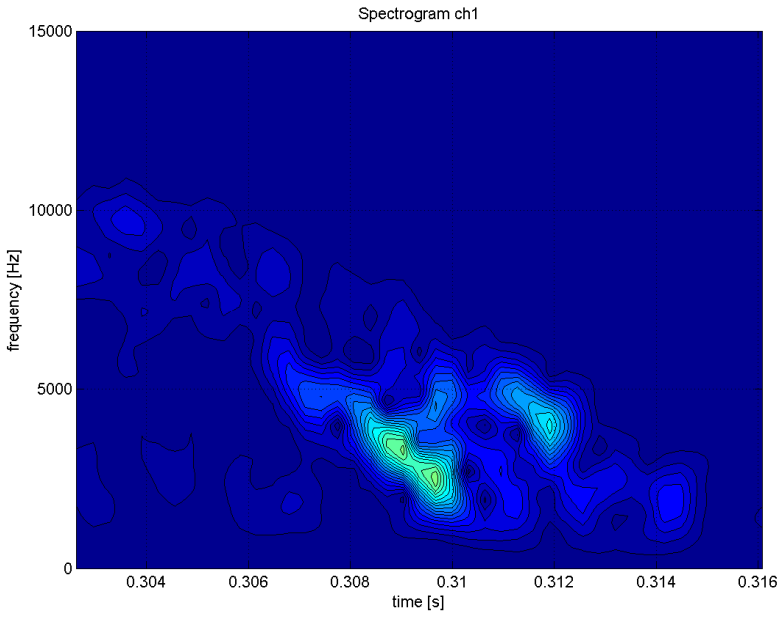

Fig. 2.13 RPG-6 missile, calculated spectrogram, sensor 1 (ch1).

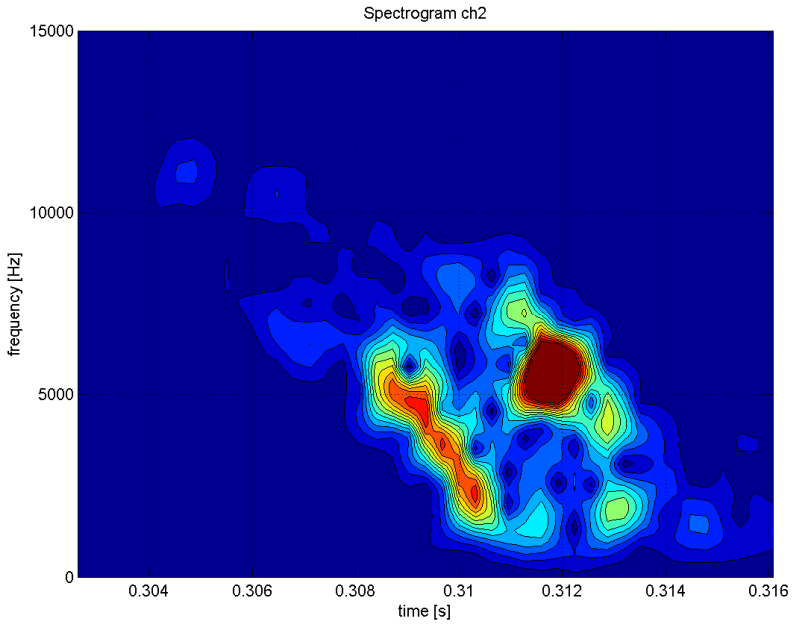

Fig. 2.14 RPG-7 missile, calculated spectrogram, sensor 3 (ch2).

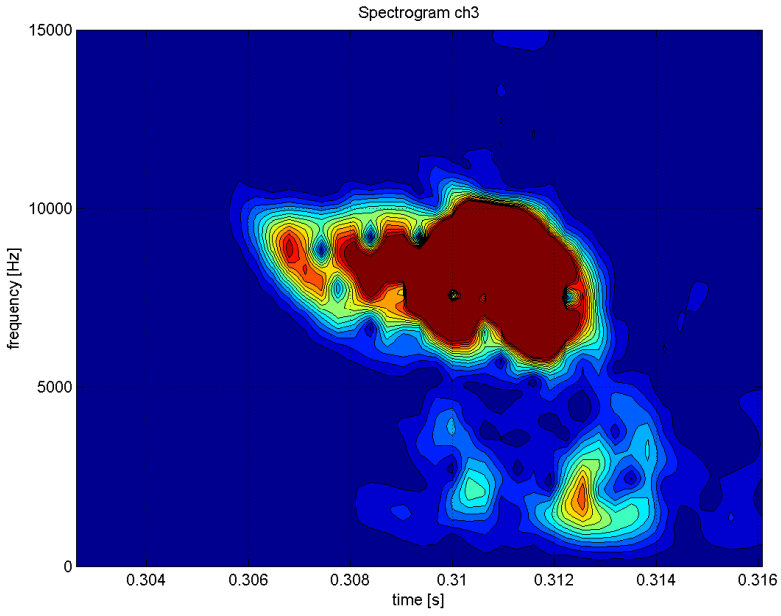

Fig. 2.15 RPG-7 missile, calculated spectrogram, sensor 5 (ch3).

The presented figures show that both time dependences and spectrograms of RPG-7 missile considerably differ from those of the 9 mm gun bullet. The main reasons for this are presented in Chapter 2.3. The horizontal position of target with respect to the MC was determined according

to formulae (2.17) to (2.21). For proper function of the subjective ADS, it is necessary to determine the zone (or two nearby zones), in which the target hits the protected wall; see Fig. 2.7. The results are indicated in Tab. 2.1. The table shows that in the case of determination of two most probable zones, the success rate is about 85.7%. This is close to the required localization reliability.

Measurement No.	Determined zone	Exact zone
1	3, 4	3
2	2, 3	3
3	1,2	3
4	2, 3	3
5	4, 5	4
6	4, 5	5
7	4, 5	5
8	4, 5	5
9	4, 5	5
10	4, 5	5
11	4, 5	5
12	4, 5	4
13	1, 2	3
14	2, 3	3

Tab. 2.1 Measured and calculated results.

2.2.2 Conclusion

Despite the acceptable results, the method suffers from errors in determination of proper Doppler frequencies. This is primarily due to the above described spreading of Doppler frequencies, generated by complex and large targets in the close vicinity of the sensors (see Figs. 2.13 – 2.15). Follow-up development is going to be focused on this problem and the determination of proper frequency from the group of available results that would be reflected in calculations. Other difficulties stem from the limited accuracy of determining Doppler frequencies by means of the FFT in the case that only a short time period is available for the determination. Due to that, other determination methods of horizontal position of the target were also considered and elaborated; see Chapters 2.4 – 2.5.

2.3 Dual-level Microwave Curtain

As the time dependences and spectrograms presented in Figs. 2.13 – 2.15 are specific to different types of missiles, they can be considered as time/frequency 'imprints' and used for distinguishing different types of targets. In case of ADSs, they are employed in order to distinguish the thread missiles from relatively harmless ones (especially all types of bullets). However, if the MC is supposed to activate the suitable counter-measure, it is impossible to let the target fly through the entire antenna radiation pattern and generate the complete ‘imprint’. Therefore, if the

identification of targets is required, the concept of dual-level microwave curtain was designed and tested; see Fig. 2.16.

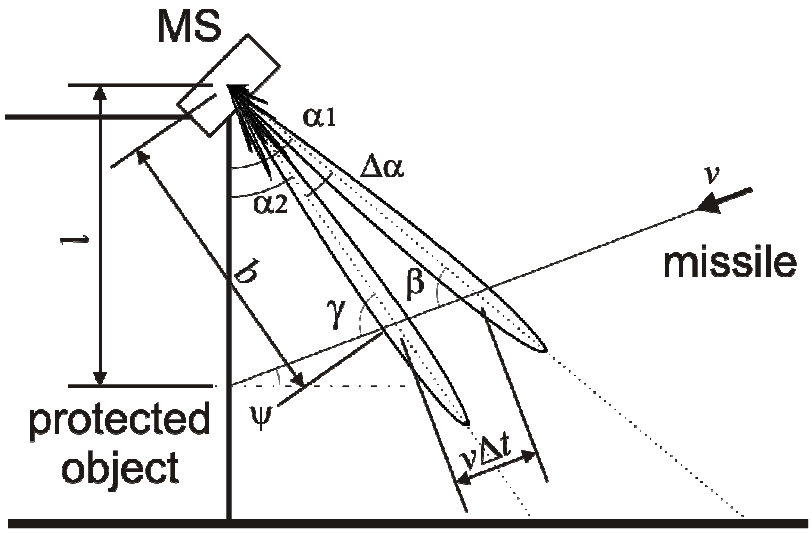

Fig. 2.16 Dual level microwave curtain (side view).

The dual level MC consists of two independent microwave sensors with two antenna pairs, while each antenna pair is tilted under a different angle (α_1 and α_2). Owing to this arrangement, prior to detection by the second antenna pair, the missile can fly through the entire radiation pattern of the first antenna pair. The obtained records show that although the missile flew through the first sensor under the different angle, the spectrograms differ only slightly; see Figs. 2.17 – 2.19.

Various types of missiles provide different spectrograms, which can be considered as specific time-frequency 'imprints' and compared with imprints stored in the memory of processing computer. This procedure is similar to the comparison of fingerprints. In principle, the system is able to decide whether the approaching target is a thread missile or a relatively harmless object.

Other virtue of the developed structure consists in its ability to determine several important parameters of the detected target. This concerns the target speed v, elevation of its trajectory ψ, and vertical component of impact point. Considering formula (2.10) and Fig. 2.16, the measured Doppler frequencies can be expressed by means of the following equations:

$$f_{d1} = \frac{2v}{c} f_{T1} \cos\beta \cos\Phi_1 \tag{2.22}$$

$$f_{d2} = \frac{2v}{c} f_{T2} \cos\gamma \cos\Phi_2 \tag{2.23}$$

where f_{di} stands for the Doppler frequency shifts of the *i-th* sensor, v represents the missile speed, c symbolizes the speed of light, f_{Ti} describes the *i-th* transmitted frequency and β and γ stand for angles defined in Fig. 2.16. Beside that the angle Φ_i represents the target azimuth with respect to

the antenna direction. The azimuths Φ_1 and Φ_2 can be approximated with one variable Φ for small values of Φ_i or small $\Delta\alpha$.

By substituting $\gamma = \Delta\alpha + \beta$, the formula (2.23) can be re-arranged into (2.24):

$$\begin{aligned} f_{d2} &= \frac{2v_m}{c} f_{T2} \cos(\Delta\alpha + \beta)\cos\Phi = \\ &= \frac{2v_m}{c} f_{T2} (\cos\Delta\alpha\cos\beta - \sin\Delta\alpha\sin\beta)\cos\Phi = \\ &= \frac{2v_m}{c} f_{T2} \left(\cos\Delta\alpha\cos\beta - \sin\Delta\alpha\sqrt{1-\cos^2\beta}\right)\cos\Phi \end{aligned} \tag{2.24}$$

Substituting $\cos\beta = x$ and $K_i = \frac{f_{di}}{2\cos\Phi \cdot f_{Ti}} c$, a nonlinear system of equation can be formed (2.25).

$$\begin{aligned} K_1 &= vx \\ K_2 &= v\left(x\cos\Delta\alpha - \sin\Delta\alpha\sqrt{1-x^2}\right) \end{aligned} \tag{2.25}$$

The analytical result of (2.25) for cosβ and v could be expressed by the below-listed formulae:

$$\cos\beta = x = \frac{\frac{f_{d1}}{f_{T1}}\sin\Delta\alpha}{\sqrt{\left(\frac{f_{d1}}{f_{T1}}\right)^2 + \left(\frac{f_{d2}}{f_{T2}}\right)^2 - 2\frac{f_{d1}f_{d2}}{f_{T1}f_{T2}}\cos\Delta\alpha}} \tag{2.26}$$

$$v = \frac{cf_{d1}}{2\cos\beta\cos\Phi f_{T1}} \tag{2.27}$$

Using the basic geometry rules, the following equations corresponding to Fig. 2.16 can be written:

$$\frac{\sin\Delta\alpha}{v\Delta t\cos\Phi} = \frac{\sin\beta}{b} \tag{2.28}$$

$$\frac{\sin(\pi - \alpha_1 - \beta)}{b} = \frac{\sin\gamma}{l}, \tag{2.29}$$

where l stands for the vertical distance from antennas, b describes the distance in the plane of sensor 2 radiation pattern, v incorporates the speed of target and Δt is the time the target flies from the first to the second sensor detection plane. Equations (2.28) and (2.29) can be used for determination of vertical impact point of the target:

$$l = b\frac{\sin\gamma}{\sin(\pi - \beta - \alpha_1)} = v\Delta t\cos\Phi\frac{\sin\beta}{\sin\Delta\alpha}\frac{\sin(\Delta\alpha + \beta)}{\sin(\beta + \alpha_1)} \tag{2.30}$$

The said formulae are valid for azimuth $\Phi = 0$; good results can be achieved for a small azimuth (up to few tens of degrees) as well.

2.3.1 Measured Results

The test set-up was arranged according to Fig. 2.16; angle between the main antenna lobe and vertical line is defined by angles $\alpha_1 = 60°$ and $\alpha_2 = 35°$, the operating frequencies were set to f_{T1} = 10.4 GHz and f_{T2} = 11 GHz.

Fig. 2.17 shows the spectrograms equivalent to the detected flight of the 9 mm bullet within the 10 – 50 ms time-section. The left spectrogram illustrates the approx. 4 ms-long flight-through with the Doppler frequency around f_{d1} = 19 kHz, corresponding to the center of the main-lobe of MS1. The right spectrogram demonstrates the corresponding Doppler frequency f_{d2} that ranges from 5 to 15 kHz (measured by MS2). The interval length where the target is seen by the sensor is related to the antenna beam width. The error in time/frequency localization caused by antenna highly exceeds the error caused by Gabor's time-frequency uncertainty theorem, which is described further.

Fig. 2.18 depicts the spectrograms equivalent of the flight of 50 cm long arrow within the 10 – 150 ms time-section. From approximately t = 85 ms, the spectrogram of MS1 signal shows ca. 35 ms-long flight-through. At t = 120 ms, the signal from MS2 contains strong components which can generate triggering impulses. The Doppler frequency shift reaches f_{d1} = 5.2 kHz (measured by MS1), f_{d2} is in the range of 1 – 4 kHz (measured by the MS2).

Fig. 2.19 includes the spectrograms corresponding to the flight of RPG-7 missile within the 150 – 340 ms time-frame. The spectrogram of the signal from MS1 shows a 10 ms-long flight-through, while the Doppler frequencies reach values of f_{d1} = 9.7 kHz. The signal measurer by MS2 contains frequencies f_{dM} in the range of 2 – 7 kHz.

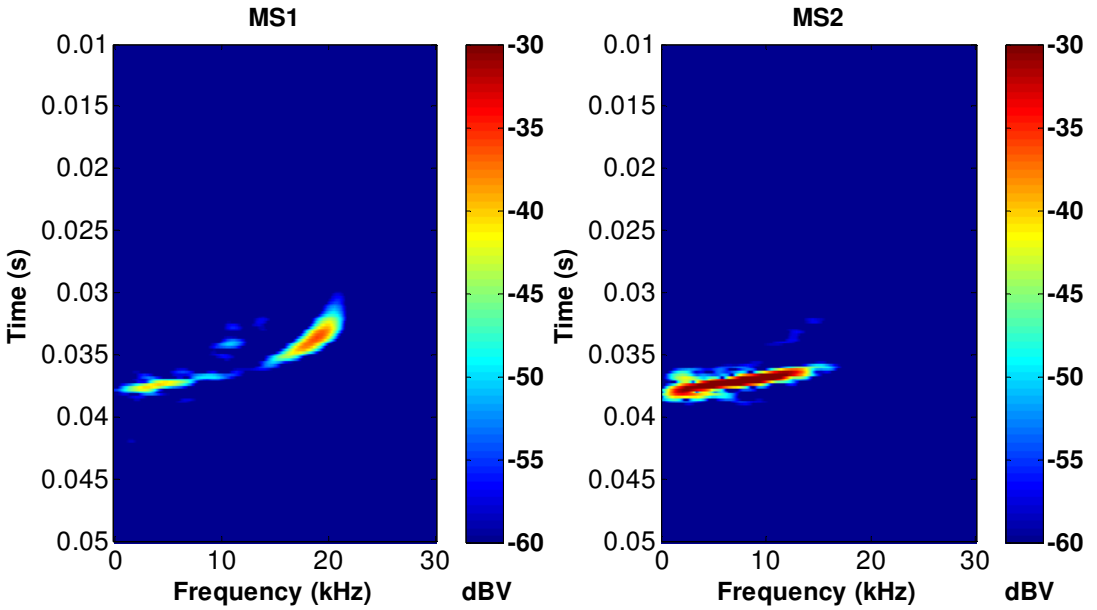

Fig. 2.17 **Spectrogram of 9 mm bullet; microwave sensors 1 – advanced (MS1 – left), microwave sensor 2 – main (MS2 – right).**

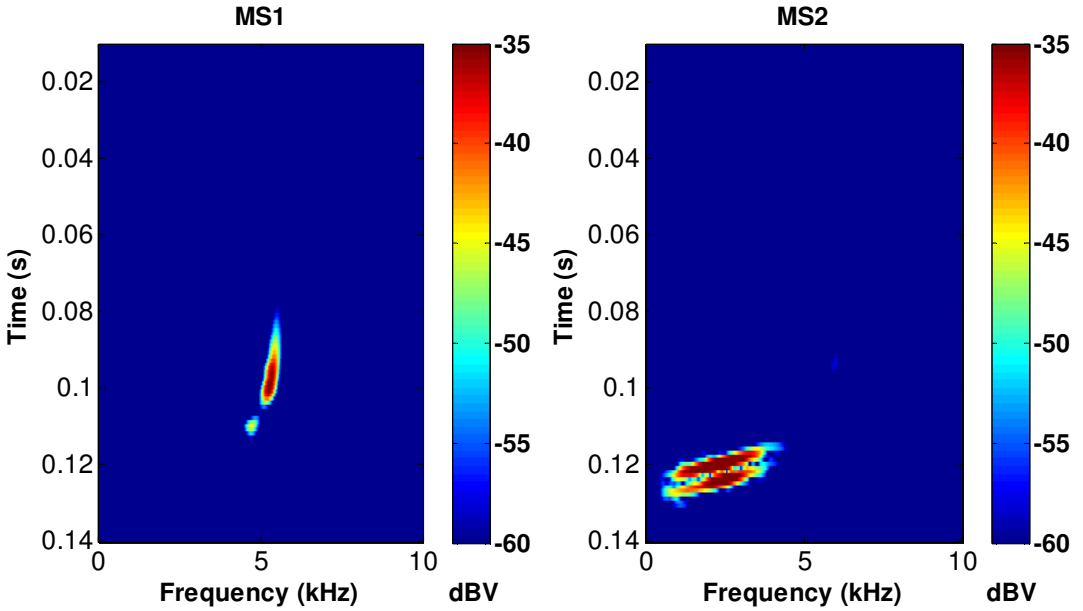

Fig. 2.18 **Spectrogram of crossbow arrow; microwave sensors 1 – advanced (MS1 – left), microwave sensor 2 – main (MS2 – right).**

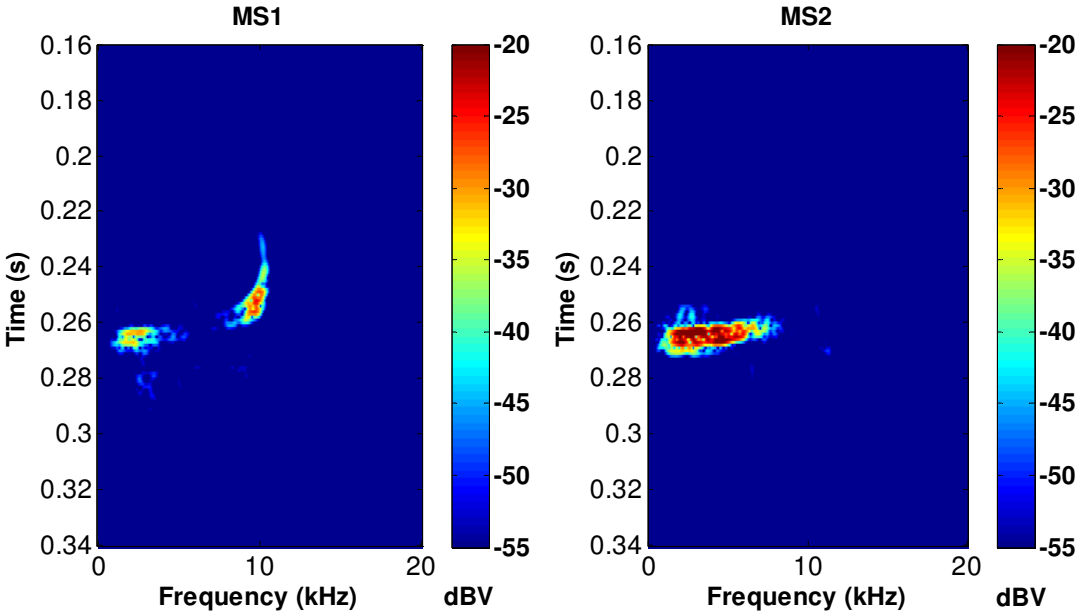

Fig. 2.19 **Spectrogram of RPG-7 missile; microwave sensors 1 – advanced (MS1 – left), microwave sensor 2 – main (MS2 – right).**

Data from Figs. 2.17 – 2.19 were arranged into Table 2.2 and both target velocity and trajectory elevation were calculated (the mean value of Doppler shifts being used). In comparison to the velocity of RPG-7 missile and the arrow to measurement in Chapter 2.4.4 (velocity of about 155 m/s and 85 m/s for missile and arrow, respectively), it was revealed that the measurements suffer from significant errors, which are discussed later in Chapter 2.3.2.

Target	f_{d1} (kHz)	f_{d2} (kHz)	v_t (m/s)	ψ (deg)
bullet	19	10	381	14
arrow	5.2	3	98.6	10
RPG-7	9.7	5	197	15

Tab. 2.2 **Parameters of test set-up.**

Due to the erroneous estimation of target velocity and inability to accurately estimate Δt, the vertical position of impact point was not calculated.

2.3.2 Accuracy of Presented Method

The presented method was analyzed to provide accuracy of the calculated results; target velocity v_m and its trajectory elevation ψ were of prime interest. Since the calculation is based on the solution of non-linear equations, the accuracy strongly depends on parameters of the test set-up and target trajectory.

Following figures shows the extent to which the accuracy depends on FFT resolution and frequency measurement error. Two cases were considered: the first one provides the frequency

resolution Δf = 1 kHz, while the other one provides the resolution Δf = 100 Hz. The frequency resolution is selected in order to balance the sufficient signal time-variance (i.e. the time during which the target flies through the antenna radiation pattern is limited) and the maximum frequency resolution (which is limited by Gabor's time-frequency uncertainty theorem [14] $\Delta T \Delta f \geq \frac{1}{2}$).The parameters remained the same as in the measurement set-up, aside from velocity and elevation that vary: v_t = 90 – 190 m/s, ψ = -10° – 60°.

The trajectory elevation error and velocity error for frequency measurement accuracy of 1 kHz and 100 Hz are depicted in Figs. 2.20 – 2.21 and 2.22 – 2.23, respectively.

The findings are the following: while 100 Hz frequency resolution provides calculation errors of few percent of velocity and maximum of 6 degrees in trajectory elevation, the resolution of 1 kHz is insufficient for this method.

Even though the frequency estimation is affected by FFT accuracy, the main frequency measurement error for MS2 is caused by the high antenna tilt related to the target trajectory (angle γ) and insufficiently wide antenna beam. The wide range of Doppler frequency shift (that can be seen in Figs. 2.17 - 2.19 – right) is caused by a different actual angle between the target trajectory and antenna during the flight-through. See [15] for detailed description of this phenomenon for complex targets.

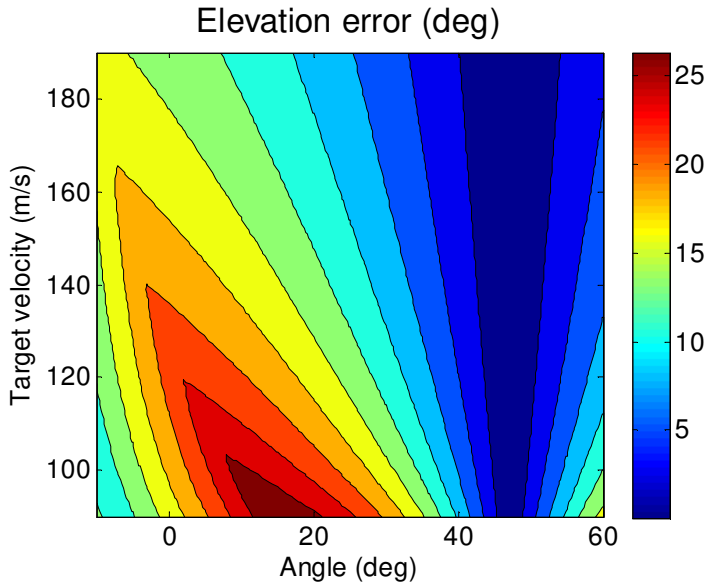

Fig. 2.20 Angle measurement error of 0 to 25 degrees for 1 kHz frequency accuracy.

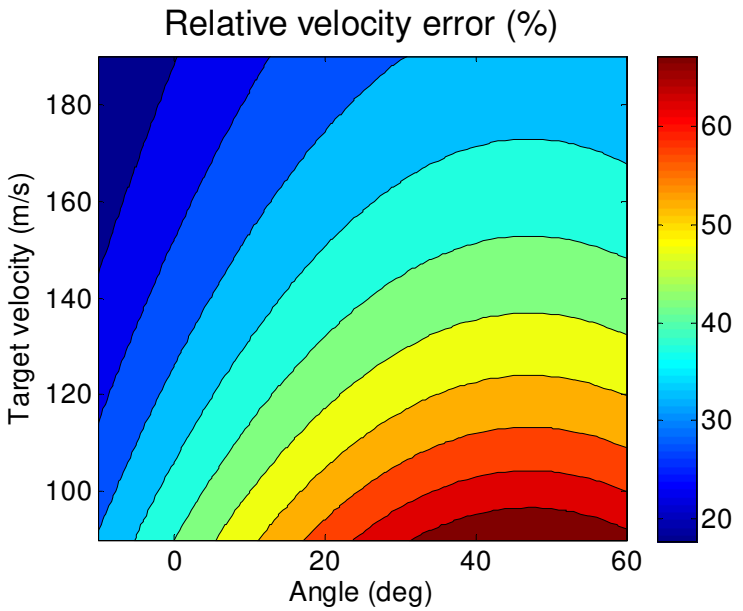

Fig. 2.21 **Approximately 30% to 40% velocity measurement error due to 1 kHz frequency measurement accuracy.**

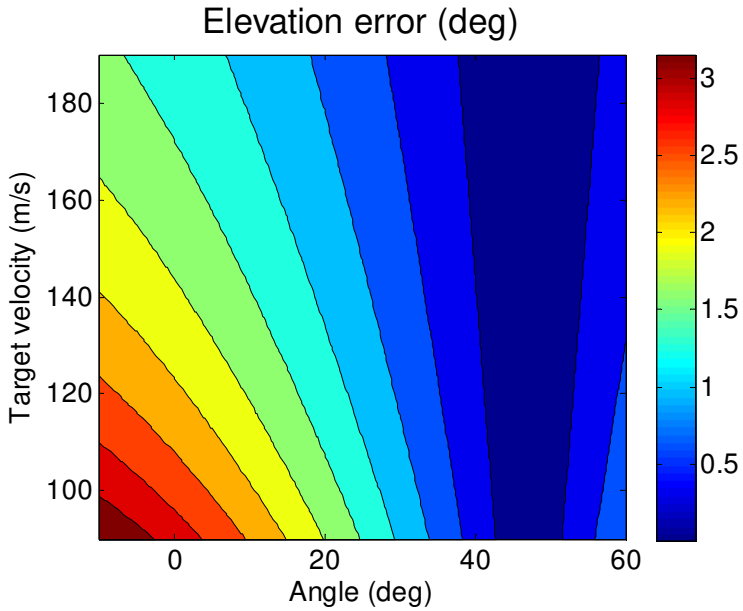

Fig. 2.22 **Maximum elevation measurement error of 3 degrees due to 100 Hz frequency measurement accuracy.**

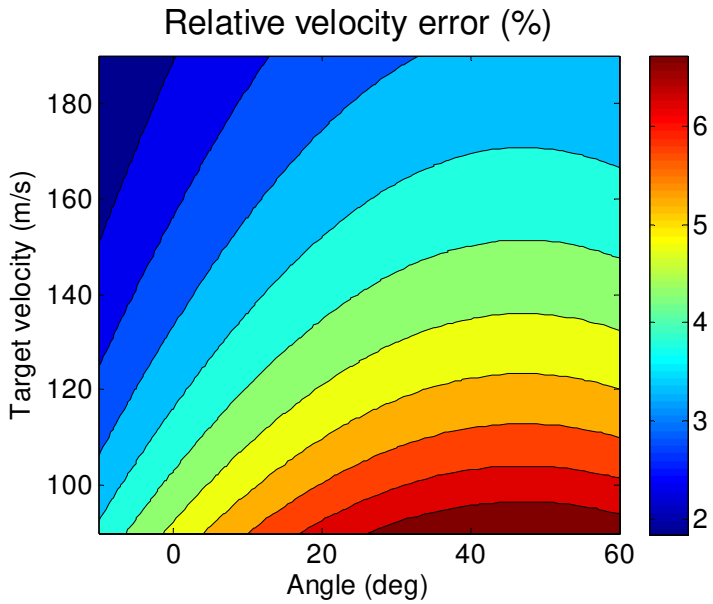

Fig. 2.23 **Relative velocity measurement error better than 6% for all range in case of 100 Hz frequency measurement accuracy.**

The accuracy of vertical impact point can be estimated from (2.30), since it depends on the velocity and measured time Δt only (the other variables depend on the dedicated set-up and the measurement error can be neglected).

The relative and absolute measurement errors of vertical impact point can be expressed by (2.31) and (2.32), respectively.

$$\frac{\Delta l}{l} = \sqrt{\left(\frac{\Delta v}{v}\right)^2 + \left(\frac{\Delta(\Delta t)}{\Delta t}\right)^2}\,, \tag{2.31}$$

$$\Delta l = \sqrt{(\Delta(\Delta t)v)^2 + (\Delta v \Delta t)^2} \cdot \cos\Phi \frac{\sin\beta}{\sin\Delta\alpha} \frac{\sin(\Delta\alpha+\beta)}{\sin(\beta+\alpha_1)} \tag{2.32}$$

In these equations, Δv stands for the velocity error and $\Delta(\Delta t)$ symbolizes the time difference error.

For better insight into the accuracy impact on the results, let us see Table 2.3 providing the calculated vertical position of impact point l and related error. Calculations were made using parameters specified above, except the target velocity $v = 150$ m/s and trajectory elevation $\psi = 0$ deg.

Variable	Values		Description
v (m/s)	150		target velocity
Δv (m/s)	15		velocity measurement error
ψ (deg)	0		target trajectory elevation
Δt (ms)	10	10	time of flight between sensor's patterns
$\Delta\Delta t$ (ms)	1	10	time measurement error
l (m)	1.45	1.45	vertical position of impact point
Δl (m)	0.21	1.5	Impact point measurement error
$rel\ \Delta l$ (%)	0.14	100	relative impact point measurement error

Tab. 2.3 Example of calculation of vertical position of impact point affecting measurement errors.

It can be concluded that the accuracy of vertical position of impact point depends mainly on the accuracy of time difference Δt measurement. The total error of 0.21 m can be achieved with measurement accuracy of 1 ms; however, 10 ms accuracy leads to the unacceptable error equal to 1.5 m. Beside others, the time measurement accuracy strongly depends on the radar sensor radiation pattern, hence the antenna with narrow radiation pattern is crucial. This also increases the accuracy of Doppler frequency shift for antennas with high tilts (MS2).

2.3.3 Conclusion

Although the method presented in Chapter 2.3 has significant drawbacks, it points out the possible application of microwave radar sensors. Assuming the higher transmitted frequency, the proportionally higher Doppler frequency shift gives rise to the better relative frequency resolution while maintaining the FFT step ΔT.

Considering radar sensors used in automotive industry (77 GHz), the velocity accuracy is better than 10% and 1% for 1 kHz and 100 Hz frequency resolutions, respectively. The elevation accuracy is better than 4 degrees and 0.4 degrees, respectively. While utilizing the higher frequency, the narrow beam antennas can be fabricated while maintaining the compact design. All aforementioned facts raise the accuracy of vertical position of impact point.

2.4 Adaptable Microwave Radar Sensor with Pseudo-random Noise Sequence Modulation

2.4.1 Radar Structure

The functionality of sensor mentioned in Chapter 2.3 can be further extended using a steerable antenna and pseudo-random noise sequence (PNS) modulation. Since steerable antenna arrays with phase shifters are very complex and costly, the attention was paid to frequency steerable antennas, specifically the leaky wave antenna (LWA) designed on the substrate integrated

waveguide (SIW) [16]. This antenna provides sufficiently low beam-width and main lobe span of about 90 degrees.

The advantages of employing LWA include space savings (in comparison to the situation when two different antennas are used), continuous angle steerability and possibility to combine different functionalities of one sensor without any additional hardware being utilized. In the case of widely spread software defined radio (SDR) approach, the sensor can perform more functions simultaneously.

PNS can provide additional functionality of the radar sensor, such as the distance measurement (in surveillance radar (SR) mode), coexistence of several radar sensors etc. All of them are important in electronic warfare (interference immunity, lower radiated power spectrum density, etc). On the other hand, the wide band PNS modulation can affect the antenna beam-width. This phenomenon is discussed further in Chapter 2.4.2.

The block diagram of bi-static radar sensor enabling operation at two different frequencies is depicted in Fig. 2.24. The sensor is composed of two identical transmitting and receiving branches, while digital modulators MOD1 and MOD2, as well as correlators COR1 and COR2, are fed by signals from the PNS generator. The CW carrier of branch 1 transmitter is generated by the local oscillator operated at the frequency f_1 and modulated in digital modulator MOD1. Signals from both branches (at frequencies f_1 and f_2) are added, amplified by power amplifier PA and connected to the input of LWA-T transmitting antenna. The signals reflected from the target are received by LWA-R receiving antenna and amplified by the low noise amplifier LNA. By means of an identical CC combining circuit, they are subsequently divided into two receiving branches. The receiving branch 1 is equipped with the correlator COR1, down-converter DC1, output base-band filter/amplifier cascade FA1, and analog-to-digital converter ADC. At its output, the signal corresponding to the operation of frequency f_1 is available while the FA2 output provides the signal corresponding to the operation of frequency f_2. That is why the single LWA-based microwave radar is able to act as two independent sensors monitoring two directions at the same time.

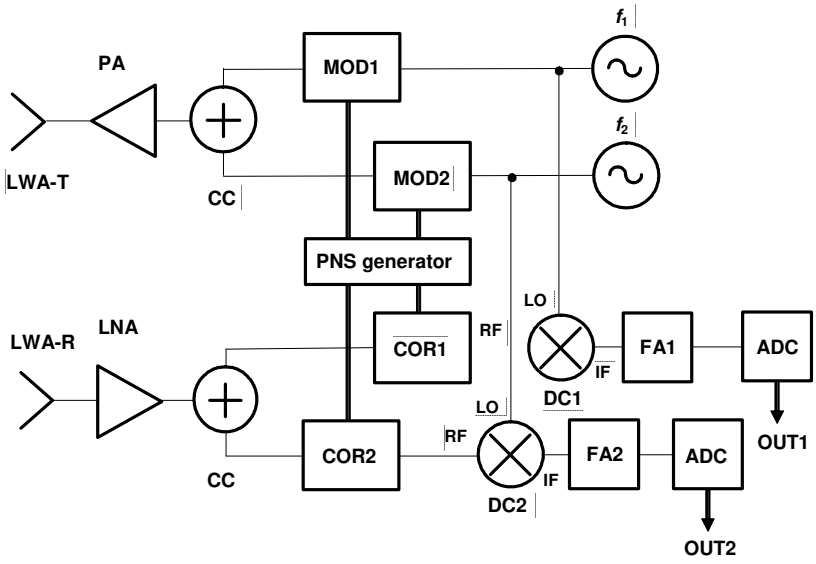

Fig. 2.24 Block diagram of multi-mode PNS CW radar sensor.

Fig. 2.24 reveals another limiting phenomenon that has to be taken into account. The distance between f_1 and f_2 depends upon the used modulation bandwidth and receiver immunity from interference. Since the latter depends on many parameters (e.g. the type of digital modulation used and PNS length - the longer the sequence, the higher the immunity), the minimum distance between f_1 and f_2 has to be determined from analyses of particular radar structure and signal-processing procedures employed.

2.4.2 Wideband Modulation

As it was already stated, the directional characteristic of frequency steerable antenna is greatly determined by the frequency. From this point of view, each frequency component of modulated signal is radiated in a slightly different direction, which is significant especially in the case of wideband signals. Due to this, the possible impact on the delay measurement of radar signal has been investigated.

It results from Oliner's theoretical analysis [17] stipulating that the directional characteristic of a long LWA can be expressed in the following manner:

$$D(\theta) = \frac{\cos^2 \theta}{\left(\frac{\alpha}{k_0}\right)^2 + \left(\frac{\beta}{k_0} - \sin\theta\right)^2} \tag{2.33}$$

where α symbolizes the attenuation constant, β represents the phase constant (both of them being the functions of frequency) and k_0 is the free-space wave number. If we suppose

$$\frac{\alpha}{k_0} << 1, \tag{2.34}$$

the radiated beam is relatively narrow. It reaches its maximum at the angle:

$$\theta_0 \approx \arcsin\left(\frac{\beta}{k_0}\right), \tag{2.35}$$

and its shape around the maximum can be approximated

$$D(\theta_0 + \Delta\theta) \approx \left(\frac{k_0}{\alpha}\cos\theta_0\right)^2 \left(1 - \left(\Delta\theta \frac{k_0}{\alpha}\right)^2\right). \tag{2.36}$$

Given that, if we use the linearization of frequency dependence of k_0/α around the carrier frequency f_0, we get a simple quadratic approximation of the LWA directional characteristic that was used during the analysis

$$D(\theta, f) = 1 - \left(\frac{\theta - \theta_0 - a(f - f_0)}{b}\right)^2 \tag{2.37}$$

where θ_0 represents the angle of maximum radiation at frequency f_0, a stands for the constant describing the linearized dependence of radiation angle on the frequency, and b is the half width of the main lobe.

The transmitted signal is expressed in the form

$$s_T(t) = g(t)\cos 2\pi f_0 t \tag{2.38}$$

where $g(t)$ embodies the real modulation signal with the spectrum

$$G(f) = G^*(-f) \tag{2.39}$$

concentrated into $\pm f_m$ frequency band. This form of signal covers all common radar signals, including pulse signals or the aforementioned pseudo-noise signals.

The analysis was performed on the signal $s_R(t)$ reflected from a target situated in direction θ_T and received using the same LWA type as the transmitter. In order to make the analysis independent of the carrier frequency, we analyzed the baseband complex envelope $\tilde{s}_R(t)$ of the received signal. We did not consider the Doppler shift as it is much lower than the signal bandwidth, thus, its influence is negligible.

The complex envelope spectrum of received signal can be expressed

$$\tilde{S}_R(f) = K\,\tilde{H}(\Delta\theta_T, f) G(f) e^{-j2\pi f \tau_R} \tag{2.40}$$

where K represents the signal attenuation, τ_R stands for the received signal delay and

$$\tilde{H}(\Delta\theta_T, f) = \left[1 - \left(\frac{\Delta\theta_T - af}{b}\right)^2\right]^2 \tag{2.41}$$

where

$$\Delta\theta_T = \theta_T - \theta_0 \tag{2.42}$$

corresponds to the frequency characteristic describing the influence of frequency dependence of the LWA radiation. This frequency characteristic can be articulated in polynomial form

$$\tilde{H}(\Delta\theta_T, f) = 1 - \sum_{i=0}^{4} c_i f^i \tag{2.43}$$

where

$$c_0 = \frac{2\Delta\theta_T^2}{b^2}\left(1 - \frac{\Delta\theta_T^2}{2b^2}\right), \tag{2.44}$$

$$c_1 = -\frac{4\Delta\theta_T a}{b^2}\left(1 - \frac{\Delta\theta_T^2}{b^2}\right), \tag{2.45}$$

$$c_2 = \frac{2a^2}{b^2}\left(1 - \frac{3\Delta\theta_T^2}{b^2}\right), \tag{2.46}$$

$$c_3 = \frac{4\Delta\theta_T a^3}{b^4}, \tag{2.47}$$

$$c_4 = -\frac{a^4}{b^4}. \tag{2.48}$$

The classic delay estimator is based on the complex envelope cross-correlation between received signal and modulation signal

$$R(\tau) = \int_{-\infty}^{\infty} g^*(t)\tilde{s}_R(t+\tau)dt \tag{2.49}$$

and takes the form

$$\hat{\tau}_R = \arg\max\left|R(\tau)\right|^2. \tag{2.50}$$

Using the spectra, the cross-correlation can also be expressed as

$$\begin{aligned} R(\tau) &= K\int_{-\infty}^{\infty} G^*(f)\tilde{S}_R(f)e^{j2\pi f\tau}df = \\ &= K\int_{-\infty}^{\infty}\left|G(f)\right|^2\tilde{H}(f)e^{j2\pi f(\tau-\tau_R)}df \end{aligned}. \tag{2.51}$$

After the frequency characteristic $\tilde{H}(f)$ described by (2.43) is inserted into (2.51) and the reverse Fourier transform is performed, the cross-correlation takes the form of a Taylor series

$$R(\Delta\tau) = K\left[R_g(\Delta\tau) - \sum_{i=0}^{4} \frac{c_i}{(j2\pi)^i} \frac{d^i R_g(\Delta\tau)}{d\Delta\tau^i} \right] \tag{2.52}$$

where $\Delta\tau = \tau - \tau_R$ and $R_g(\tau)$ is the autocorrelation function of modulation signal. Thus the resulting square of cross-correlation can be expressed.

$$|R(\Delta\tau)|^2 = K^2 \left[\begin{array}{l} \left(\begin{array}{l} R_g(\Delta\tau)(1-c_0) + \frac{c_2}{4\pi^2} \frac{d^2 R_g(\Delta\tau)}{d\tau^2} - \\ - \frac{c_4}{16\pi^4} \frac{d^4 R_g^4(\Delta\tau)}{d\tau^4} \end{array} \right)^2 + \\ + \left(\frac{c_1}{2\pi} \frac{dR_g(\Delta\tau)}{d\tau} - \frac{c_3}{8\pi^3} \frac{d^3 R_g(\Delta\tau)}{d\tau^3} \right)^2 \end{array} \right] \tag{2.53}$$

The autocorrelation $R_g(\tau)$ represents an even function implying that its odd derivatives are odd functions. Therefore, nonzero terms c_1 and c_3 cause the shift in the cross-correlation maximum, which results in the bias of resulting signal delay estimation. The respective bias depends on the angle deviation of target from the direction of maximum radiation θ_T. If the target is situated exactly at the radiation maximum, the bias equals zero. The component c_1 reaches its maximal values at

$$\Delta\theta_T = \pm\frac{b}{\sqrt{3}} \tag{2.54}$$

and the resulting error is totally negligible, provided

$$\frac{8af_m}{3\sqrt{3}b} << 1. \tag{2.55}$$

The influence of component c_3 grows as θ_T rises. It is fully negligible, as long as

$$\frac{4a^3 f_m{}^3}{b^3} << 1 \tag{2.56}$$

which is a lesser requirement than (2.55).

However, as the even derivatives are even functions, the nonzero terms c_2 and c_4 do not cause any bias of delay estimation. These terms describe the symmetric suppression of higher frequency components of the signal. The said suppression leads to a lower signal bandwidth and, consequently, to lower precision of the measured delay within the given signal-to-noise ratio. The effect caused by component c_2 is fully negligible if

$$\frac{2a^2 f_m^2}{b^2} << 1, \tag{2.57}$$

and the influence of component c_4 is negligible on condition that

$$\frac{a^4 f_m^4}{b^4} << 1 \tag{2.58}$$

Similarly, it is a lesser requirement than (2.57).

The term c_0 represents the attenuation caused by antenna directivity. It has no influence on the form of the received signal spectrum, yet, according to expectations, the attenuation rises with the angle deviation from maximum radiation direction $\Delta\theta_T$.

To give practical example, the modulation limits of LWA used in practical tests and described in thisch chapter were evaluated within the 10.2 – 11.4 GHz frequency band. Based on the measured radiation patterns presented in Fig. 2.25, the dependence of radiation angle on frequency was estimated to be around $a = 7 \cdot 10^{-10}$ rad/Hz, while the half width of the main lobe was assessed as $b = 0.2$ rad. Inserting these values into condition (2.55) results in the frequency limit of $f_m << 186$ MHz. Inserting the same parameters into condition (2.57) leads to the frequency limit of $f_m << 202$ MHz. This is why the maximum value of PNS chip frequency used during the practical tests was limited to $f_{chip} = 25$ MHz.

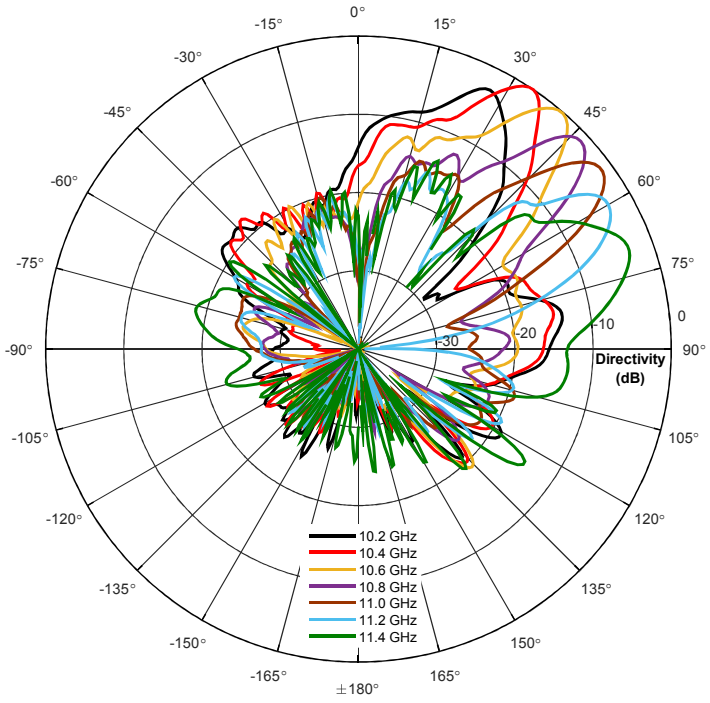

Fig. 2.25 LWA radiation pattern – E plane (vertical).

2.4.3 Operational Modes

The radar sensor equipped with two or more receivers or, alternatively, with an SDR base radar sensor can fulfill more functions simultaneously. Such system can provide different operation modes. The most important ones include:

- Adaptable surveillance radar mode – the sensor can compensate the tilt θ, so it is able to keep the horizontal aim by changing the operational frequency (see Fig. 2.26). The other sensor can scan higher elevations for incoming threats (Fig. 2.27).
- Dual-level microwave curtain mode – provides the same functionality as described in Chapter 2.3, but can add the tilt compensation as described above in adaptable SR mode.

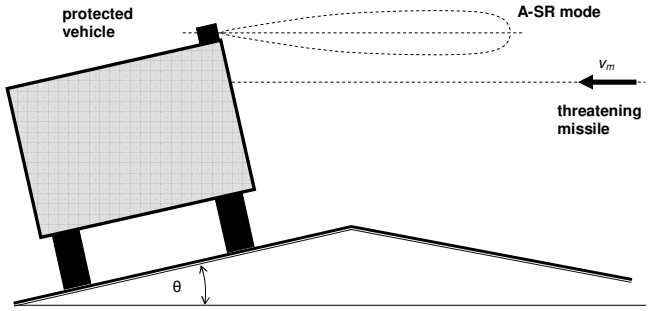

Fig. 2.26 Compensation of a vehicle's tilt in A-SR mode.

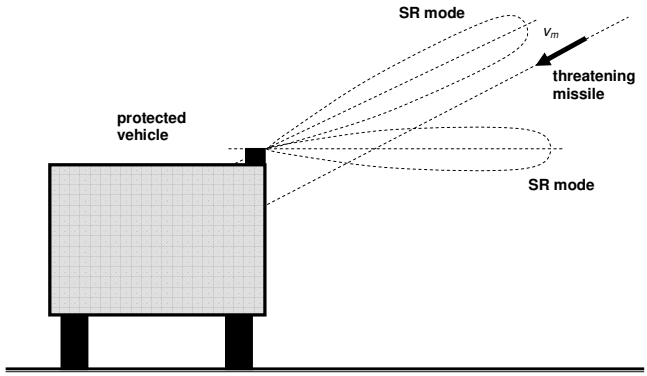

Fig. 2.27 Radar sensor in SR-SR mode.

2.4.4 Practical Tests

The radar sensor was tested in the following modes: surveillance radar with microwave curtain mode and dual level microwave curtain mode (the latter provided the same results as in Chapter 2.3). The developed PNS radar sensor was operated at two independent frequencies within the 9.3 to 11.4 GHz band and the modulation frequency f_{chip} = 25 MHz.

The tests were conducted using various targets: 9 mm bullets to simulate small targets, a cross-bow arrow to simulate longer 2D targets, and RPG-7 missiles to represent real and complex targets. Fig. 2.28 (a) shows the PNS radar sensor utilized during the testing, while Fig. 2.28 (b) depicts the measurement set-up at the military shooting range with an approaching RPG-7 missile flying through the center of measurement gate. The LWAs were fixed onto the top horizontal girder of measurement gate.

The spectrograms related to the flight of RPG-7 missile shot from the on-axis distance of 40 m are shown in Fig. 2.29. The missile was shot at $t = 0$, detected by the surveillance radar at approximately $t = 10$ ms. Its initial velocity equaled 113 m/s. At $t = 170$ ms, the rocket engine was automatically ignited and the missile started to accelerate until it flew under the measurement gate at $t = 305$ ms. The maximum velocity of 155 m/s could be estimated from the maximum Doppler frequency of surveillance radar (fd = 10.6 kHz). The flight-through is visible in the spectrogram from the second sensor (MC) at the time of approx. 298ms.

The spectrograms corresponding to the flight of cross-bow arrow, shot from the point situated on-axis and ca. 8 m in front of the measurement gate, are depicted in Fig. 2.30. The arrow was shot at $t = 0$ and the flight time record was 140 ms long. The surveillance radar spectrogram shows that the arrow initial velocity attained approx. 85 m/s. After 120 ms, the arrow passed under the measurement gate. At $t = 100$ ms, the arrow tip passed through the microwave curtain.

As it was stated above, the range measurement capability represents the main advantage of PNS applications.. Although the chip frequency was low (25 MHz), the range resolution can be better than 6 m (based on actual SNR). Combining range and velocity measurement in Kalman filter, the sufficient accuracy can be achieved, see Fig. 2.31.

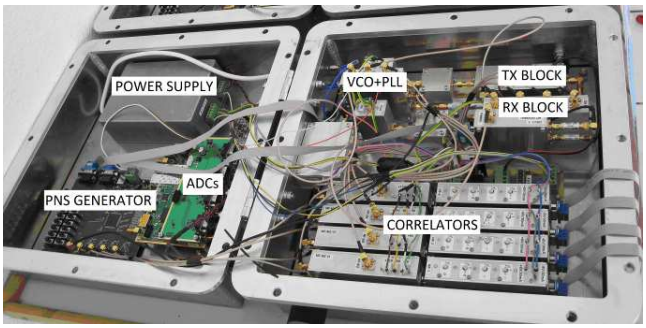

(a)

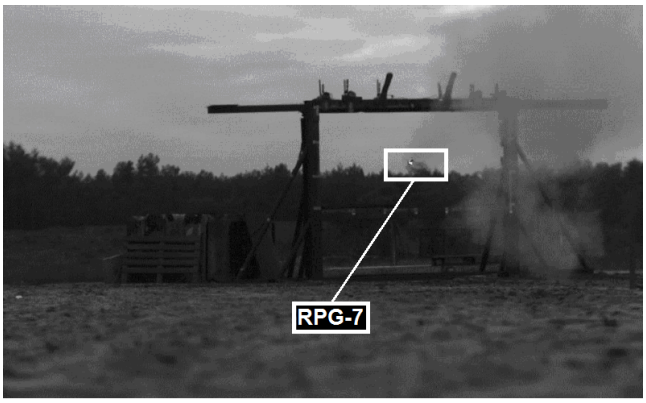

(b)

Fig. 2.28 **Equipment used during practical tests: (a) PNS radar sensor, (b) measurement gate with RPG-7 missile flying through its center.**

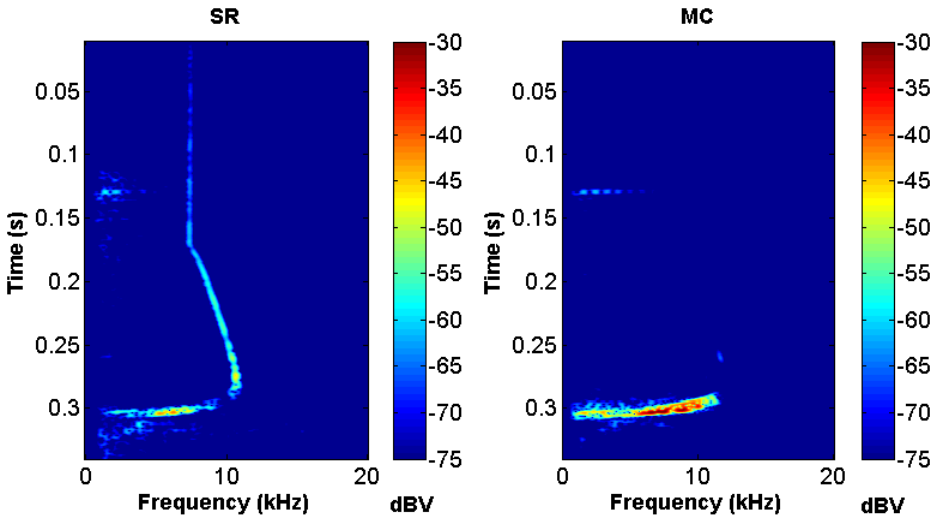

Fig. 2.29 **pectrograms related to flight of RPG-7 missile detected by surveillance radar branch (left) and microwave curtain branch (right), T_w = 5 ms.**

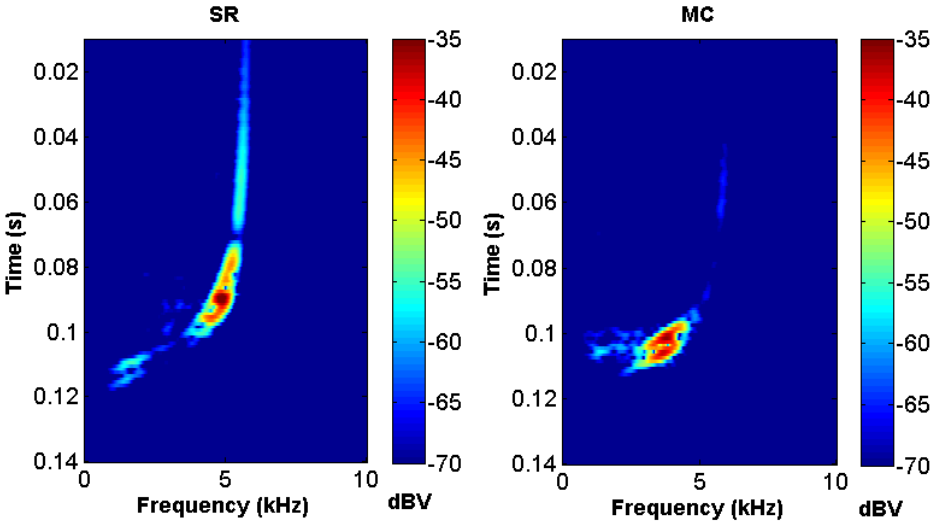

Fig. 2.30 **Spectrograms related to flight of cross-bow arrow detected by surveillance radar branch (left) and microwave curtain branch (right), T_w = 5 ms.**

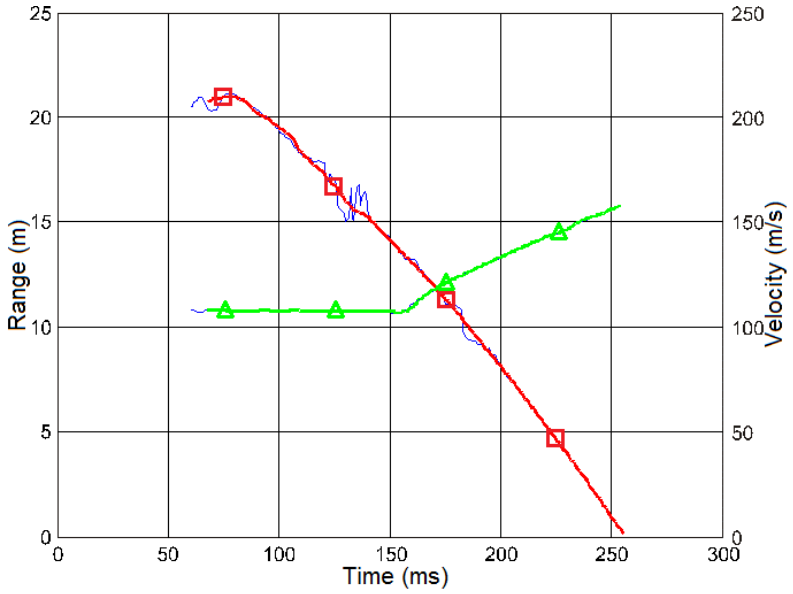

Fig. 2.31 **Range (blue = measured values, red squares = Kalman filter estimations) and radial velocity (green triangles) measurements of RPG-7 missile, f_{chip} = 25 MHz.**

2.4.5 Conclusion

The presented solution utilizes the well-known scanning capability of LWAs to integrate more functions in single radar sensor. Moreover, one antenna can be shared among two (or more) radar sensors that can perform more functions (detection, identification, tracking) simultaneously. Furthermore, all these functions can be automatically switched according to instantaneous AD system requirements.

The number of microwave hardware needed can be further reduced using SDR approach that provides more flexibility and efficiency.

The developed PNS radar sensor utilizes the wideband signal modulation, hence the work also includes the evaluation of LWAs‘ influences on the said modulations. The majority of technical solutions and sensor modes developed were verified at the military shooting-range using real missiles. The obtained results confirmed that the presented solutions function accurately.

2.5 Interferometric Radar

The principal function of developed ADS is to detect the approaching thread missiles and destroy or deactivate them by activating suitable counter-measures. The detection system consists of a set of sensors (commonly of very different types and purposes). The detection of thread missile in a medium zone (typically 20-30 m from the protected wall) constitutes of the main tasks of developed surveillance radar (SR). The SR contributes to identification of the target and ADS preparation for defense action. Furthermore, since the MC ability to determine the horizontal position of approaching missile has not been absolutely satisfactory, the SR development is also intensely oriented toward measurement of target trajectory (in horizontal plane) and impact point (IP) determination.

Since the SR has to track the target to the close vicinity of protected wall, it should also show no blind-zone. Therefore, employment of a form of CW radar structure can be recommended. As the analog type of the said radar is unable to measure radar-to-target distances, it cannot perform measurements of target trajectory in its simplest form. Nevertheless, the MISO (Multiple Input – Single Output) version of CW radar enabling measurement of DOA (Direction of Arrival) was developed within this work [18]. The determination of target trajectory can be consequently converted into the measurement of DOAs (azimuths) by employing two sensors that are placed relatively far apart.

2.5.1 Radar Structure

The structure of designed MISO CW radar sensor can be seen in Fig. 2.32. For the first tests, the version based on the above-described analog bi-static CW radar structure with direct conversion to base-band and relatively low output power was designed and manufactured. The radar operates at the frequency of 11 GHz; the transmitted signal is generated by the local oscillator (LO) and amplified by the power amplifier (PA). As transmitting antenna, the COMPA type (detailed in [19]) was employed. Its gain accounts for approx. 10 dB, while showing the 30-degree beam width in the vertical plane and 90-degree in the horizontal plane (-3 dB). The transmitting antenna illuminates the monitored area with CW signal. The receiver consists of four channels equipped with a simple 5 dB patch antenna; distances between neighboring patches equaling Δ = 16.8 mm.

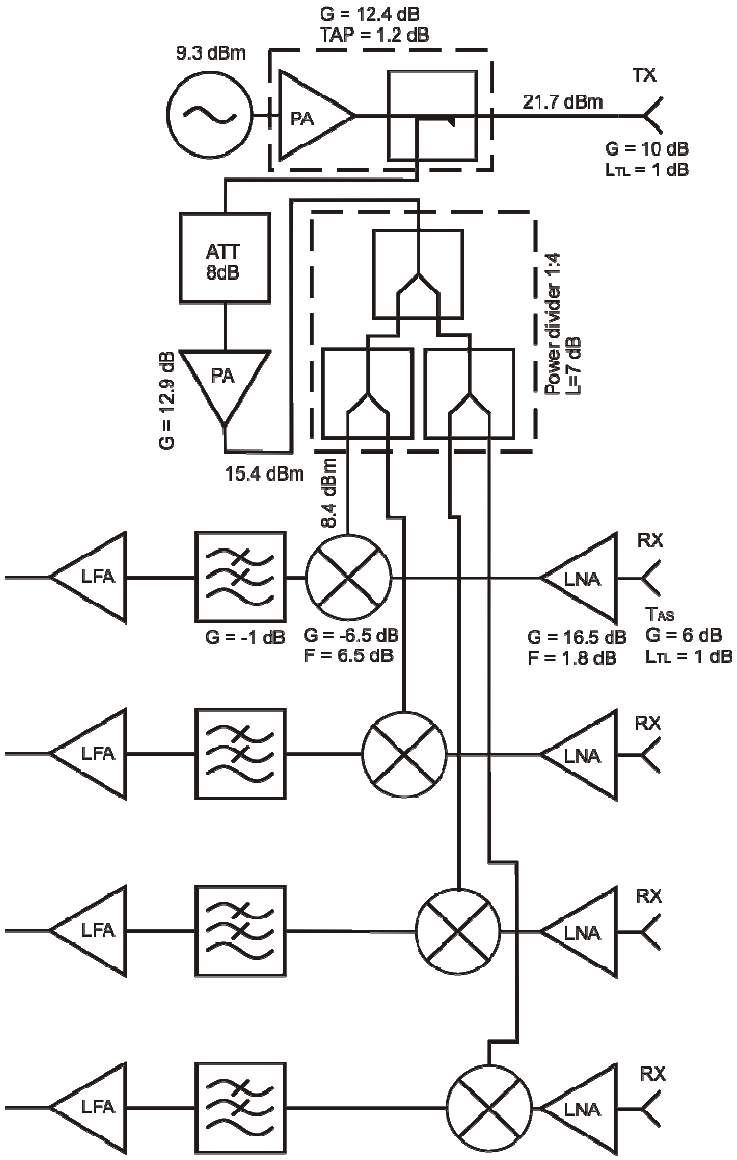

Fig. 2.32 Blok diagram of developed MISO CW radar sensor.

The received signal, reflected from the target, is amplified by the LNA and multiplied with reference signals derived from the transmitted signal. The base-band signal (after additional amplification and filtering) at the output of the *i-th* sensor can be expressed as:

$$s_{bi}(t) = A_{bi}\cos(2\pi f_{di}t + \Psi_i) \qquad (2.59/4.1)$$

$$f_{di} = \frac{2f(\mathbf{v_m}\cdot\mathbf{r_0})}{c} \qquad (2.60/4.2)$$

In formula (4.1), A_{bi} describes the amplitude of base-band signal, f_{di} stands for the Doppler frequency shift and ψ_i represents the general phase. The Doppler frequency f_{di} can be calculated using formula (4.2), where f symbolizes the transmitted RF frequency, $\mathbf{v_m}$ denotes the speed vector of target and $\mathbf{r_0}$ describes the unity radius vector between the missile and radar.

The amplitude of $s_{bi}(t)$ signal is proportional to the radar-target distance and *RCS* of the target as well, while its frequency is equal to the Doppler frequency shift. All output signals are subject to extensive signal processing.

2.5.2 Signal Processing Method

The signal processing method applied in this sensor is based on the ESPRIT super-resolution algorithm; see [20]. This algorithm is widely used for DOA estimation in wireless communications. In order to calculate the signal DOA, the ESPRIT method uses the phase differences between the received signals at antenna outputs. Moreover, it compares the modulation of incoming signals in order to differentiate one from another and attain better accuracy. Although there is no modulation on CW radar transmitted signal, the received signal behaves as a SSB modulated signal with a suppressed carrier caused by the Doppler frequency shift. In fact, this modulation is essential for proper function of ESPRIT algorithm.

The algorithm divides the array into two sub-arrays, which may partially overlap (three-element sub-arrays are used in this case). Each antenna can receive more signals $s_1(t)$ ... $s_d(t)$ in parallel. The incoming signals received by both sub-arrays and converted to the base-band can be expressed using formulae (4.3) and (4.4).

$$\mathbf{x}_1(t) = \begin{bmatrix}\mathbf{a}(\mu_1) & \dots & \mathbf{a}(\mu_d)\end{bmatrix}\begin{bmatrix} s_1(t) \\ \vdots \\ s_d(t)\end{bmatrix} + \mathbf{n}(t) = \mathbf{A}_1\mathbf{s}(t) + \mathbf{n}(t) \qquad (2.61/4.3)$$

$$\mathbf{x}_2(t) = \mathbf{A}_2\mathbf{s}(t) + \mathbf{n}(t) = \mathbf{A}_1\Phi\mathbf{s}(t) + \mathbf{n}(t) \qquad (2.62/4.4)$$

In (4.3) and (4.4), $\mathbf{x_i}(t)$ can be described as a base-band signal vector, while $\mathbf{A_1}$ and $\mathbf{A_2}$ represent the array steering matrix, formed by column vectors $\mathbf{a}(\mu_i)$. The additive Gaussian (white) noise is expressed by $\mathbf{n}(t)$ and $\mathbf{\Phi}$ represents the rotation operator described by formula (4.5), where μ_i represents spatial frequencies (4.6).

$$\mathbf{\Phi} = diag\begin{bmatrix} e^{j\mu_1} & \dots & e^{j\mu_d}\end{bmatrix} \qquad (2.63/4.5)$$

$$\mu_i = -\frac{2\pi f\Delta}{c}\sin\theta_i = -\frac{2\pi\Delta}{\lambda}\sin\theta_i \qquad (2.64/4.6)$$

where f and λ stand for the transmitted frequency and wavelength respectively, Δ represents the distance of two array elements and θ denotes the desired angle of arrival DOA. The rotation operator $\mathbf{\Phi}$ describes the influence of displacement of two sub-arrays. The main advantage of this

algorithm consists in the fact that the displacement error affects the DOA calculation merely negligibly and the algorithm is relatively fast (in comparison to other super resolution algorithms, such as MUSIC).

Though ESPRIT is capable of differentiating $M-1$ incident signals (M counts array elements) this advantage may be used later when more targets are present or while dealing with the multi-path propagation, which is not considered in this test set-up.

2.5.3 Calibration and Correction Method

Since neither antenna elements in the array nor inter-connecting cables and receiver channels are identical, the calibration of entire receiver and correction of the received signals are necessary. Many calibration techniques have already been published; e.g. in [21] and [22]. Due to the fact that the calibration has to be carried out under difficult conditions (at army shooting range), a relatively simple calibration technique has been deployed.

Considering only one incoming signal $s_1(t)$ and given that the radar requires correction, the formula (4.3) is modified in the following manner:

$$\mathbf{x}_r(t) = \mathbf{a}_r(\mu_1)s_1(t) + \mathbf{n}(t) \qquad (2.65/4.7)$$

$\mathbf{x}_r(t)$ represents the vector of signals received by the antenna array, $s_1(t)$ stands for the source signal and $\mathbf{n}(t)$ denotes the noise vector. In addition, $\mathbf{a}_r(\mu_1)$ symbolizes the antenna steering vector described by formula (4.8). The $\mathbf{a}_r(\mu_1)$ vector also includes all phase and amplitude errors (i.e. differences in antenna, cable and receivers parameters) and can be determined in the following fashion:

$$\mathbf{a}_r(\mu_1) = \begin{bmatrix} g_1 \\ g_2 e^{j\mu_1} \\ \vdots \\ g_M e^{j(M-1)\mu_1} \end{bmatrix} = diag\left(\mathbf{a}(\mu_1)\right)\mathbf{g} = \mathbf{A}(\mu_1)\mathbf{g} \qquad (2.66/4.8)$$

where $\mathbf{g}$ stands for the error vector, $\mathbf{a}(\mu_1)$ represents the ideal array steering vector, $\mathbf{A}(\mu_1)$ describes the diagonal array steering matrix and μ_1 embodies the spatial frequency defined by (4.6).

Considering formulae (4.7) and (4.8), the $\mathbf{x_r}(t)$ vector can be calculated:

$$\mathbf{x}_r(t) = \mathbf{A}(\mu)\mathbf{g}s_1(t) + \mathbf{n}(t) \qquad (2.67/4.9)$$

From (4.9), the error vector $\mathbf{g}$ can be expressed as:

$$\mathbf{g} = \frac{\mathbf{A}^{-1}(\mu)\mathbf{x}_r(t) - \mathbf{n}(t)}{s_1(t)} \qquad (2.68/4.10)$$

As the noise vector $\mathbf{n}(t)$ is unknown, formula (4.7) can be evaluated using proper estimation method for $\mathbf{g}$ and the received signals as a reference. The estimation of $\mathbf{g}$ can be, therefore, expressed using formula (4.11):

$$\hat{\mathbf{g}} = \sum_{n=1}^{N} \frac{\mathbf{A}^{-1}(\mu)\mathbf{x}_r(t_n)}{x_{rk}(t_n)} \qquad (2.69/4.11)$$

where N counts signal samples used for $\mathbf{g}$ estimation and $x_{rk}(t_n)$ represents the *k-th* element of vector $\mathbf{x_r}(t_n)$ selected as the reference. In our case, one measurement with the known angle of arrival θ was applied for evaluation of the error vector $\mathbf{g}$. Consequently, the received signals can be corrected using formula (4.12):

$$\mathbf{x}_c(t) = diag\left(\frac{1}{g_1} \quad \cdots \quad \frac{1}{g_M}\right)\mathbf{x}_r(t) \qquad (2.70/4.12)$$

Although this correction does not take into consideration the cross talk between antennas, the results show that the calibration is acceptable for our purpose, see Fig. 2.33.

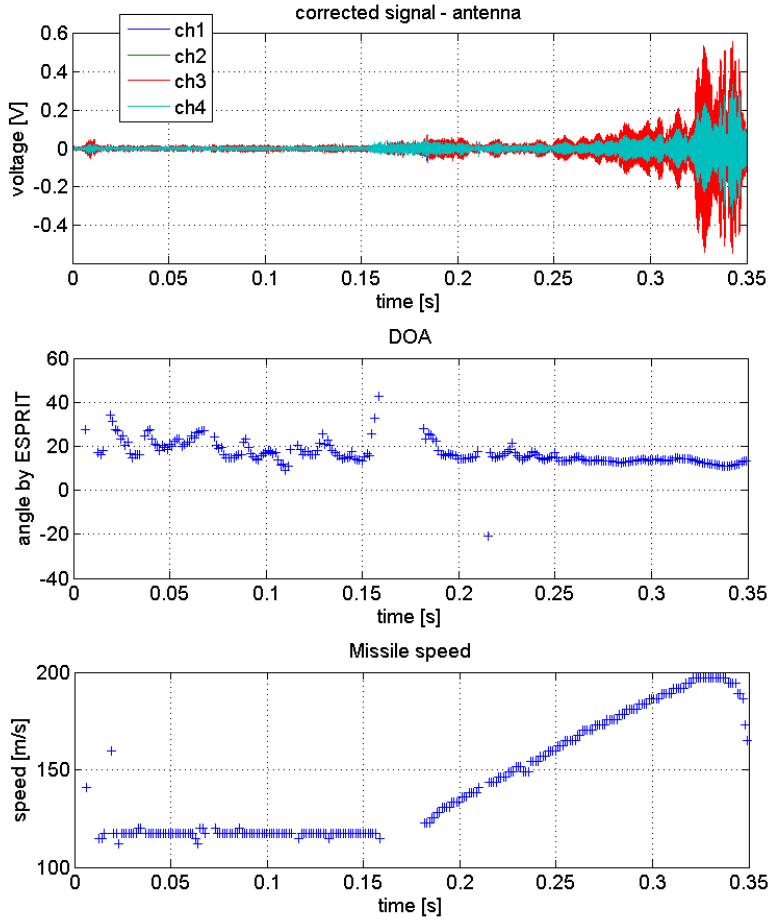

Fig. 2.33 Measured and calculated results, *DOA*=θ=18°.

2.5.4 Target Position Estimation

The sketch of simple test system consisting of only two DOA sensors can be seen in Fig. 2.34.

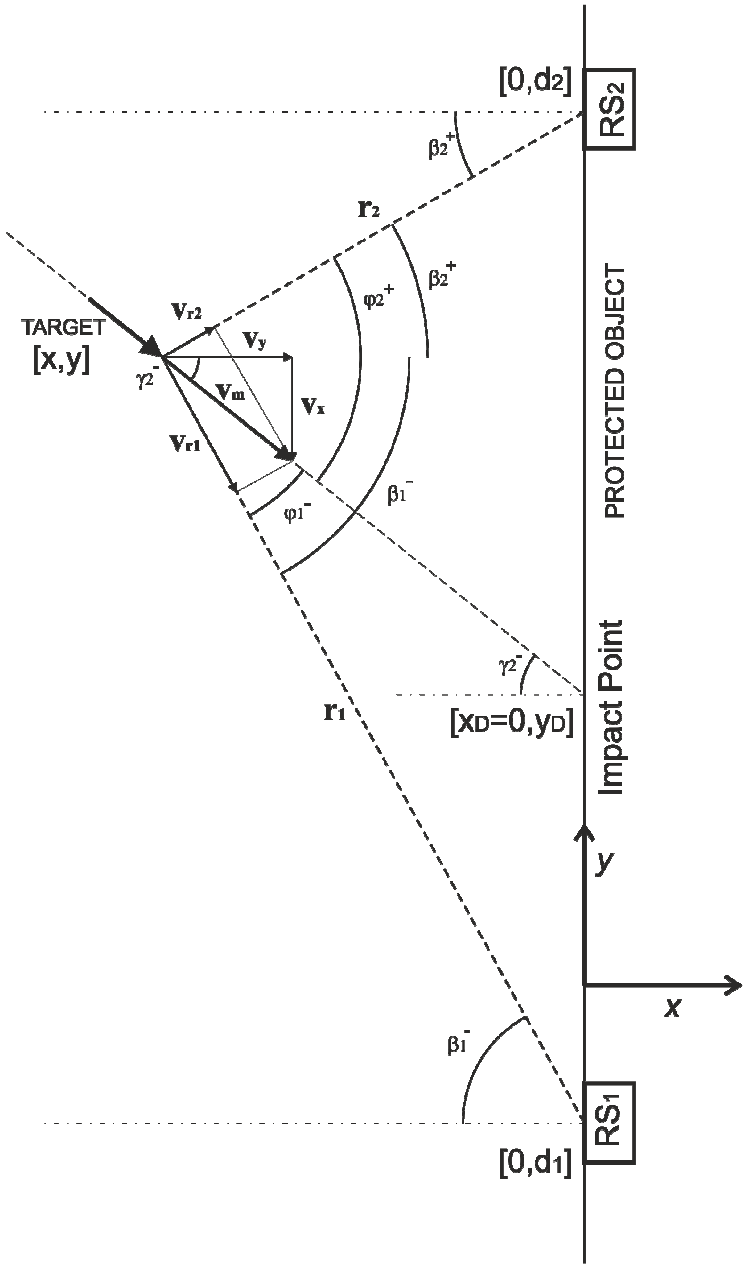

Fig. 2.34 Simple surveillance radar consisting of two DOA radar sensors.

The position of target is specified by intersection of two lines defined by two DOA values. Adding extra sensors and DOA values results in over-determination of corresponding equation system and can serve as a tool to attain more precise calculations of target parameters. When

using two radar sensors RS_1 and RS_2, the target position can be expressed by formulae (4.13) and (4.14):

$$x = \frac{d_1 - d_2}{\tan\beta_2 - \tan\beta_1} \qquad (2.71/4.13)$$

$$y = \frac{d_1 \tan\beta_2 - d_2 \tan\beta_1}{\tan\beta_2 - \tan\beta_1} \qquad (2.72/4.14)$$

In these equations, d_1 and d_2 stand for the radar sensor displacements in the y-axis, while β_1 and β_2 represent the target azimuths with respect to RS_1 and RS_2 respectively, see Fig. 2.34. The other DOA sensors are supposed to be fixed on neighboring sides of the protected vehicle too. This configuration enables both coverage of entire vehicle and detection of respective targets that are approaching from very steep angles, where sensor antennas usually show their minima.

Although several successive DOA measurements are sufficient for target trajectory calculations, more accurate results can be achieved by including the values of target radial velocity components as well. They can be measured by the CW radar with a good accuracy. This is especially significant in cases where the sensor-to-target distance highly exceeds the distance among radar sensors or in case of inconvenient situation geometry.

2.5.5 Trajectory Estimation

By measuring more target parameters and by taking into account the target flight 'history', it is possible to reach higher accuracy as well as the capability to estimate the impact point. As the equations describing the model are nonlinear, the extended Kalman filtration [23] was employed.

The applied tracking method can be divided into several steps. First, the future state is predicted and its covariance matrix is calculated.

In the presented case, the state vector $\mathbf{x}$ incorporates the target coordinates x,y and its velocity components v_x, v_y:

$$\mathbf{x} = \begin{bmatrix} x & y & v_x & v_y \end{bmatrix}^T \qquad (2.73/4.15)$$

The state transition matrix of the model $\mathbf{F}$ is described by (6), where dt stands for the discrete time step.

$$\mathbf{F} = \frac{\partial \mathbf{f}}{\partial \mathbf{x}} = \begin{bmatrix} 1 & 0 & dt & 0 \\ 0 & 1 & 0 & dt \\ 0 & 0 & 1 & 0 \\ 0 & 0 & 0 & 1 \end{bmatrix} \qquad (2.74/4.16)$$

In the second step of Kalman filtration process, the a priori estimated value of $\mathbf{x}$ is corrected using measured values (4.17) and model covariance matrix. The measurement vector is

composed of the measured azimuths β_1, β_2 and radial velocity components v_{r1}, v_{r2} measured by radar sensors RS_1 and RS_2, respectively:

$$\mathbf{y} = \begin{bmatrix} \beta_1 & \beta_2 & v_{r1} & v_{r2} \end{bmatrix}^T \tag{2.75/4.17}$$

The measurement function in the Kalman filter is expressed by equation (4.18):

$$\mathbf{h} = \begin{bmatrix} \arctan\dfrac{y-d_1}{x} \\ \arctan\dfrac{y-d_2}{x} \\ \dfrac{-v_x x - v_y (y-d_1)}{\sqrt{x^2 + (y-d_1)^2}} \\ \dfrac{-v_x x - v_y (y-d_2)}{\sqrt{x^2 + (y-d_2)^2}} \end{bmatrix} \tag{2.76/4.18}$$

The model measurement matrix is derived from (4.18) by means of partial derivatives:

$$\mathbf{H} = \frac{\partial \mathbf{h}}{\partial \mathbf{x}} = \begin{bmatrix} -\dfrac{y-d_1}{x^2 + (y-d_1)^2} & \dfrac{x}{x^2 + (y-d_1)^2} & 0 & 0 \\ -\dfrac{y-d_2}{x^2 + (y-d_2)^2} & \dfrac{x}{x^2 + (y-d_2)^2} & 0 & 0 \\ \dfrac{-v_x (y-d_1)^2 + v_y x (y-d_1)}{\left(x^2 + (y-d_1)^2\right)^{\frac{3}{2}}} & \dfrac{v_x x (y-d_1) - v_y x^2}{\left(x^2 + (y-d_1)^2\right)^{\frac{3}{2}}} & \dfrac{-x}{\sqrt{x^2 + (y-d_1)^2}} & \dfrac{-(y-d_1)}{\sqrt{x^2 + (y-d_1)^2}} \\ \dfrac{-v_x (y-d_2)^2 + v_y x (y-d_2)}{\left(x^2 + (y-d_2)^2\right)^{\frac{3}{2}}} & \dfrac{v_x x (y-d_2) - v_y x^2}{\left(x^2 + (y-d_2)^2\right)^{\frac{3}{2}}} & \dfrac{-x}{\sqrt{x^2 + (y-d_2)^2}} & \dfrac{-(y-d_2)}{\sqrt{x^2 + (y-d_2)^2}} \end{bmatrix} \tag{2.77/4.19}$$

Within the radar detection range, the above-mentioned algorithm is capable of target tracking. The impact point can be calculated by means of formula (4.20):

$$y_d = (x_d - x)\frac{v_y}{v_x} + y \tag{2.78/4.20}$$

where y_d is the horizontal coordinate of impact point, while x_d usually equals zero. The estimation error can be expressed via Kalman filter estimation covariance matrix and formulae (4.21) and (4.22):

$$\mathbf{E} = \begin{bmatrix} \dfrac{\partial y_d}{\partial x} & \dfrac{\partial y_d}{\partial y} & \dfrac{\partial y_d}{\partial v_x} & \dfrac{\partial y_d}{\partial v_y} \end{bmatrix} = \begin{bmatrix} -\dfrac{v_x}{v_y} & 1 & x\dfrac{v_y}{v_x^2} & -\dfrac{x}{v_x} \end{bmatrix} \tag{2.79/4.21}$$

$$VAR(y_d) = \mathbf{E}\tilde{\mathbf{P}}_k\mathbf{E}^T \tag{2.80/4.22}$$

2.5.6 Measured Results

The above-described sample of surveillance radar, consisting of two DOA sensors, was tested at army shooting range. At first, both radar sensors were calibrated according to (4.12). Test targets, i.e. RPG-7 missiles, were shot from the distance of about 50 m at the time t = 0 s. The data from both MISO radar sensors were recorded and subject to further processing.

The recorded data were used to calculate DOA values by means of the already mentioned ESPRIT method with 1024 samples window length and 1/4 overlay. The target radial velocity was measured by both sensors as well.

Figs. 2.35 –2.37 show results of one of the performed tests. In this case, the missile flew perpendicularly towards the sensor plane, and at the time t = 0.29 s, it passed right under RS_2 sensor (y_d = 3 m). Fig. 2.35 depicts the measured DOA time responses provided by RS_1 and RS_2 sensors. Fig. 2.36 provides comparisons of missile position calculated with the help of equations (4.13) and (4.14) and position estimated by the Kalman filter. The time response of estimated impact point can be seen in Fig. 2.37.

The presented results show a relatively good agreement between the expected and measured values. Considering the velocity of the target is roughly 160 m/s, the radar is capable of tracking the missile in the required near range from 13 m to 0 m. Calculations of impact point very quickly converge with the correct value y = 3 m. The primary problem of developed method consists in the employment of extended Kalman filter and its nonlinearity. If highly erroneous data are preset at the filter input, they cannot converge with the meaningful results within the given measurement time limit. Therefore, the proper moment to start the tracking algorithm is crucial and has to be determined carefully.

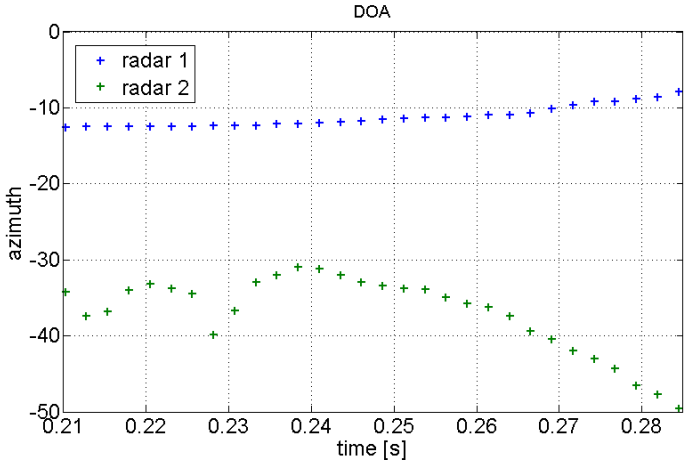

Fig. 2.35 Test No. BZ0022 – RS_1 and RS_2 DOA measurements.

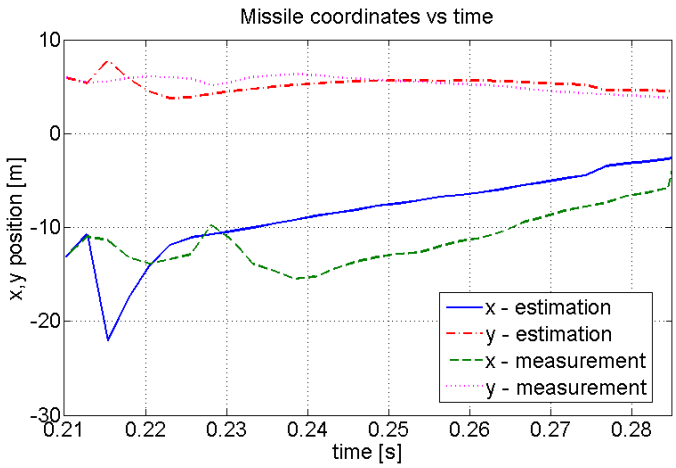

Fig. 2.36 Measured target position and its estimation by Kalman filter.

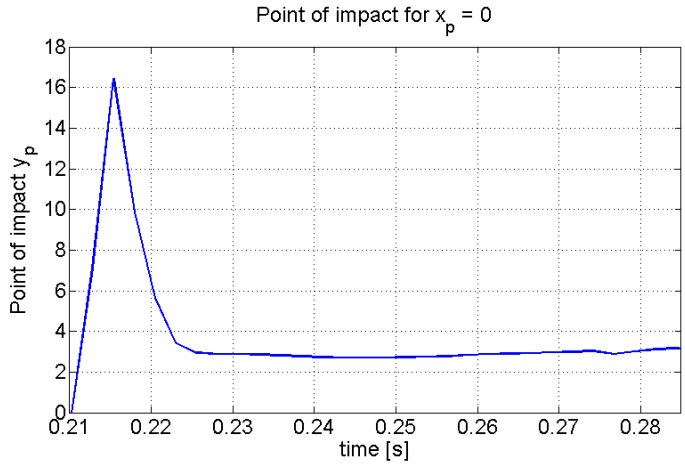

Fig. 2.37 Impact Point estimation provided by Kalman filter.

2.5.7 Conclusion

Regarding previous information about microwave curtain concepts, SR is the key component in ADS. Practical tests show that the surveillance radar based on DOA and radial velocity measurements is able to trace even very fast targets, flying in the close vicinity of sensors. The radar can calculate target trajectory, its velocity and impact point and is applicable in the developed defense system. Using more sensors enables to cover the entire protected vehicle as well as to monitor the targets approaching from very steep angles. Although the higher precision of DOA measurement can be achieved by more sophisticated calibration, the employment of PNS radar seems to provide more advantages. Apart from the direct distance measurement capability (which can contribute to accurate trajectory estimation), the PNS radar provides a better RFI immunity and separation of different radars by a unique PNS code.

3 Moving Target Simulator for CW Radar Calibration

As is stated in the Introduction, the development of CW radar sensors is demanding as to the quality of equipment, which can be used for testing of such sensors. Following chapters describe a method simulating a moving target with well-defined parameters using quite common microwave building blocks.

3.1 Simulator Design

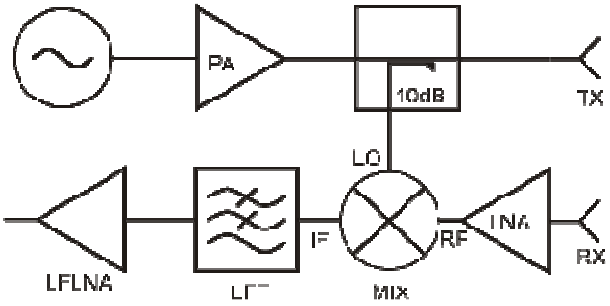

Fig. 3.1 Bloc diagram of analog CW Doppler radar.

There are three main possibilities for designing the calibrator that arise from the CW radar working principle, which are described further. In line with the radar in Fig. 3.1, the signal at the output of low-frequency filter can be stated as:

$$s_{bb}(t) = \frac{k_{rx} A_t R_t}{L_p} \cos\left(\frac{2\omega r_0}{c} + \frac{2\omega v_r t}{c} + \Psi - \Psi_{rt}\right) \tag{3.1}$$

In this equation, k_{rx} and Ψ symbolize the receiver conversion gain and general phase respectively, A_t stands for the amplitude of transmitted signal, R_t and Ψ_{rt} represent the magnitude and phase of reflection coefficient of the target, while L_p embodies the total propagation loss, including the influence of antennas. Besides, r_0 embodies the static target position at the time $t = 0$, while v_r stands for the radial target velocity with respect to the radar. If we consider any moving target, the base-band output signal can be expressed as:

$$s_{bb}(t) = A' \cos\left(\frac{2\omega v_r t}{c} - \Psi'\right) = A' \cos(\omega_D t + \Psi') \tag{3.2}$$

The moving target generates the output signal with the frequency equal to the Doppler frequency shift:

$$f_D = -\frac{2 v_r f_0}{c} \tag{3.3}$$

The prime objective of designed calibrator is to make the radar generate a comparable base-band signal, simulating the moving target even in the case when $v_r = 0$. The above-presented formulae reveal the ways how this can be achieved.

a) Amplitude modulation of R_t

Since the calibrator has to be based on the target modulation, the amplitude modulation of its reflection coefficient ($\approx RCS$) is likely to represent the easiest option. The modulation can be performed using the RF switch, which is able to change the R_t value between 0 (load) and 1 (short). The resulting base-band signal at the output of Doppler radar then equals ($r_0 = 0$, $v_r = 0$, static reflections being removed):

$$s_{bb}(t) = \frac{k_{rx} A_t}{L_p} \cos(\Psi - \Psi_{rt}) \sum_{n=1}^{\infty} R_n \sin(n\omega_{\mathrm{mod}} t) \tag{3.4}$$

The amplitude modulation of R_t results in the output frequency spectrum $n\omega_{mod}$, which can be used for calibration. However, when using this type of calibrator, it is necessary to solve the problem related to the $\cos(\Psi - \Psi_{rt})$ component. The amplitude of $s_{bb}(t)$ signal depends upon actual static phases in the system and can easily reach the zero value. This type of calibrator can be, with some caution, used for calibration of target velocity, yet cannot be used as a *RCS* reference.

b) Variations of r_0

Changes in static position of the target r_0 are identical to those incurred in the case of non-zero v_r value. The calibrators in question include moving parts able to simulate movements of the target. An example of such calibrator can be found in [5]. The disadvantages of this solution were described in Chapter 1.1.2.

c) Variations of Ψ_{rt}

The equation (3.1) shows that even if $r_0 = 0$ and $v_r = 0$, the $s_{bb}(t)$ signal can simulate the moving target, provided that Ψ_{rt} is time-dependent. This dependence can be performed by employing the structure according to Fig. 3.2.

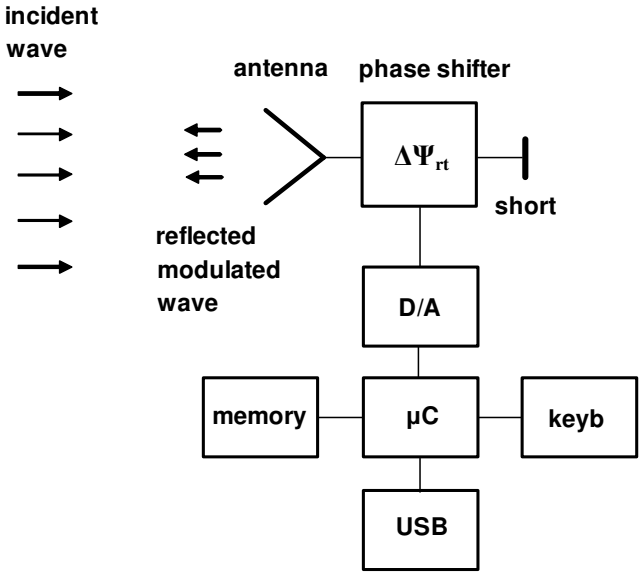

Fig. 3.2 Block diagram of designed calibrator.

The structure is based on the variable phase-shifter, which is connected between the antenna output and short-circuit. The incident wave passes through the phase-shifter, reflects at the short-circuit, goes the same way back and is eventually radiated in the direction towards the radar. In order to obtain the sinusoidal output signal simulating the constant target velocity and constant radar output Doppler frequency, the Ψ_{rt} time response should be linear:

$$\Psi_{rt}(t) = k_p t \tag{3.5}$$

The k_p parameter represents the required rate of phase changes:

$$k_p = \frac{d\Psi_{rt}}{dt} = \frac{\Delta\Psi_{rt}}{\Delta t} = \omega_{ds} = 2\pi f_{ds} \tag{3.6}$$

Hence, it is possible to calculate the required time Δt, during which the phase shifter should change its phase by $\Delta\Psi_{rt}$. The latter stands for the function of the required simulated Doppler frequency f_{ds} or the function of simulated target velocity v_{r2}:

$$\Delta t = \frac{\Delta\Psi_{rt}}{2\pi f_{ds}} = \frac{\Delta\Psi_{rt} c}{4\pi v_{rs} f_0} \tag{3.7}$$

As the signal passes through the phase-shifter twice, it is necessary to perform the phase-shift $\Delta\Psi = \pi$ within the time Δt, whereby the requirements for controlling the phase-shifter can be derived.

The best approximation of linear Ψ_{rt} time response is the saw-tooth waveform. The circuit changes the phase from 0 to π (or from α to $\alpha + \pi$), and then returns back to zero as quickly as possible. During the linear part of the course, the calibrator generates the required pseudo-

Doppler signal. Given that the transition to zero is very fast, the generated pseudo-Doppler spectrum reaches very high frequencies and can be easily removed.

3.2 Calibrator Realization

The designed calibrator was realized for testing of the developed CW radar sensors in the 11GHz frequency band. Its structure is based on the HMC931LP4E (Hittite) variable phase-shifter, while its phase is controlled by the TLC7528CDW (Texas Instruments) 8-bit dual DAC and an MCU. It was measured by means of VNA and stored in the MCU memory, because the phase-voltage dependence is non-linear. The MCU generates data for DAC using a phase to voltage calibration table, so that it forms a linear phase shift. An X-band horn antenna was employed. The realized calibrator set-up is depicted in Fig. 3.3.

The TLC7528 setting time amounts to 100 ns, hence the DAC is able to ensure a very rapid (typically. 1 μs) return-to-zero transition. Since TLC7528 circuit contains two DACs, the second DAC can be used as a variable voltage reference for optimum setting of the HMC931LP4E operating phase range. In fact, only 180º phase shift from approx. 400º of the available phase-shift is exploited. A simple keyboard enables to set various simulated target velocities and to switch between the approaching and receding target modes. The digital controlling circuits can be re-programmed by means of USB connection. Instead of analog phase-sifter, the digitally controlled MMIC can be applied. Easier control and linearity can be expected, yet the analog version usually provides finer phase-shift steps.

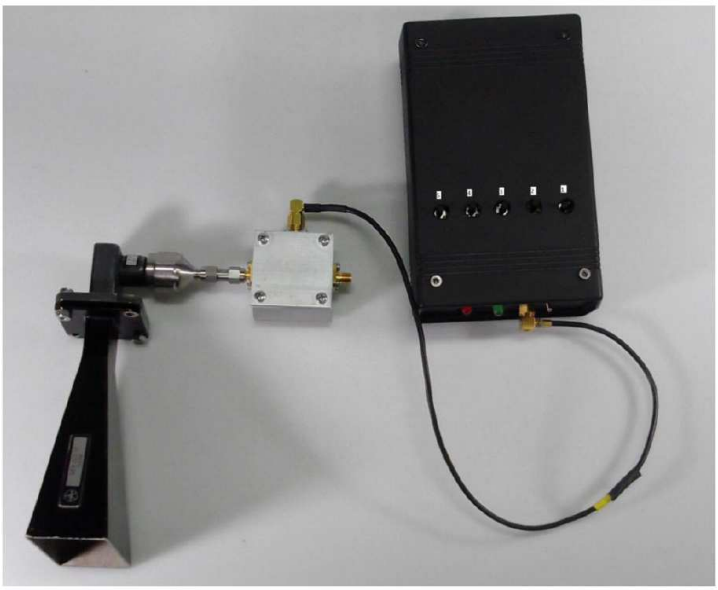

Fig. 3.3 Realized calibrator set-up.

3.3 Measured Results

The developed and realized calibrator was tested using two types of 11 GHz radars: basic analog CW radar and PNS radar. During the tests, the calibrator phase speed was set to 180°/167μs, which simulated the target velocity of 40.9 m/s and generated the pseudo-Doppler frequency of 3 kHz (for CW radar). Alternatively, the calibrator phase speed was set to 180°/250μs, which simulated the target velocity of 27.3 m/s and generated the pseudo-Doppler frequency of 2 kHz (for PNS radar). The calibrator was illuminated from the distance of 3 m and the radar output signals were recorded with the help of Agilent L4534A digitizer. The time response and spectrum of analog CW radar output signal are detailed in Figs. 3.4 and 3.5.

Both figures show that the radar output spectrum contains strong component that is expected to attain 3 kHz. The spectrum is stable and simulated target velocity is constant and well-defined. The higher f_D harmonics stem from the sub-optimally compensated phase-shifter non-linearity, yet for the expected employment of calibrator, this does not represent any major problem.

Figs. 3.6 and 3.7 show the time response and output spectrum of PNS radar (11 GHz center frequency, BPSK modulation, 25 MHz chip-rate, 100 MHz output band-width).

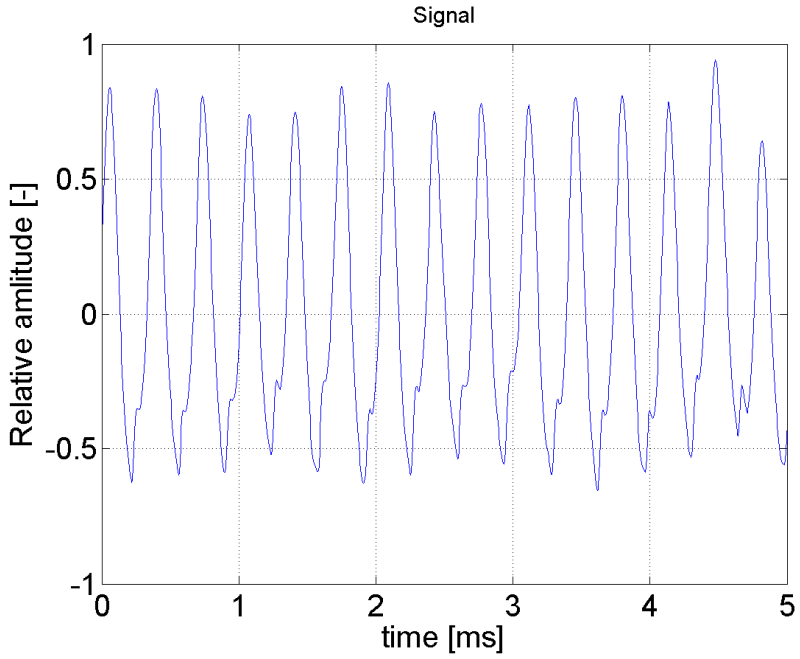

Fig. 3.4 Analog CW radar detects designed calibrator – relative output voltage.

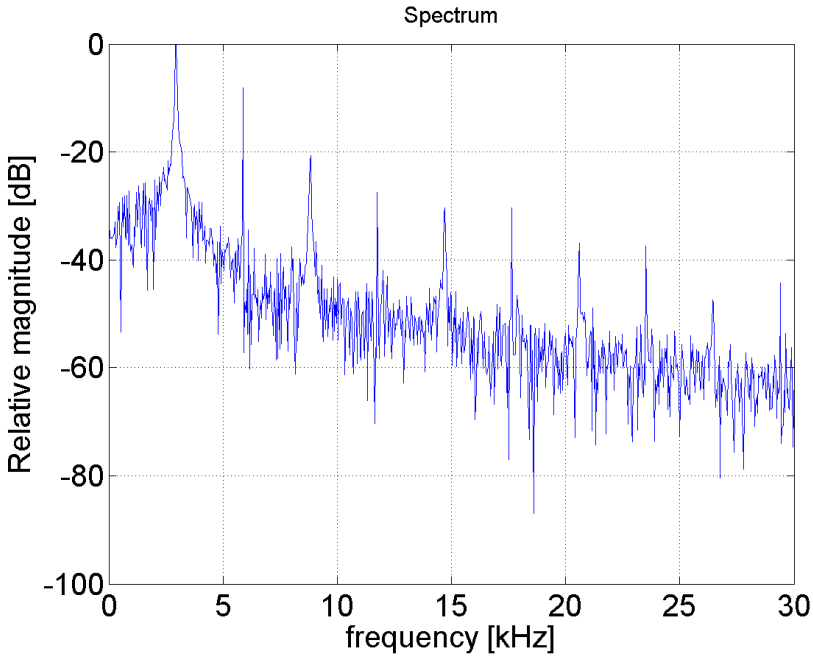

Fig. 3.5 **Analog CW radar detects designed calibrator – relative output spectrum.**

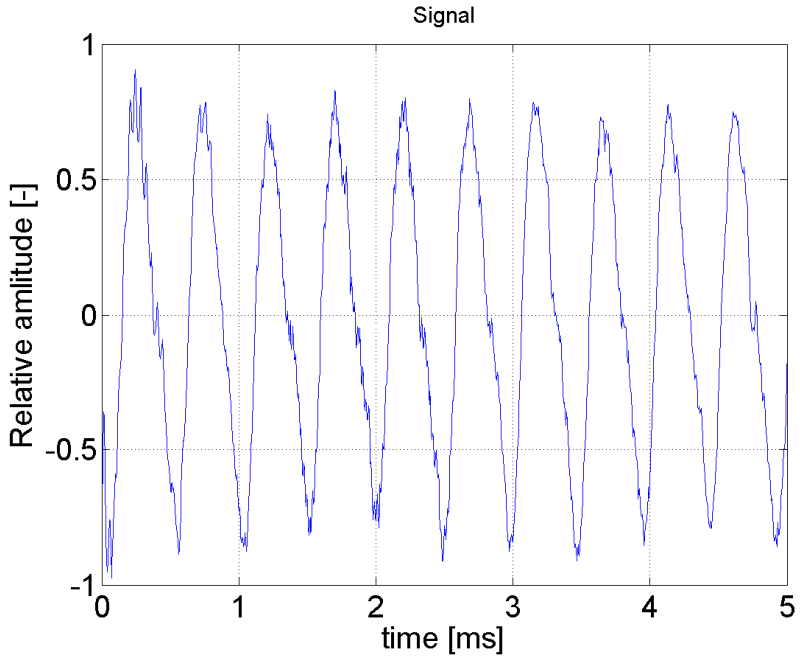

Fig. 3.6 **PNS radar detects designed calibrator – relative output voltage.**

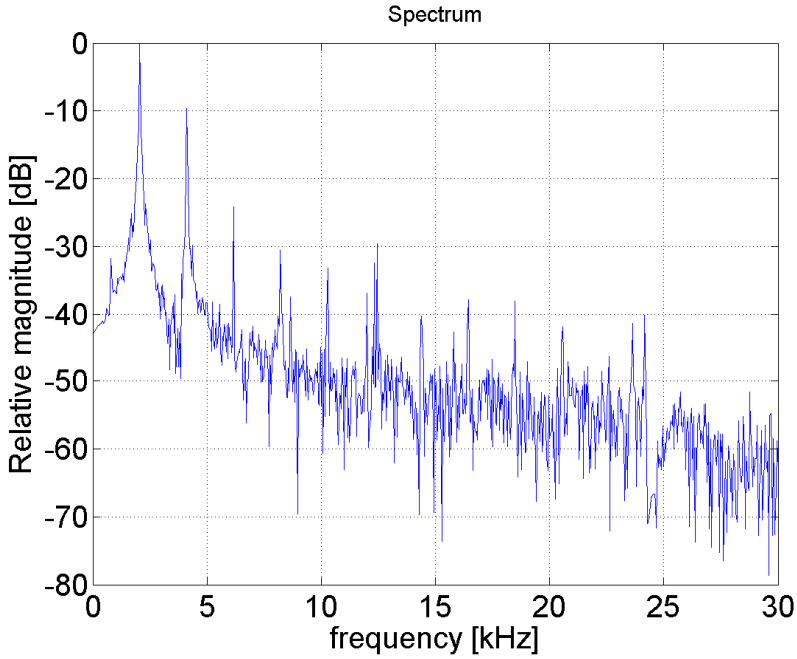

Fig. 3.7 PNS radar detects designed calibrator – relative output spectrum.

The results reveal that the time response and output spectrum demonstrate the strong 2 kHz component. This can serve as evidence that the calibrator is able to simulate moving targets even within a wider frequency band.

3.4 Conclusion

Proposed method substantially eased testing of CW radar sensors in laboratory conditions as well as at outdoor testing range. Simulated moving target has constant and well defined effective RCS and velocity.

The main drawbacks of this method are limited frequency range of developed calibrator and high static RCS (compare to RCS of simulated target), which depends on insertion loss of the phase shifter. However, effective RCS can be enlarged using another structure with separate TX and RX antennas of the calibrator and amplifier compensating for loss in the phase shifter. The frequency limitation depends mainly on the phase shifter and its linearity. Even though 10% bandwidth is not enough to have a wide band testing equipment, it is usually enough for conventional CW radar sensors.

4 Noise Analysis of CW Radar

Noise sources of CW radar sensors can be divided into categories listed below:

- Noise of linear or quasi-linear RF circuits of receiver,
- Phase-noise of local oscillator,
- Amplitude noise of local oscillator,
- Noise of LF circuits.

Following four subchapters treat each noise source separately; the total noise and its impact is discussed later on (together with simulated and measured results). Chapter 4.8 is focused on the radar self-test method.

4.1 Noise of Linear or Quasi-linear RF Receiver Circuits

The model of CW radar receiver comprising linear and quasi-linear RF circuits is depicted in Fig 4.1.

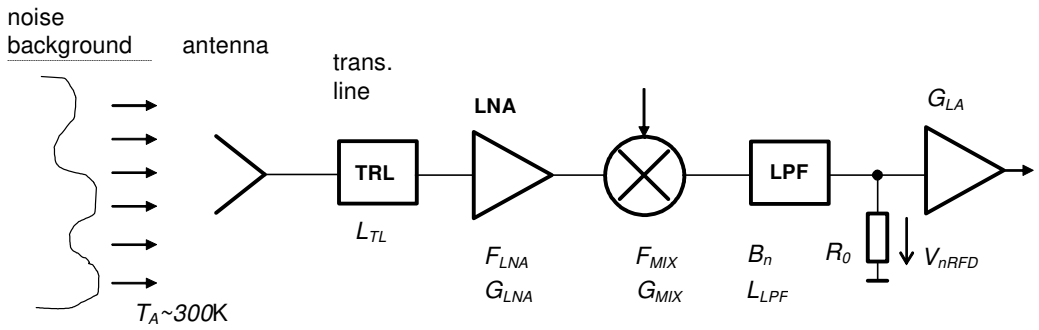

Fig. 4.1 Model of CW radar receiver including linear and quasi-linear RF circuits.

Apart from passive circuits (antenna, transmission line, filter), the model involves an LNA, mixer and LF amplifier that can be, in this case, treated as quasi-linear components. In Fig. 4.1, T_A represents the noise temperature of noise background, typically equal to T_A ~ 300 K. Due to that, the antenna can be modelled as a matched load with standard noise temperature T_0. Yet problems originating from the receiving antenna seeing the plasma of nearby explosions should not be omitted. Using higher reserves in the system design should be sufficient to deal with this problem.

Since the antennas in AD systems are frequently damaged or even destroyed by the activated counter-measure, they are connected using the sections of co-axial cables in order to protect the main parts of sensors. Their influence can be described by T_{TL} parameter (i.e. insertion loss).

The single side band noise power P_{nRFS} at the receiver output, caused by either linear or quasi-linear RF circuits, can be described by (4.1):

$$P_{nRFS} = \frac{kT_0 B_n G_{LNA} G_{MIX}}{L_{TL} L_{LPF}} + (L_{TL} - 1)\frac{kT_0 B_n G_{LNA} G_{MIX}}{L_{TL} L_{LPF}} + \\ + (F_{LNA} - 1)\frac{kT_0 B_n G_{LNA} G_{MIX}}{L_{LPF}} + (F_{MIX} - 1)\frac{kT_0 B_n G_{MIX}}{L_{LPF}} + \\ + (L_{LFF} - 1)\frac{kT_0 B_n}{L_{LPF}} \qquad (4.1/2.15)$$

In this formula, B_n describes the noise bandwidth, G_{LNA} and F_{LNA} represent the gain and noise figure of LNA respectively, while G_{MIX} and F_{MIX} stand for the conversion gain and noise figure of mixer. In addition, L_{LPF} represents the insertion loss of LF filter. If a high-gain LNA is used, P_{nRFS} power is dominantly determined by the first two items in (4.1) and the remaining items can be omitted. If a low-gain LNA or no LNA is utilized, influences of the mixer and LF filter can be significant and have to be included into calculations. In the case that the radar sensor does not reject the mirror frequencies, it is necessary to take into account the DSB noise power P_{nRF} in the manner indicated below.

$$P_{nRF} = 2P_{nRFS} \qquad (4.2)$$

The effective value of noise voltage V_{nRF} at the output of LF filter, loaded with the R_0 load and caused by the linear or quasi-linear RF components, can be expressed as:

$$V_{nRF} = \sqrt{P_{nRF} R_0} \qquad (4.3)$$

4.2 Phase Noise of Local Oscillator

In order to calculate the influence of local oscillator phase noise, the entire transmitting – receiving chain has to be considered. The transmitted signal $s_t(t)$ can be defined as:

$$s_t(t) = A_t \cos\left(2\pi f_o t + \varphi(t)\right) \qquad (4.4)$$

In this formula, A_t describes the signal voltage amplitude, f_o stands for the local oscillator frequency and $\varphi(t)$ is the phase-noise of local oscillator. The phase-noise is a random process with power spectral density $S_\varphi(f)$.

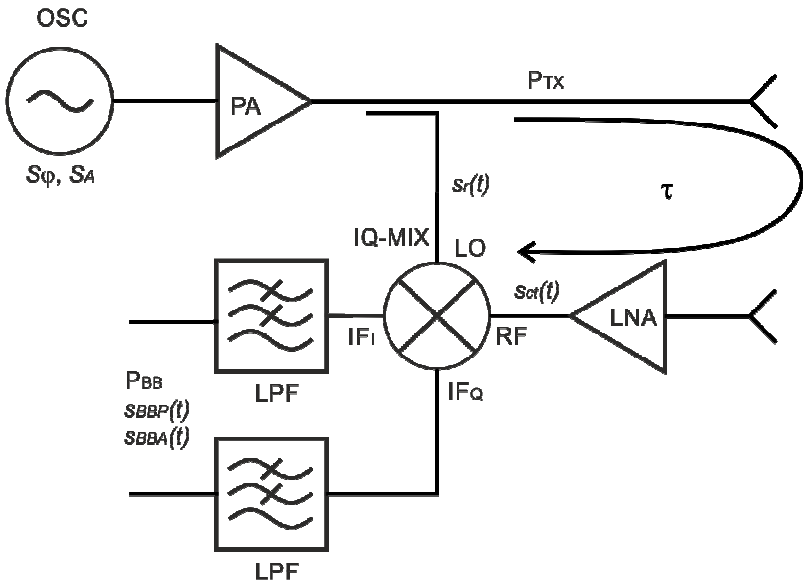

Fig. 4.2 Block diagram of basic analog CW radar sensor.

One part of the transmitted signal is used as a reference signal $s_r(t)$ and is brought into the mixer LO input.

$$s_r(t) = A_r \cos(2\pi f_o t + \varphi(t)) \tag{4.5}$$

In addition to the signal reflected from the target, there is always a cross-talked signal $s_{ct}(t)$ at the mixer input. With a different amplitude A_{ct}, it is in fact an attenuated copy of transmitted signal delayed by τ (with respect to the reference signal):

$$s_{ct}(t) = A_{ct} \cos(2\pi f_o (t-\tau) + \varphi(t-\tau)) \tag{4.6}$$

After down-conversion, the complex base band (BB) signal can be described as:

$$s_{BBP}(t) = A_{BB} e^{j(2\pi f_0 \tau + \Delta\varphi(t,\tau))} \tag{4.7}$$

while

$$\Delta\varphi(t,\tau) = \varphi(t) - \varphi(t-\tau) \tag{4.8}$$

represents the phase noise difference, A_{BB} stands for the signal amplitude at the down-converter's output.

Supposing $\Delta\varphi(t,\tau) << 1$, BB signal can be described using in-phase and quadrature components as:

$$s_{BBP\_I}(t) \cong A_{BB}\left[\cos(2\pi f_o \tau) - \Delta\varphi(t,\tau)\sin(2\pi f_o \tau)\right] \tag{4.9}$$

$$s_{BBP\_Q}(t) \cong A_{BB}\left[\sin(2\pi f_o \tau) - \Delta\varphi(t,\tau)\cos(2\pi f_o \tau)\right]. \tag{4.10}$$

The (4.9) and (4.10) signals consist of DC components (described by the first terms in brackets) and noise components. The power spectral density (PSD) of BB noise caused by the local oscillator phase-noise for in-phase (I) and quadrature (Q) components takes the form according to (4.11) and (4.12), respectively:

$$S_{nP\_I}(f) = P_{BB} \sin^2(2\pi f_o \tau) S_{\Delta\varphi(t,\tau)}(f) \tag{4.11}$$

$$S_{nP\_Q}(f) = P_{BB} \cos^2(2\pi f_o \tau) S_{\Delta\varphi(t,\tau)}(f) . \tag{4.12}$$

In (4.11) and (4.12), f represents the off-set frequency from the oscillator carrier frequency f_0; variable P_{BB} stands for the signal power at ideal IQ down-converter's outputs (we consider the same amplitude for I and Q signals), which can be expressed by (4.13):

$$P_{BB} = P_{TX} \frac{G_{MIX} G_{LFF} G_{AA} G_{LNA}}{L_{CAB}} G_{SYS} \tag{4.13}$$

According to [10], the spectrum of phase noise difference is then equal to

$$S_{\Delta\varphi(t,\tau)}(f) = 4 S_{\varphi}(f) \sin^2(\pi f \tau) \tag{4.14}$$

where $S_{\varphi}(f)$ represents the normalized PSD of local oscillator phase noise. With the help of (4.11) - (4.14), the PSD of IQ BB signals can be evaluated as

$$S_{nP\_I}(f) = 4 P_{BB} \sin^2(2\pi f_o \tau) \sin^2(\pi f \tau) S_{\varphi}(f) \tag{4.15}$$

$$S_{nP\_Q}(f) = 4 P_{BB} \cos^2(2\pi f_o \tau) \sin^2(\pi f \tau) S_{\varphi}(f) . \tag{4.16}$$

The formulae (4.15) and (4.16) show that PSD is the function of time-delay τ between the reference and cross-talked signals. The first sine/cosine terms cause oscillations of the noise power in both I and Q channels with τ changes. It is obvious that the maxima of I and Q channel signals are mutually shifted by 90 degrees. Therefore, the noise cannot be compensated by suitable phase shifts between the RX input and reference branches in the IQ receiver. The second sine terms describe changes of phase noise influences for frequencies situated further apart from the DC component. The maxima of I and Q components (4.15) and (4.16) equal

$$S_{nP}(f) = 4 P_{BB} \sin^2(\pi f \tau) S_{\varphi}(f) . \tag{4.17}$$

Assuming the noise bandwidth is known, the total noise power arising from phase noise can be calculated by integration of (4.17) (example for I channel):

$$P_{nP\_I} = \int_{BW} S_{nP}(f,\tau) df = = 4 P_{BB} \sin^2(2\pi f_o \tau) \int_{BW} \sin^2(\pi f \tau) S_{\varphi}(f) df \tag{4.18}$$

Considering the white phase and white frequency noise components, the phase noise PSD can be approximated [24-25]:

$$S_{\varphi}(f) \approx \frac{a_2}{f^2} + a_0 . \tag{4.19}$$

Where a_0 stands for white frequency noise coefficient and a_0 represents noise far from carrier (approx 1-10 MHz). The phase noise of oscillator can be approximated by more accurate formulae [26-28], but the aim was to provide a simple and acceptable formula. Assuming that $\pi f\tau << 1$, the resulting noise powers in the I and Q channels can be expressed as:

$$P_{nP\_I} \approx 8P_{BB}\pi^2\tau^2 \sin^2(2\pi f_o\tau)\cdot\left[\frac{a_0}{3}(f_H - f_L)^3 + a_2(f_H - f_L)\right] \tag{4.20}$$

$$P_{nP\_Q} \approx 8P_{BB}\pi^2\tau^2 \cos^2(2\pi f_o\tau)\cdot\left[\frac{a_0}{3}(f_H - f_L)^3 + a_2(f_H - f_L)\right]. \tag{4.21}$$

If condition $\pi f\tau << 1$ is not met (i.e. in the case of wide-band radars or radars with long transmission lines between receiver and antennas), the numerical integration takes place.

4.3 Amplitude Noise of Local Oscillator

The derivation of amplitude noise effects considers the cross-talked signal $s_r(t)$ described by (4.22), and the reference signal $s_{ct}(t)$ described by (4.23). In this case, with respect to $s_r(t)$, $s_{ct}(t)$ is delayed by τ, and both signals are affected by the amplitude noise $A_n(t)$ only. The amplitude-noise is a random process with a power spectral density $S_A(f)$.

$$s_r(t) = A_r(1 - A_n(t))\cos(2\pi f_o t) \tag{4.22}$$

$$s_{ct}(t) = A_{ct}(1 - A_n(t-\tau))\cos(2\pi f_o(t-\tau)) \tag{4.23}$$

The complex signal at mixer output can be expressed as follows:

$$s_{BBA}(t) = A_{BB}(1 - A_n(t))(1 - A_n(t-\tau))e^{j(2\pi f_0\tau)} . \tag{4.24}$$

The corresponding base-band signal can be described using I and Q components as:

$$s_{BBA\_I}(t) \cong A_{BB}\cos(2\pi f_o\tau)s_{AA}(t,\tau) \tag{4.25}$$

$$s_{BBA\_Q}(t) \cong A_{BB}\sin(2\pi f_o\tau)s_{AA}(t,\tau) \tag{4.26}$$

where

$$s_{AA}(t,\tau) = (1 - A_n(t))(1 - A_n(t-\tau)) \tag{4.27}$$

is the amplitude noise product with spectrum $S_{AA}(f)$.

The noise PSD caused by the local oscillator amplitude noise for I and Q components takes the form according to (4.28) and (4.29), respectively:

$$S_{nA\_I}(f) = P_{BB}\cos^2(2\pi f_o\tau)S_{AA}(f) \tag{4.28}$$

$$S_{nA\_Q}(f) = P_{BB}\sin^2(2\pi f_o\tau)S_{AA}(f). \tag{4.29}$$

In conformity with [11], S_{AA} can be articulated as:

$$S_{AA}(f) = 4S_A(f)\cos^2(\pi f\tau) + 2R_A(\tau)\delta(f) \tag{4.30}$$

where $R_A(\tau)$ is the amplitude noise autocorrelation . The last term in (4.30) can be omitted, for it represents the DC component that is filtered out. The total power attributable to oscillator amplitude noise can be calculated using (4.31).

$$P_{nA\_I} = \int_{BW} S_{nAM}(f)df = 4P_{BB}\cos^2(2\pi f_o\tau)\int_{BW}\cos^2(\pi f\tau)S_A(f)df \tag{4.31}$$

Considering the white noise and flicker noise, the approximation of oscillator amplitude noise spectrum is

$$S_A(f) \approx b_0 + \frac{b_1}{f}. \tag{4.32}$$

Putting (4.32) in (4.28) and integrating, the amplitude noise spectrum can be expressed as:

$$S_{nA\_I}(f) = 4P_{BB}\cos^2(2\pi f_o\tau)\cos^2(\pi f\tau)\left(b_0 + \frac{b_1}{f}\right). \tag{4.33}$$

The DSB power of amplitude noise is then:

$$P_{nA\_I} = 8P_{BB}\cos^2(2\pi f_o\tau)\int_{f_L}^{f_H}\cos^2(\pi f\tau)\left(b_0 + \frac{b_1}{f}\right)df. \tag{4.34}$$

The integrals presented above do not have analytic solutions. Yet since the radar bandwidth does not exceed 1 GHz with τ being in order of 10^0 ns usually and, therefore, $\tau f \ll 1$ in most of the cases, the second cosines are approximately equal to 1. That is why equations (4.33) and (4.34) can be simplified to (4.35) and (4.36).

$$P_{nA\_I} \approx 8P_{BB}\cos^2(2\pi f_o\tau)\int_{f_L}^{f_H}\left(b_0 + \frac{b_1}{f}\right)df = 8P_{BB}\cos^2(2\pi f_o\tau)\left[b_0 f + b_1\ln(f)\right]_{f_L}^{f_H} \tag{4.35}$$

$$P_{nA\_Q} \approx 8P_{BB}\sin^2(2\pi f_o\tau)\left[b_0 f + b_1\ln(f)\right]_{f_L}^{f_H} \tag{4.36}$$

4.4 Noise of LF Circuits

The employment of amplification at base band rather than at RF/IF blocks enables to gain advantages of removal of DC component from cross-talked signals on the one hand and cheap gain ratio (price per dB of gain) on the other hand. Given that the amplitudes of LF voltages at both mixer and LF filter output can reach very low levels, it is necessary to connect a low-noise LF amplifier in front of A/D processing. The low-noise operational amplifier (LT1028, Linear Technology) was used in our measurement; see Fig. 4.3.

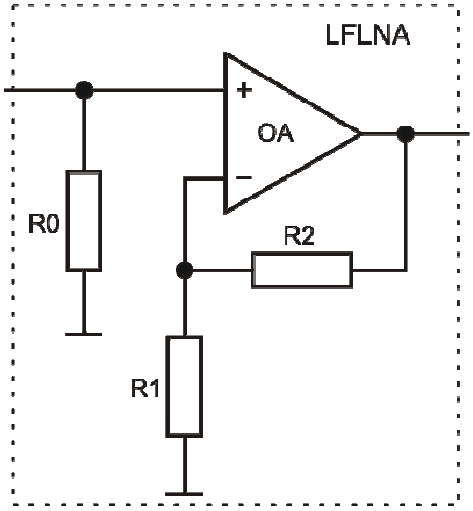

Fig. 4.3 Low-noise LF amplifier based on OA.

For this circuit, the manufacturer declares [29] that the effective value of noise voltage V_{nLF} referred to the input reaches the value:

$$V_{nLF} = \sqrt{B_n\left[e_n^2 + e_{nR}^2 + (i_n R_{eq})^2\right]} \tag{4.37}$$

In this formula, e_n stands for the input noise voltage of the given OA (its value is stated in [nV.Hz$^{-1/2}$]) and i_n represents the input noise current of the given OA (its value is indicated in [pA.Hz$^{-1/2}$]). The values of noise voltages generated by resistors can be calculated by means of formulae (4.38) and (4.39).

$$e_{nR} = \sqrt{4kT_0R_{eq}} \tag{4.38}$$

$$R_{eq} = \frac{R_0}{2} + \frac{R_1R_2}{R_1 + R_2} \tag{4.39}$$

For better noise power summation, the noise power of low frequency components follows formula (4.40):

$$P_{nLF} = \frac{V_{nLF}^2}{R_0} \tag{4.40}$$

Sufficient gain is usually provided by the first amplifier, thus the noise of later stages can be neglected.

4.5 Resulting Noise Parameters

The resulting noise power P_{nT} can be defined as a sum of all noise powers:

$$P_{nT} = P_{nA} + P_{nP} + P_{nRF} + P_{nLF} \tag{4.41}$$

The noise voltage then accounts for

$$V_{nT} = \sqrt{P_{nT} R_0} \tag{4.42}$$

The measurable noise voltage V_{nTo} at LF amplifier output can be simply calculated by multiplying V_{nT} by the voltage gain A_L at the LF amplifier:

$$V_{nTo} = A_L V_{nT} \tag{4.43}$$

Although the summation of noise sources at receiver output is uncommon (the receiver input is calculated instead), it gives two distinct advantages:

- Proper selection of the ADC based on actual noise floor at the receiver output,
- Easy comparison of theoretical and directly measured values (in the case of voltages).

For radar system calculations, it might be beneficial to know the total noise figure of receiver F_{RXt} that comprises influences of all above-described noise sources:

$$F_{RXt} = \frac{V_{nT}^2}{R_0} \frac{L_{TL} L_{LPF}}{k T_0 B_n G_{LNA} G_{MIX}} \tag{4.44}$$

Eventually, it is possible to define the total equivalent noise temperature at receiver T_{eRXt}:

$$T_{eRXt} = (F_{RXt} - 1) T_0 \tag{4.45}$$

4.6 Experiment I – Measurement of Amplitude Noise

4.6.1 Measurement Test Set-up

This measurement was reported in [30], where we assumed that the measured noise power had a dominant phase noise component. Further investigation revealed that the amplitude noise of local oscillator exceeded the phase noise for low radar BW and low time delay τ (in terms of ns).

Given that a similar DRO was used in the latter experiment and its phase and amplitude noise PSD were measured, it was possible to compare the measurement with recalculated values.

Unfortunately, the new noise PSDs of PLL oscillator were unavailable, thus DRO results are presented only.

Tabs. 4.1 and 4.2 list all principal parameters that were incorporated into the calculations.

Parameter	Description	Value	Unit
P_{TX}	transmitted power	21.5	dBm
G_{AA}	cross-talk gain	-43	dB
G_{AAW}	cross-talk gain with reflection wall	-36	dB
T_0	standard noise temperature	290	K
F_{LNA}	noise figure of RF pre-amplifier	1.8	dB
G_{LNA}	gain of RF pre-amplifier	16.5	dB
G_{MIX}	conversion gain of mixer	-6.5	dB
F_{MIX}	noise figure of mixer	6.5	dB
L_{TL}	transmission line loss	2	dB
L_{LPF}	low pass filter insertion loss	1	dB
f_L	noise bandwidth – low frequency	10^3	Hz
f_H	noise bandwidth – high frequency	$20 \cdot 10^3$	Hz
$B_n = f_{bh} - f_{bl}$	noise bandwidth, SSB	$19 \cdot 10^3$	Hz
e_n	input noise voltage of LT1028	1.2	$nV.Hz^{-}_{1/2}$
i_n	input noise current of LT1028	1.8	$pA.Hz^{-}_{1/2}$
R_0	load resistance	50	Ω
R_1	feedback resistor, 1st stage	10	Ω
R_2	feedback resistor, 1st stage	1000	Ω
A_L	voltage gain of LF amplifier	69.5	dB

Tab. 4.1 Parameters of tested radar sensor.

Type	f_c [Hz]	$S_\varphi(f)$ [Hz^{-1}]	$S_{AA}(f)$ [Hz^{-1}]
DRO	11.018	$3.2e\text{-}14+0.4/f^2$	3.2e-15+(1e-10)/f

Tab. 4.2 Parameters of used local oscillator.

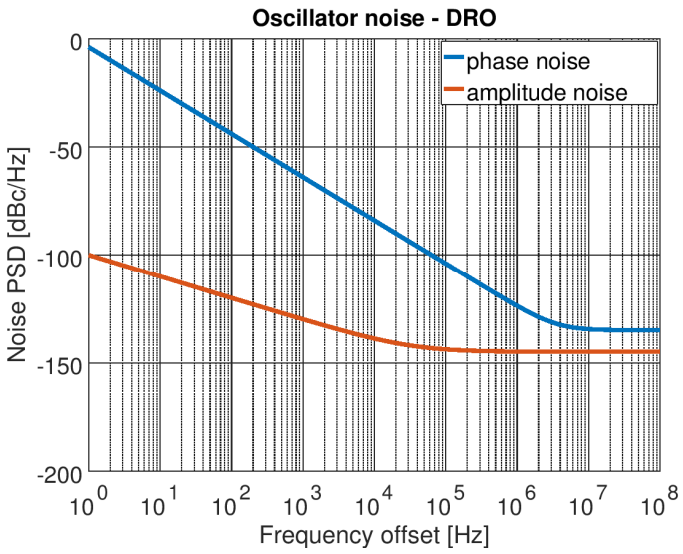

Fig. 4.4 **Approximations of amplitude and phase noise PSD of DRO as function of frequency offset.**

For measurement purposes, it is useful to separate voltages V_{nLF} and V_{nLR} corresponding to the LF amplifiers' noise and RF linear and quasi-linear components' noise, respectively, from (4.41) and thus form a linear delay-independent voltage:

$$V_{nLR} = \sqrt{V_{nLF}^2 + V_{nRF}^2} \tag{4.46}$$

The latter voltage can be measured by two matched loads replacing the antennas (therefore $G_{AA} = 0$, $P_{BB} = 0$, $P_{nP} = 0$ and $P_{nA} = 0$). As V_{nLF} can be easily calculated or measured from the known V_{nLR}, the value of V_{nRF} can be determined.

The remaining parts of (4.41), i.e. the amplitude and phase noise power, can only be evaluated together and with a varying τ. This remaining noise voltage from nonlinear components is expressed from (4.41) as:

$$V_{nN} = \sqrt{V_{nT}^2 - V_{nLF}^2 - V_{nRF}^2} \tag{4.47}$$

The V_{nN} measurement requires that τ has to vary by small increments (i.e. typically 10^1 *ps*), so it is possible to find the voltage maximum. A new type of noise measurement based on the employment of reflecting wall was proposed and verified for case when no suitable phase-shifter is available. The reflecting metallic wall was located in front of the radar antennas, while the distance between antennas and wall was subject to changes (in terms of millimetres); see Fig. 4.5.

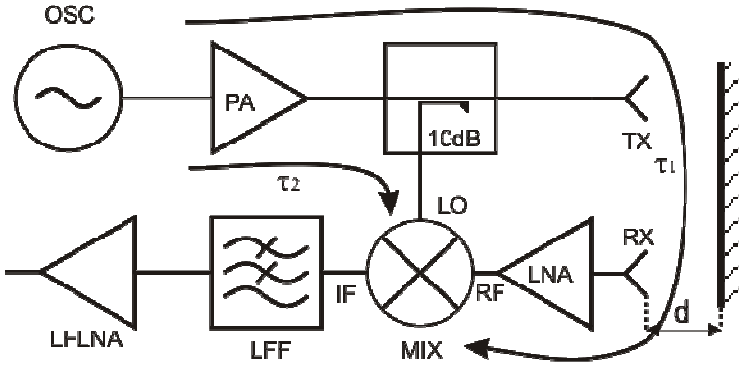

Fig. 4.5 Measurement setup of a CW radar with $\tau = \tau_1 - \tau_2$.

The time delays τ_1 between the oscillator and mixer RF input on the one hand and τ_2 between the oscillator and mixer LO input on the other hand were measured using a microwave oscilloscope (τ_1 was measured for the entire range of reflecting wall positions). If such microwave oscilloscope is unavailable, it is possible to use VNA in time delay measurement mode. The effective values of all noise voltages were measured by digital oscilloscope.

4.6.2 Measurement Results

Fig. 4.6 shows the comparison of calculated and measured $V_{nTo} = f(\tau)$ dependences that the minimum V_{nTmo} and maximum V_{nTMo} values can be read from. Fig. 4.7 provides important insight into the noise behaviour for a wider time delay range and for all noise components separately.

Given the measured values of V_{nTmo}, V_{nTMo}, V_{nLR} and V_{nLF}, it is possible to calculate the noise voltage of RF components V_{nRF}, maximum V_{nNM} and minimum V_{nNm} voltage of non-linear components:

$$V_{nRF} = \sqrt{V_{nLR}^2 - V_{nLF}^2} \tag{4.48}$$

$$V_{nNM} = \sqrt{V_{nTM}^2 - V_{nLR}^2} = \sqrt{\left(\frac{V_{nTMo}}{A_L}\right)^2 - V_{nLR}^2} \tag{4.49}$$

$$V_{nNm} = \sqrt{V_{nTm}^2 - V_{nLR}^2} = \sqrt{\left(\frac{V_{nTmo}}{A_L}\right)^2 - V_{nLR}^2} \tag{4.50}$$

In these formulae, V_{nTmo} and V_{nTMo} represents the minimum and maximum measured values of $V_{nTo} = f(\tau)$, and A_L denotes the LF amplifier voltage gain.

Even though it is impossible to evaluate the amplitude and phase noises separately, it is obvious from Fig. 4.7 that the phase noise is much lower than the amplitude noise. Therefore it can be concluded that the maximum noise voltage, which is due to the amplitude noise $V_{nAM} \approx V_{nNM}$ and

V_{nNm}, is a residual noise voltage caused by the phase noise, yet it does not necessarily represent the phase noise maximum.

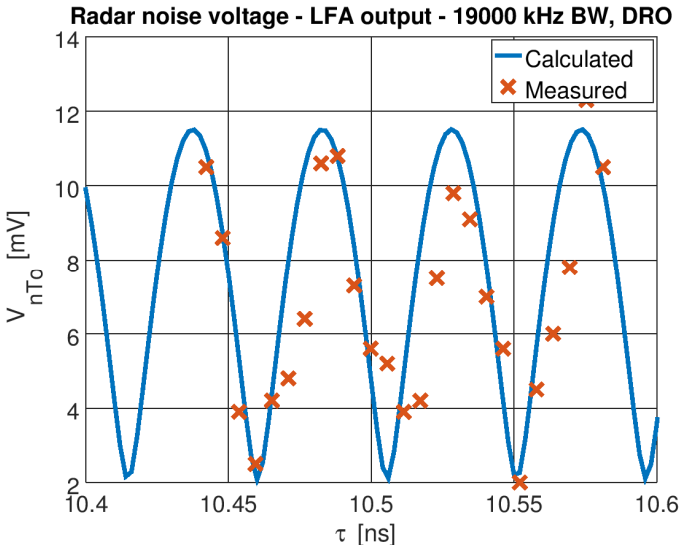

Fig. 4.6 **Resulting noise voltage as function of time delay τ (DRO based sensor with reflecting wall).**

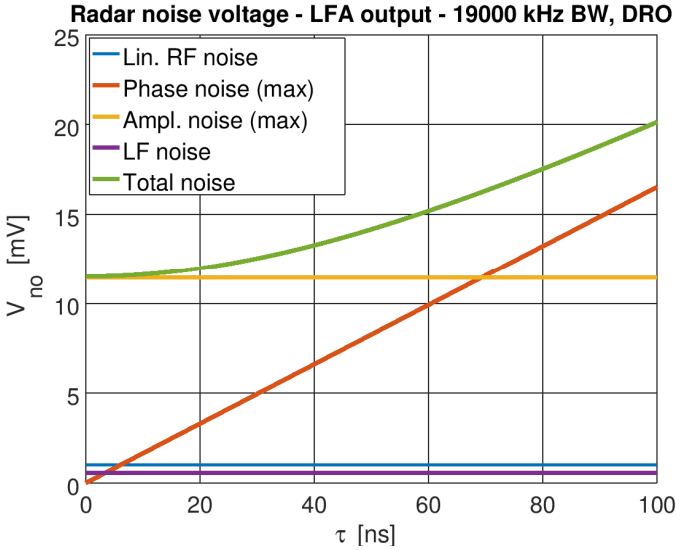

Fig. 4.7 **Calculated total noise and noise components for wide range of time delay τ (DRO based sensor with reflecting wall).**

The noise voltages of individual contributors (results from both measurement and theoretical values) are depicted in Tab. 4.3.

Parameter	DRO	DRO
	Calculated	Measured
P_{nRF} [W]	$2.4\ 10^{-15}$	$6.5\ 10^{-15}$
V_{nRF} [V]	$3.4\ 10^{-7}$	$5.7\ 10^{-7}$
P_{nNM} [W]	$2.9\ 10^{-13}$	$3.5\ 10^{-13}$
V_{nNM} [V]	$3.8\ 10^{-6}$	$4.1\ 10^{-6}$
P_{nPM} [W]	$6.8\ 10^{-15}$	n. a.
P_{nAM} [W]	$2.9\ 10^{-13}$	n. a.
V_{nLF} [V]	$1.8\ 10^{-7}$	$2.7\ 10^{-7}$
V_{nTM} [V]	$3.9\ 10^{-6}$	$4.2\ 10^{-6}$
V_{nTMo} [V]	$1.2\ 10^{-2}$	$1.2\ 10^{-2}$
V_{nLR} [V]	$3.9\ 10^{-7}$	$6.3\ 10^{-7}$
$A_L V_{nLR}$ [V]	$1.2\ 10^{-3}$	$1.9\ 10^{-3}$

Tab. 4.3 Calculated and measured noise parameters –reflecting wall (G_{AAW} = -36 *dB*, τ = 10.5 *ns*).

The table shows that in the case of high cross talk (-36 dB), the majority of noise is caused by the local oscillator amplitude noise, which exceeds other noise sources power by the factor of 100. Nonetheless, the maximum power due to the local oscillator phase noise is at the same level as other noise sources, which may cause measurement errors unless it is properly taken into account.

There is no proven correlation between the power maxima attributable to the amplitude and phase noise. This may lead to two extreme situations: Firstly, the amplitude noise power is in-phase (with respect to τ) with phase noise. In this case, the phase noise is hidden in amplitude noise and its impact can be neglected. Secondly, the amplitude noise power maxima are located exactly at the phase noise minima. In this case, the phase noise raises the minimum achievable noise power. Moreover, there is a difference between the power measured without local oscillator connected to the receiver and the power with local oscillator connected (which is the same as in the first case).

During the operation (with no reflecting wall), lower G_{AA} values have to be considered. In addition, the time-delay τ is reduced by ca. 1.5 ns. The calculated and measured operational noise parameters can be seen in Tab. 4.4 (G_{AA} = -43 *dB*, τ = 9.0 *ns*) and Fig. 4.8. Some noise parameters, including the specific value amplitude and phase noise dependant on specific value of τ, are unavailable due to their nature. However, theoretical results can provide estimation of the worst case situation as well as achievable results. The last four parameters were calculated using (4.44) and (4.45). The inputs involved the total maximum noise voltage V_{nTM} and noise voltage of linear components V_{nLR} for maximum and minimum noise figure (F_{RXM}, F_{RXm}), respectively.

Parameter	DRO	DRO
	Calculated	Measured
P_{nRF} [W]	2.4 10^{-15}	6.5 10^{-15}
V_{nRF} [V]	3.4 10^{-7}	5.7 10^{-7}
P_{nNM} [W]	5.9 10^{-14}	n. a.
V_{nNM} [V]	1.7 10^{-6}	n. a.
P_{nPM} [W]	9.9 10^{-16}	n. a.
P_{nAM} [W]	5.9 10^{-14}	n. a.
V_{nLF} [V]	1.8 10^{-7}	2.7 10^{-7}
V_{nTM} [V]	1.8 10^{-6}	n. a.
V_{nTMo} [V]	5.2 10^{-3}	n. a.
V_{nLR} [V]	3.9 10^{-7}	6.3 10^{-7}
$A_L V_{nLR}$ [V]	1.2 10^{-3}	1.9 10^{-3}
T_{eRXM} [K]	40,000	n. a.
T_{eRXm} [K]	1,650	n. a.
F_{RXM} [dB]	21.4	n. a.
F_{RXm} [dB]	8.2	n. a.

Tab. 4.4 **Calculated and measured noise parameters –operation (G_{AA} = -43 *dB*, τ = 9 *ns*).**

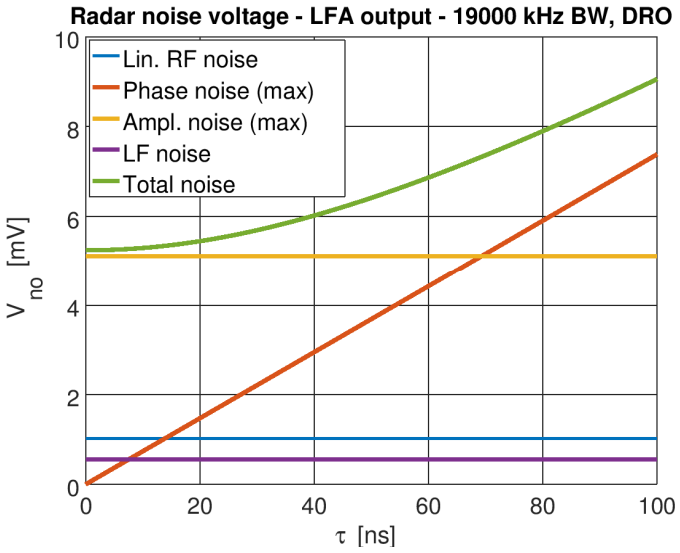

Fig. 4.8 **Calculated total noise and noise components for wide range of time delay τ (DRO based sensor – operation).**

4.6.3 Conclusion of Experiment I

As all parameters presented in Tabs. 4.3 and 4.4 correspond to the noise signals, there is an acceptable agreement between calculations and measurements. Besides, both calculated and measured results indicate a considerable potential influence of the amplitude and phase-noise on the system noise parameters. The CW radar structures enable the reduction of this influence to zero by ensuring the optimum τ. However, this compensation cannot be applied in radar systems with quadrature demodulation. In practice, the time delay of cross-talked signal can vary due to external factors, such as rain drops on antenna radoms. Therefore, the optimum phasing has not been applied so far and the system design was based on maximum values corresponding to formula (4.43) for maximum total noise voltage V_{nTM}.

During the operation, the noise voltage at radar sensor output attains levels between V_{nTMo} (being the upper limit corresponding to the maximal influence of amplitude noise) and $A_L(V_{nLR} + V_{nNm})$ (i.e. the noise voltage of low frequency components plus some residual voltage due to phase noise). For higher time delay τ or higher bandwidth, the impact of phase noise may overweight as it is shown in Chapter 4.7.

4.7 Experiment II – measurement of both amplitude and phase noise in system with IQ mixer

The second experiment regarding the impact of local oscillator's noise reveals conditions under which either amplitude or phase noise of local oscillator dominates the radar system set-up. The radar system was adopted to show and measure this behavior clearly, even though it is not used in this operational configuration.

4.7.1 Test Set-up Description

Fig. 4.9 shows the block diagram of measurement set-up that consists of the basic radar structure common to all CW-type versions, and additional components needed for performed tests. The radar TX involves the DRO or PLL-type local oscillator, PA power amplifier and power splitter dividing the signal to TX output and reference branch. The RX branch is composed of a coherent IQ down-converter fed by the reference signal from one output of TX splitter and followed by LF filtering-amplifying branches.

To achieve the required time-delay values necessary to distinguish between amplitude and phase noise, the test part of measurement set-up includes a set of co-axial cable sections with different lengths (1 – 30 m), and a variable length strip-line (to measure little time-delay differences). A set of RF amplifiers is used to compensate for the high insertion loss of concerned time-delay components. The entire test circuit affects the noise calculation in the way specified below.

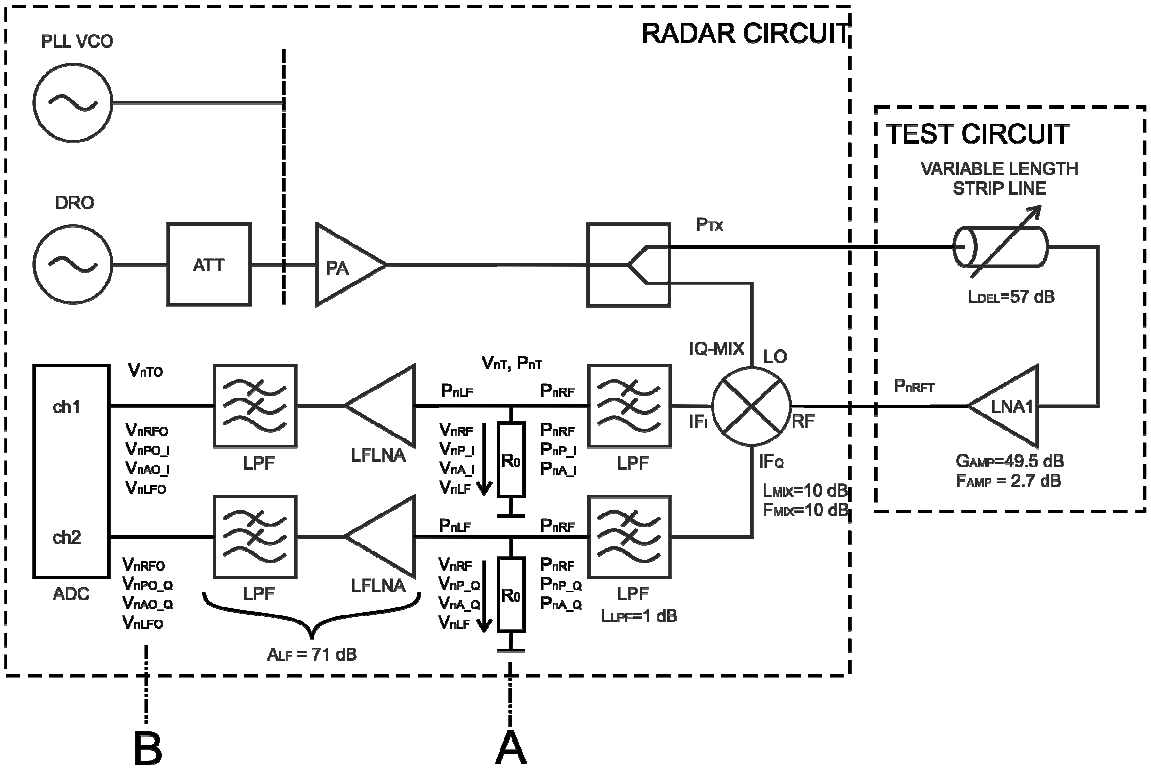

Fig. 4.9 **Block diagram of measurement set-up; variables are placed in close proximity to points they relate to.**

According to Fig. 4.9, the P_{nRF} total noise power generated by linear RF components at the filtered IQ demodulator outputs (considering output LP filters and both sidebands) can be written in the following manner (4.51).

$$P_{nRF} = 2P_{nRFSSB} = 2\left(P_{nRFT}G_{SYS} + P_{nRFSYS}\right) \tag{4.51}$$

In this formula, P_{nRFT} represents the noise power at the test circuit output and P_{nRFSYS} and G_{SYS} stand for the output noise power and gain of RF radar circuits, respectively.

The noise power of test circuit is further expressed in (4.52):

$$\begin{aligned} P_{nRFT} &= kT_0B_n\left(L_{DEL}-1\right)\frac{G_{AMP}}{L_{DEL}} + \\ &+ kT_0B_n\left(F_{AMP}-1\right)G_{AMP} \end{aligned} \tag{4.52}$$

where B_n stands for the noise bandwidth; L_{DEL} incorporates the loss of inserted cable and variable length strip line as well as attenuators used for cable loss compensation. G_{AMP} and F_{AMP} symbolize respectively the total gain and noise figure of used amplifiers.

The noise power of RF radar circuits takes into consideration the mixer gain G_{MIX}, mixer noise figure F_{MIX} and losses in the low pass filter L_{LPF}:

$$P_{nRFSYS} = kT_0B_n\frac{(F_{MIX}-1)G_{MIX}}{L_{LPF}} + \\ + kT_0B_n\frac{(L_{LPF}-1)}{L_{LPF}} \tag{4.53}$$

$$G_{SYS} = \frac{G_{MIX}}{L_{LPF}} \tag{4.54}$$

The contribution of amplitude and phase noise of local oscillator can be evaluated by means of (4.35-4.36) and (4.20-4.21), respectively; the signal power P_{BB} in these formulae (at the LPF output) is embodied in (4.55):

$$P_{BB} = P_{TX}\frac{G_{AMP}}{L_{CAB}}G_{SYS} \tag{4.55}$$

The noise of LF signal path P_{nLF} is referred to Z_0 impedance at the filtered down-converter outputs (Fig. 4.9, plane A). Usually, in these planes (behind LPFs) 50 ohm impedance matches the paths end, and is followed by voltage amplifiers (Fig. 4.6). That is why it can be advantageous to refer LF noise of LF amplifiers to their inputs, see the equation describing LF amplifier noise voltages and currents:

$$V_{nLF} = \sqrt{B_n\left[e_n^2 + e_{nR}^2 + (i_nR_{eq})^2\right]} \tag{4.56}$$

where e_n constitutes the input noise voltage of given OA (the value being stated in [nV.Hz-1/2]) and i_n refers to the input noise current of given OA (stated in [pA.Hz$^{-1/2}$]). e_{nR} is the noise voltage generated by feedback resistors.

This plane (marked A in Fig. 4.9) is defined as noise calculation plane, where all inner noise sources can be summed. There, the P_{nT} total noise power can be calculated as:

$$P_{nT} = P_{nA} + P_{nP} + P_{nRF} + P_{nLF} \tag{4.57}$$

The relation between V_i noise voltage and P_i noise power is in line with formula (4.58).

$$P_{nT} = \frac{V_{nT}^2}{R_0} \tag{4.58}$$

4.7.2 Calculated Noise

The values of parameters used in both measurement set-up and calculations are indicated in Tab. 4.5. The calculations were made for two different B_n noise bandwidths reaching 9 and 159 kHz, which correspond to processing of both narrowband and more broadband CW-type radar signals.

Parameter	Description	Value	Unit
T_0	ambient temp.	300	K
f_L	low frequency limit (BB)	1	kHz
f_H	high frequency limit (BB)	10/160	kHz
B_n	noise bandwidth	9/159	kHz
P_{TX}	transmitted power (DRO/PLL VCO)	13/19	dBm
L_{DEL}	delay line total loss	57	dB
G_{AMP}	gain of compensating amps	49.5	dB
F_{AMP}	noise figure of compensating amps	2.7	dB
G_{MIX}	mixer gain	10	dB
F_{MIX}	mixer noise figure	10	dB
L_{LPF}	LP filter loss	1	dB
A_{LF}	voltage gain of LF block	71	dB

Tab. 4.5 Parameters of measurement set-up components.

The results of noise parameters calculations caused by RF signal path are summarized in Tab. 4.6. To compare the calculations with measured results, V_{nRF} and V_{nRFO} filtered noise voltages at noise calculation plane and ADC input respectively are also presented.

$\boldsymbol{Bn}$ [kHz]	$\boldsymbol{P_{nRF}}$ [W]	$\boldsymbol{V_{nRF}}$ [mV]	$\boldsymbol{V_{nRFO}}$ [mV]
9	0.99e-12	7.0e-3	25.0
159	17.5e-12	29.6e-3	105

Tab. 4.6 Calculated noise parameters caused by RF signal path.

The noise voltages corresponding to LF signal path are presented in Tab. 4.7. V_{nLF} stands for LF circuits noise recalculated to point A in Fig. 4.9, V_{nLFO} symbolizes the voltage of identical noise at point B.

$\boldsymbol{Bn}$ [kHz]	$\boldsymbol{V_{nLF}}$ [mV]	$\boldsymbol{V_{nLFO}}$ [mV]
9	1.2e-4	0.5
159	5.3e-4	1.7

Tab. 4.7 Calculated noise voltages corresponding to LF signal path.

The time-delay dependences of noise voltages are involved in Tabs. 4.8-4.9 (calculations) and Figs. 4.10 – 4.13 (calculations and measurement). Tabs. 4.8 and 4.9 show values of noise voltages corresponding to radar sensors equipped with DRO and PLL based local oscillators, respectively. The partial V_{nP}, V_{nA} voltages are referred to calculation plane A (Fig. 4.9). V_{nPO},

V_{nAO} voltages correspond to ADC inputs (calculation plane B), while V_{nTO} values stand for the maximum noise voltages at ADC inputs considering all noise sources (calculation plane B).

B_n [kHz]	τ [ns]	V_{nP} [mV]	V_{nA} [mV]	V_{nPO} [mV]	V_{nAO} [mV]	V_{nTO} [mV]
9	5	0.3e-3	5.4e-3	1.1	19.2	31.4
	48.1	3.0e-3	5.4e-3	10.8	19.2	33.3
	96.1	6.1e-3	5.4e-3	21.5	19.2	38.2
	144	9.1e-3	5.4e-3	32.3	19.2	45.1
159	5	1.3e-3	10.7e-3	4.7	37.9	112
	48.1	12.8e-3	10.7e-3	45.4	37.9	120
	96.1	25.6e-3	10.7e-3	90.7	37.9	144
	144	38.3e-3	10.7e-3	136	37.9	176

Tab. 4.8 DRO-based radar - calculated noise voltages caused by local oscillator amplitude and phase noise as function of time-delay and frequency bandwidth. Total noise voltage is presented in last column.

B_n [kHz]	τ [ns]	V_{nP} [mV]	V_{nA} [mV]	V_{nPO} [mV]	V_{nAO} [mV]	V_{nTO} [mV]
9	5	2.4e-3	3.6e-3	8.5	12.8	29.3
	48.1	23.0e-3	3.6e-3	81.5	12.8	86.2
	96.1	45.9e-3	3.6e-3	163	12.8	126
	144	68.8e-3	3.6e-3	244	12.8	246
159	5	6.5e-3	15.1e-3	23.0	53.6	120
	48.1	62.4e-3	15.1e-3	221	53.6	251
	96.1	125e-3	15.1e-3	445	53.6	460
	144	188e-3	15.1e-3	666	53.6	677

Tab. 4.9 PLL-based radar - Calculated noise voltages caused by local oscillator amplitude and phase noise as function of time-delay and frequency bandwidth. Total noise voltage is presented in last column.

4.7.3 Noise Measurement Results

The radar system noise measurements were performed in a set-up according to Fig. 4.9. To eliminate the local oscillator noise, measurements with a disconnected cable (no crosstalk) were also conducted. The RMS noise voltages were calculated from data acquired by AD converters. Applying digital filtering enabled to calculate noise voltages separately for each considered B_n frequency bandwidth. To prevent aliasing in AD converters, analog low-pass filters with 160 kHz cutoff frequencies were used

All measured values for structures equipped with DRO and PLL based local oscillators are summarized in Tabs. 4.10 and 4.11. The calculated values are provided for easy comparison as well. Slightly different values for I and Q branches are attributable to somewhat different gains in I and Q branches, and mixer amplitude imbalance.

B_n [kHz]	τ [ns]	V_{nMO_I} [mV]	V_{nMO_Q} [mV]	V_{nTO} [mV]
9	5	29.5	31.1	31.4
	48.1	31.2	32.2	33.3
	96.1	35.1	35.4	38.2
	144	43.6	41.0	45.1
159	5	118	128	112
	48.1	121	133	120
	96.1	145	159	144
	144	169	180	176
9	no crosstalk	23.7	23.3	25.0
159	no crosstalk	125	135	105

Tab. 4.10 DRO-based radar – measured noise voltages as functions of τ and filter bandwidths B_n; comparison with theoretical values.

To provide better insight into the CW-type radar noise behavior, the calculated and measured results are also indicated as functions of time-delay τ in Figs 4.10 – 4.13. The measured noise voltages correspond to the V_{nT} total radar noise voltage, and were evaluated for four discrete τ values (5, 48.1, 96.1 and 144 ns) created by the combination of co-axial cable sections and variable phase-shifter. V_{nT} voltages are plotted separately for I and Q branches. All graphs also include estimated lower and upper V_{nT} limits. The limits were evaluated with respect to variations in insertion loss of the used variable phase shifter, mixer amplitude imbalance, amplitude imbalance of low frequency circuits and system gain uncertainties caused by system interconnects. To facilitate understanding of the resulting noise voltage dependences, the graphs also demonstrate the dependences of separate phase-noise, amplitude-noise and LF noise components.

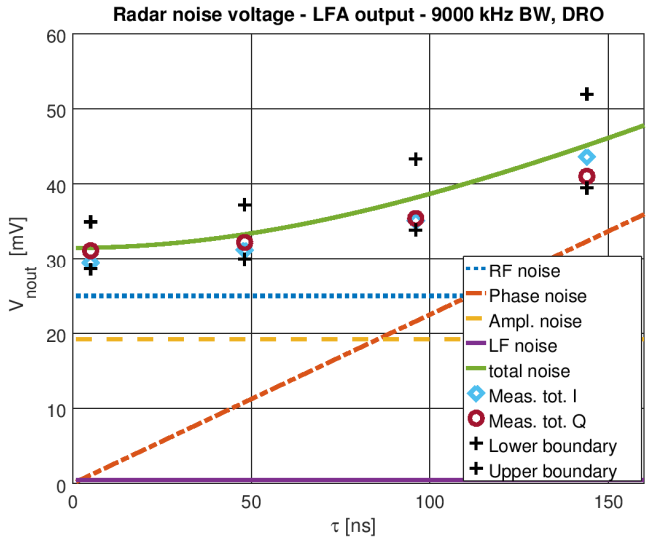

Fig. 4.10 DRO-based radar – calculated and measured noise voltages, 1–10 kHz BW.

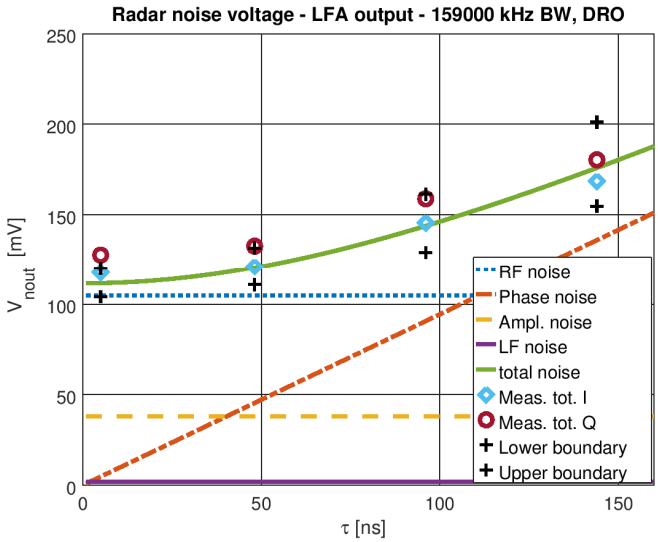

Fig. 4.11 DRO-based radar – calculated and measured noise voltages, 1–160 kHz BW.

B_n [kHz]	τ [ns]	V_{nMO_I} [mV]	V_{nMO_Q} [mV]	V_{nTO} [mV]
9	5	26.8	26.0	29.3
	48.1	91.1	79.5	86.2
	96.1	173	157	126
	144	224	213	246
159	5	110	120	120
	48.1	248	264	251
	96.1	468	483	460
	144	625	642	677
9	no crosstalk	23.7	23.3	25.0
159	no crosstalk	125	135	105

Tab. 4.11 **PLL-based radar – measured noise voltages as functions of τ and filter bandwidths B_n; comparison with theoretical values.**

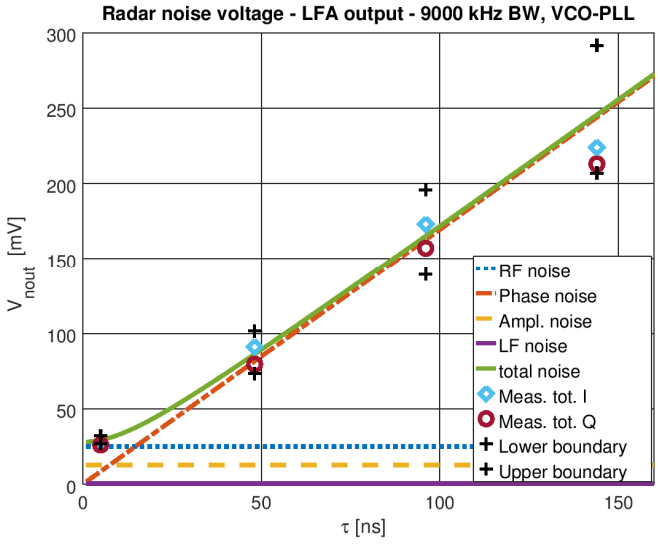

Fig. 4.12 **PLL-based radar – calculated and measured noise voltages, 1–10 kHz BW.**

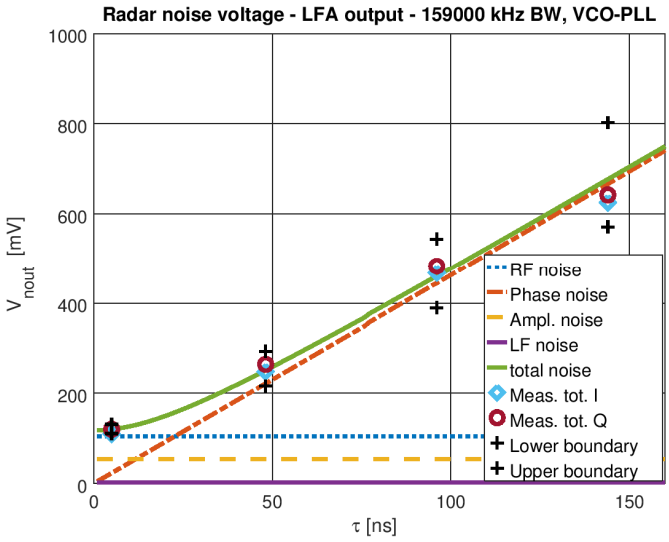

Fig. 4.13 PLL-based radar – calculated and measured noise voltages, 1–160 kHz BW.

The results presented above illustrate that the noise behaviors of CW-type radars equipped with of DRO and PLL local oscillators considerably differ. The DRO-based units show relatively high amplitude noises, which are independent of τ. Accordingly, if the frequency exceeds 1 kHz, they perform only a weak function of B_n noise bandwidth. That is why it can become a dominant noise source in the case of narrowband systems and low τ values. It can also be important in the case of low RF noise.

As the PLL-based units show very low amplitude noises, their noise behavior is dominated by RF noise and phase noise. Both radar types used for tests evince negligible LF noise. It is caused by the fact that both measurement set-ups employ low-noise LF amplifiers applying LT1028 operational amplifiers. These ICs belong to the best available (but also costly) low-noise amplifiers with $0.9\ \mu V / \sqrt{Hz}$ input noise voltage. Using standard cheaper OAs can lead to a significantly higher LF noise.

4.8 Use of Amplitude/Phase Noise in Self-test

The capability of self-test or malfunction detection is mandatory for almost all devices with the exception of some non-critical systems (for instance microwave door openers or low security grade combined uW/PIR sensors). As far as radar sensors are concerned, the overall functionality depends on non-fault operation of transmitter, receiver and corresponding antennas.

Though the malfunction transmitter is easy to detect (e.g. power detector coupled to transmission line close to TX antenna), the inspection of receiver represents a more complicated task. An input signal has to be injected, for the circuits are non-autonomous. The example of self-diagnostic

circuit benefiting from external injection of the testing signal can be found in [31]. However, this method requires additional costly components.

This chapter explains a self-test method exploiting the amplitude/phase noise measurement. It uses its own radar signal, existing cross-talk between antennas and its impact on radar noise parameters. In line with the statements made in Chapters 4.2-4.3, the amplitude noise power and phase noise depend on the time delay τ and the phase shift ψ between the reference and cross-talked signals. The amplitude noise usually overweighs the phase noise in the case of low τ. Therefore further explanation reckons upon amplitude noise (i.e. the major noise source has to be evaluated within the current system). The results using phase noise are similar, though.

Provided that the reference signal (4.22) involves the added phase ψ:

$$s_r(t) = A_r(1 - A_n(t))\cos(2\pi f_o t + \psi) \tag{4.59}$$

The resulting noise power related to amplitude noise leads to the modification of (4.34):

$$P_{nA} = 8P_{BB}\cos^2(2\pi f_o \tau + \psi)\int_{f_L}^{f_H}\cos^2(\pi f \tau)\left(b_0 + \frac{b_1}{f}\right)df \tag{4.60}$$

The total noise power is the sum of all noise sources (4.41). As for voltages, (4.41) is transformed into (4.61):

$$V_{nT} = \sqrt{V_{nRF}^2 + V_{nLF}^2 + V_{nP}^2 + V_{nA}^2}\ . \tag{4.61}$$

Since both noise voltages V_{nP} and V_{nA} depend on τ and ψ, the total noise is also determined by τ and ψ. Assuming $P_{nP} >> P_{nA}$, we get equations of maximum and minimum noise voltages:

$$V_{nTM} = \sqrt{V_{nRF}^2 + V_{nLF}^2 + V_{nPM}^2 + V_{nAM}^2} \tag{4.62}$$

$$V_{nTm} = \sqrt{V_{nRF}^2 + V_{nLF}^2 + V_{nPM}^2} \tag{4.63}$$

where V_{nMT}, V_{nPM} and V_{nAM} represent respectively the maximum total noise voltage, maximum noise voltage due to phase noise and maximum noise voltage due to amplitude noise. V_{nTm} stands for the minimum total noise voltage. The phase noise power contribution is considered constant and equals to its maximum, because it impacts uniquely the minimum noise voltage.

4.8.1 Radar Self-diagnostic Circuit

The key principle of developed radar self-diagnostic method can be derived from equation (4.60). The proposed circuit is illustrated in Fig. 4.14.

The resulting noise voltage V_{nT} is the function of power P_{BB} (4.64), time delay τ of signal cross-talked from the transmitter to receiver as well as phase shift ψ between cross-talked signal and reference signal.

$$P_{BB} = P_{TX} G_{AA} G_{LNA} G_{MIX} / L_{LPF} \tag{4.64}$$

In (4.64) P_{TX} embodies the transmitted power and G_{AA} counts the cross-talk gain.

The voltage obviously consists of the constant component (4.63) and oscillating component that is proportional to V_{nA}. By inserting an additional variable phase-shifter (VPS) into the reference branch, it is possible to vary the phase shift ψ and find minima V_{nTm} and maxima V_{nTM} of $V_{nT} = f(\tau,\ \psi)$. Furthermore, additional important parameters such as maximum receiver noise figure can be calculated:

$$F_{RXM} = \frac{V_{nTM}^2 L_{LPF}}{kT_0 R_0 B_n G_{LNA} G_{MIX}} \tag{4.65}$$

To enable self-test in the case that moving objects are present in radar range, the system is equipped with a pair of switches and attenuator, which represents a reference (or test) cross-talk with gain G_{AAt}.

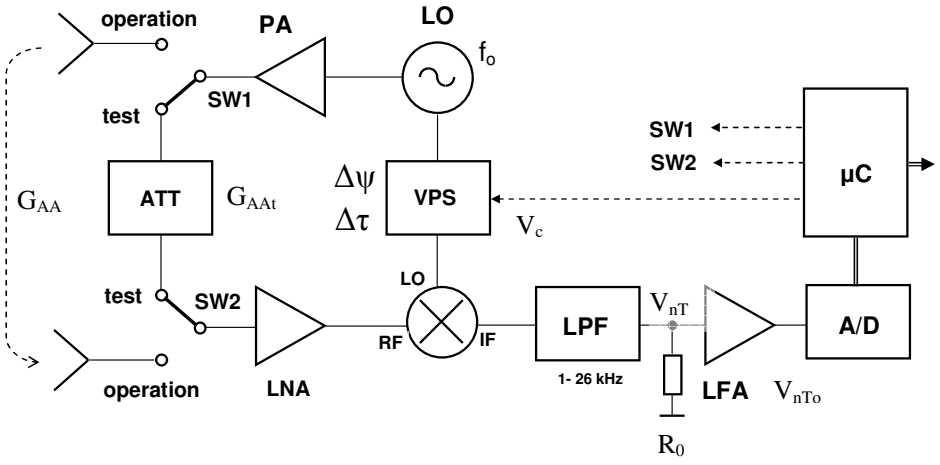

Fig. 4.14 Block diagram of radar front end with self-test circuit.

4.8.2 Self-diagnostic Circuit Measurement

The verification of proposed self-diagnostic method was tested via HMC931LP4E and HMC932LP4E (Hittite) VPSs. The states listed below that represent both radar correct operation and potential failures were simulated:

- Standard operation,
- 2 dB decrease in G_{AAt} test branch gain carried out by inserting the 2 dB additional attenuator at LNA input (fault in receiving branch),
- Total drop-out (TX-OFF) of the transmitter output power (fault in transmitting branch).

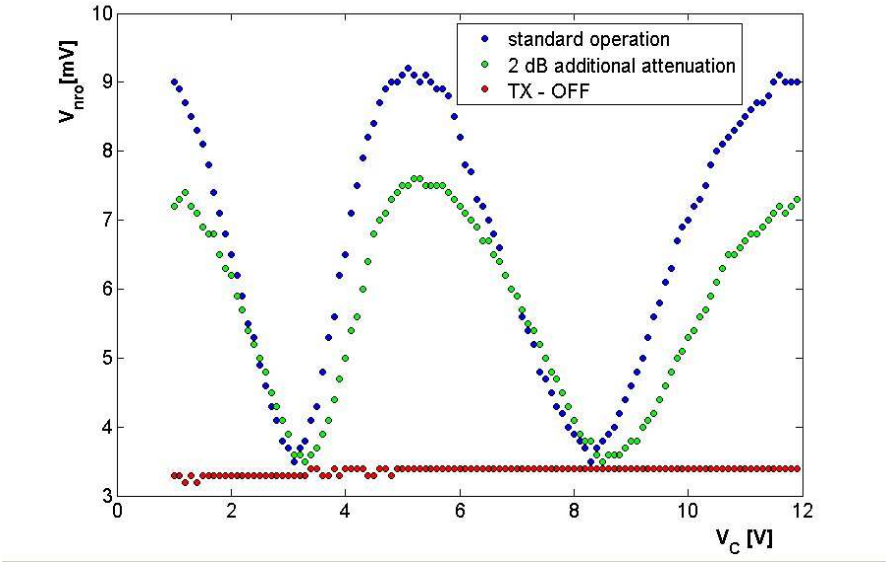

Fig. 4.15 CW radar measured $V_{nTo} = f(V_c)$ dependences.

Fig. 4.15 depicts the recorded $V_{nTo} = f(V_c)$ dependences ($V_{nTo} = A_{LF}\, V_{nT}$, where A_{LF} symbolizes the voltage gain of low frequency amplifier). In case of the standard operational state, the graph shows the expected oscillating behavior. The minimum noise figure $F_{RXm} = 2.49$ dB was calculated from the read value $V_{nTmo} = 3.5$ mV, which matches up with the expected 2.58 dB. The maximum $F_{RXM} = 13.8$ dB corresponds to the maximum noise voltage $V_{nTMo} = 9.2$ mV.

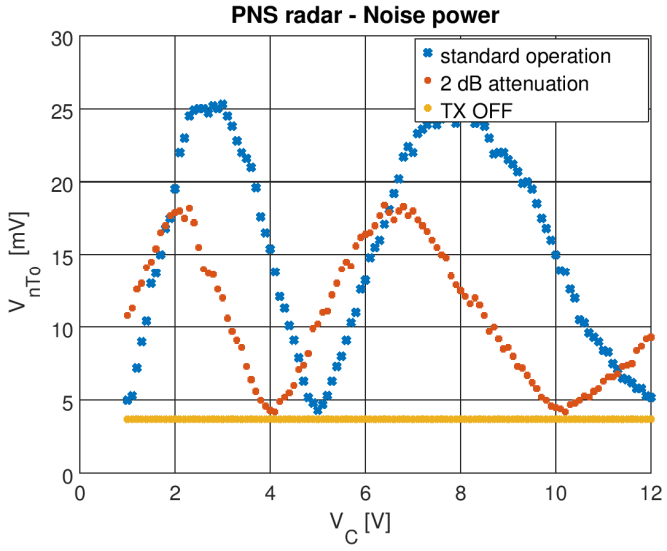

Fig. 4.16 PNS CW radar measured $V_{nTo} = f(V_c)$. Standard operation, attenuation in receiving branch, drop-out of transmitted power.

The 2 dB increase in LNA noise figure is caused by the connection of 2 dB attenuator in front of LNA and results primarily in P_{BB} decrease. As a consequence, the amplitude swing of $V_{nTo} = f(V_c)$ oscillations also diminishes. Yet the performed F_{RF} calculations lead to 4.51 dB value, which is close to the expected 2 dB increase. The simulated drop-out of transmitter output power makes the constant $V_{nTo} = f(V_c)$ dependence equal to zero local oscillator noise.

The effect of phase noise was measured on PNS CW radar as well with similar results (see Fig. 4.16). Even though the PNS CW radar is more complex structure, the behavior is similar to simple CW radar.

4.9 Conclusion

Chapter 4 yields complex analysis of all inner noise sources in a structure with IQ signal processing. The considered noise sources include local oscillator phase-noise, local oscillator amplitude noise, noise of linear or quasi-linear components in the RF signal path and noise of the LF signal path. Based on detailed description of all these sources, a complex radar noise model was created and verified.

The models shows, that with regards to radar bandwidth and amplitude and phase noise of local oscillator, the amplitude noise dominates the phase noise for low time delays (below tens of ns). Aside amplitude noise, which maximum is constant for changes in time delay, the phase noise magnitude is increasing with τ. Minima of amplitude or phase noise could be found in single channel base band radars to suppress total noise, which is not available in systems with quadrature demodulation.

It was shown in Chapter 4.8 that amplitude and phase noise can be used for automated radar system self-test adding only simple components.

The behavior of more complex structure of PNS radar let us suppose that the total noise due to amplitude or phase noise of all local oscillators (including PNS generator) can be neglected aside the local oscillator with the highest amplitude/phase noise PSD; this is usually the one with the highest frequency.

This topic should be subjected to further research to provide detailed description of the noise behavior of heterodyne systems and systems with additional PNS modulation.

5 Conclusion

The thesis was focused on CW radar systems for detection of fast-moving targets in a short range that equals to (given the intended application) tens of meters, which is demanding in terms of the utilized radar system, especially its zero blind zone. Hence mainly CW radars were considered. Although the research was primarily focused on methods for military use, the results are applicable in many other radar based systems (e.g. automotive industry).

The main theoretical and experimental developments in area of microwave radar sensors are listed below:

- **Multisensor Microwave Radar Systems**

  Since the employment of a simple microwave radar cannot provide sufficient information for impact point or target trajectory estimation, various impact point detection methods and system concepts using more radar sensors were proposed and verified.
  The first method for calculating the target impact point uses Doppler frequencies from more radar sensors (Chapter 2.2). Although it provides good theoretical results, the practical limitation lies in the frequency resolution and Doppler frequency spreading effect in the case of long targets (e.g. missiles).
  The dual level microwave curtain concept proposed in Chapter 2.3 can gather more information about detected targets. The system is capable of calculating various target parameters (velocity, trajectory elevation and vertical position of impact point) and can be used for identification of target category (e.g. bullet, missile…). Utilizing a PNS modulated CW radar and leaky-wave antennas (Chapter 2.4), this concept can be applied as adaptable microwave radar sensor with many capabilities. Firstly, it can function in the surveillance radar mode that is able to measure the target velocity and distance. The system combining at least two of such sensors is able to provide 2-D target tracking (using PNS modulation and scanning capabilities of leaky wave antenna). Secondly, the system can compensate for vehicle tilt in MC configuration. Last but not least, the dual level MC configuration is available with additional capability as well, so it is possible to measure directly the vertical impact point (again, via PNS modulation).
  Chapter 2.5 presented coherent multi-input radar for SDR based estimation of target azimuth; two radars of this kind provided 2-D target tracking, which was verified experimentally.

- **In-field Calibration of Radar Systems**

  As there was a need for testing and calibrating the radar sensors in field, Chapter 3 investigated available methods for this purpose. Various methods (rotating helix, moving reflector) were considered and their advantages and limitations were evaluated. The selected solution benefits from the antenna with electronically controlled phase shifter and

short-end stub (together behaving as a reflector with modulated phase shift). The solution was verified by two types of radar sensors (CW radar sensor and PNS modulated CW radar sensor) and provided the expected results.

- **Comprehensive Noise Analysis**

  Chapter 4 yields a detailed analysis of all inner noise sources in a structure with IQ signal processing. The considered noise sources include local oscillator phase-noise, local oscillator amplitude noise, noise of linear or quasi-linear components in the RF signal path and noise of LF signal path.
  A complex radar noise model was created and verified by measurements; different time-delay τ values between received and reference signals, and different noise bandwidths were considered. Besides, the second experiment considered two different local oscillators (DRO and VCO with PLL).
  The performed measurements confirmed that the developed noise model corresponded well to real radar circuits. Additional measurements on PNS modulated CW radar verified that the analysis can be extended to more complex radar sensors.
  Based on the properties of amplitude noise, the radar self-test method was designed and verified, which included all components in TX and RX chain.
  The presented noise analysis can be used in many other radar systems, including wide-spread automotive radar sensors.

As far as the target detection is concerned, further research should be focused on PNS radar systems, which can provide additional information about target (velocity and range), and more detailed description of target behavior regarding electromagnetic waves.

Follow-up research in the field of noise analysis should be focused detailed noise analysis of heterodyne systems and systems with PNS modulation in order to extend the noise analysis to SDR based radars.

6 References

[1] R. M. Ogorkiewicz, "Active Protection Systems Penetrate the Armoured Vehicle Market," *Jane´s International Review*, Vol. 44, October 2011, ISSN 1476-2129.

[2] P. Hudec, K. Hoffmann, M. Randus, M. Rynes, J. Raboch, M. Svanda, M. Polivka, "Radar Sensor for Detection of Anti-Armour Missiles," *European Radar Conference EuRAD 2008*, Amsterdam, pp. 116-119, 30-31 Oct. 2008.

[3] P. Hudec, J. Raboch, M. Randus, K. Hoffmann, A. Holub, M. Svanda, M. Polivka, "Microwave Radar Sensors for Active Defense Systems", *Proc. EuRAD Conf.*, Rome, 2009, pp. 116-119, ISBN 78-1-4244-3794-8.

[4] P. Hudec, J. Plasil, P. Dohnal, "Digital Signal Processing Applied to Radar Sensors Operated in Active Defense Systems," *European Radar Conference EuRAD 2010*, Paris. pp. 483-486, Sept. 30 2010-Oct. 1 2010.

[5] M. J. Lazarus, F. R. Pantoja and M. G. Somekh, "New Moving Target Simulators for Doppler Radar," *Electronic Letters*, Vol. 17, No. 1, pp. 48-49, Jan. 1981.

[6] Li Dun Fu,; Duan, Wu: A Compact Ka Band CW Doppler Radar with High if and its System Noise Analysis, *19th European Microwave Conference, 1989*, pp. 300-304, 4-7 Sept. 1989 doi: 10.1109/EUMA.1989.333980.

[7] J. J. Bussgang, P. Nesbeda, H. Safran, "A Unified Analysis of Range Performance of CW, Pulse, and Pulse Doppler Radar," *Proceedings of the IRE*, Vol. 47, No. 10, pp. 1753-1762, Oct. 1959 doi: 10.1109/JRPROC.1959.287110.

[8] Tsai-Hwa Chen: "FM/AM Noise Test Set for a Pulsed Doppler Radar," *IEEE Transactions on Aerospace and Electronic Systems*, Vol. AES-19, No. 6, pp. 788-794, Nov. 1983 doi: 10.1109/TAES.1983.309390.

[9] J. F. i. Ventura, H. Russchenberg, "Improvement of the Performance of FM-CW Radar Systems by using Direct Digital Synthesizers: Comparison with Voltage Controlled Oscillators," *International Radar Symposium 2006*, IRS 2006, pp. 1-4, 24-26 May 2006 doi: 10.1109/IRS.2006.4338068.

[10] M. C. BUDGE Jr. and M. P. BURT, "Range Correlation Effects in Radars," *Record of the 1993 IEEE National Radar Conference 1993*, Lynnfield, MA, USA, 1993, pp. 212-216. doi: 10.1109/NRC.1993.270463.

[11] M. C. BUDGE and M. P. BURT, "Range Correlation Effects on Phase and Amplitude Noise," *Proceedings., IEEE Southeastcon '93*, Charlotte, NC, 1993, pp. 5 p.-. doi: 10.1109/SECON.1993.465731.

[12] K. SIDDIQ, R. J. WATSON, S. R. PENNOCK, P. AVERY, R. POULTON AND B. DAKIN-NORRIS, Phase noise analysis in FMCW radar systems, 2015 European Radar Conference (EuRAD), Paris, 2015, pp. 501-504. doi: 10.1109/EuRAD.2015.7346347

[13] P. Bezoušek, P. Šedivý, "Radarová technika," 1st edition. Prague: ISBN 8001030369, CTU, Prague 2004.

[14] D. Gabor, “Theory of communication. Part 3: Frequency compression and expansion,” *Journal of the Institution of Electrical Engineers - Part III: Radio and Communication Engineering*, Vol. 93, No. 26, pp. 445-457, November 1946. doi: 10.1049/ji-3-2.1946.0076

[15] F. Kozak, M. Capek, V. Jenik, P. Hudec, Z. Skvor, “Simulation of Electromagnetic Field of a Fast Moving Target Close to Antennas,“ *Proc. 7th EUCAP Conf.* Gothenburg, 2013, pp. 286-290, ISBN 978-88-907018-3-2.

[16] F. Kozak, V. Jenik, J. Machac, P. Hudec, “Microwave Radar Sensor Based on CRLH SIW Leaky-Wave Antennas”, *Proc. 11th EuRAD Conf.* London: Horizon House Publications, 2014, pp. 53-56, ISBN 978-2-87487-034-7.

[17] R. C. Johnson, “Antenna Engineering Handbook“, *McGraw-Hill 1993*, ISSN 1063-665X.

[18] V. Jenik, P. Hudec, “Microwave multi-sensor system for estimation of positions of fast-flying objects,” 6th European Conference on Antennas and Propagation EuCAP 2012; ISBN 978-1-4577-0918-0; CZ, Prague 2012.

[19] A. Holub, M. Polivka, “Multiport Network Modeling of a Complex Canonically Shaped Patch Antenna*,” The Second European Conference on Antennas and Propagation. EuCAP 2007*, Vol., No., pp. 1-5, 11-16 Nov. 2007.

[20] Z. Chen, G. Gokeda, and Y. Yu, “Introduction to direction-of-arrival estimation,” *Artech House*, 2010, ISBN 13: 978-1-59693-089-6.

[21] K.R. Dandekar, Ling Hao, Xu Guanghan, “Smart antenna array calibration procedure including amplitude and phase mismatch and mutual coupling effects,” IEEE International Conference on Personal Wireless Communications, 2000, pp.293-297, 2000.

[22] L. Bin, L. Guisheng, “Method for array gain and phase uncertainties calibration based on ISM and ESPRIT,” *Jurnal of Systems Engineering and Electronics*, Vol.20, No.2, pp. 223-228, Apr. 2009.

[23] G. Welsh, G. Bishop, “An Introduction to the Kalman Filter” [on-line]. [2012-11-01] Available at: <http://www.cs.unc.edu/~welch/kalman/kalmanIntro.html>.

[24] M. J. Underhill, “Fundamentals of Sscillator Performance,” *Electronics & Communication Engineering Journal*, Vol.4, No.4, pp. 185-193, Aug. 1992.

[25] U. L. Rohde, D. P. Newkirk, “RF/Microwave Circuit Design for Wireless Applications,” pp. 832. *John Wiley and Sons*, 2000, ISBN: 0471298182, 9780471298182.

[26] A. Hajimiri and T. H. Lee, ”A general theory of phase noise in electrical oscillators,” *IEEE Journal of Solid-State Circuits*, Vol. 33, No. 2, pp. 179-194, Feb 1998. doi: 10.1109/4.658619

[27] A. Demir, A. Mehrotra and J. Roychowdhury, ”Phase noise in oscillators: A Unifying Theory and Numerical Methods for Characterization,” *IEEE Transactions on Circuits and Systems I: Fundamental Theory and Applications*, Vol. 47, No. 5, pp. 655-674, May 2000. doi: 10.1109/81.847872

[28] T. H. Lee and A. Hajimiri, “Oscillator phase noise: a tutorial,” *IEEE Journal of Solid-State Circuits*, Vol. 35, No. 3, pp. 326-336, March 2000. doi: 10.1109/4.826814

[29] Linear Technology. LT1028/LT1128 Ultra Low Noise Precision High Speed Op Amps, [on-line]. [2011-06-01] Available at <http://cds.linear.com/docs/Datasheet/1028fa.pdf>.

[30] Jenik V., Hudec P., Panek P.: Noise Parameters of CW Radar Sensors Used in Active Defence Systems," *Radioengineering, 2012*, Vol. 21, No. 2, pp. 632-639, ISSN 1210-2512.

[31] Schnabel R., Steinbuch D., Weigel R.: An ISO26262 Compliant Built-in Self-Test for 77 GHz Automotive Radar Sensors, in Proceedings of the European Microwave Conference EuRAD, pp. 216-2919, Nurmberg October 2013.

List of Candidate's Publications

Publications Related to the Thesis

Publications in Impacted Journals

V. Jenik, P. Hudec, P. Panek, "Noise Parameters of CW Radar Sensors Used in Active Defence Systems," *Radioengineering*, Vol. 21, No. 2, pp. 632-639, ISSN 1210-2512, 2012.

P. Hudec; P. Panek; V. Jenik, "Multimode Adaptable Microwave Radar Sensor Based on Leaky-Wave Antennas," *IEEE Transactions on Microwave Theory and Techniques* , Vol. PP, No. 99, pp. 1-10; doi: 10.1109/TMTT.2017.2653104.

One publication is in a review process:

V. Jenik, P. Hudec, P. Panek, "Extended Noise Analysis Model of CW-type Radar Sensors with IQ Down-Conversion," *Radioenginnering*.

Other publications

V. Jenik, P. Hudec, "Missile Measurement and Identification," *21st International Conference Radioelektronika 2011*; ISBN 978-1-61284-325-4; CZ, Brno, 2011.

V. Jenik, P. Hudec, "Design and Testing of Multi-Sensor Radar Microwave Curtain," *The 8th European Radar Conference EuRAD*; ISBN 978-1-4577-1156-5; UK, Manchester, 2011.

V. Jenik, P. Hudec, "Measurement of Noise Parameters of CW Radar Sensors*," 78th ARFTG Microwave Measurement Symposium*; ISBN 978-1-4673-0281-4; USA, AZ, Tempe, 2011.

V. Jenik, P. Hudec, "Microwave multi-sensor system for estimation of positions of fast-flying objects," *6th European Conference on Antennas and Propagation EuCAP 2012*; ISBN 978-1-4577-0918-0; CZ, Prague, 2012.

V. Jenik, F. Kozak, P. Hudec, "MISO Radar for Detection and Tracking of Fast-Flying Objects," *The 9th European Radar Conference EuRAD*, pp. 99-102; ISBN 978-1-4673-2471-7; Amsterdam, 2012.

V. Jenik, Z. Plhak, P. Hudec, P. Cerny, "Digitally-controlled calibrator for measurement and testing of CW Doppler radars," *European Microwave Conference (EuMC) 2013*, Vol., No., pp. 1283 - 1286, Nurmburg 6-10 Oct. 2013

V. Jenik, F. Kozak and P. Hudec, "Mutli-sensor surveillance radar based on MISO sensors and Kalman filtration,"European Radar Conference (EuRAD) 2013, Nuremberg, 2013, pp. 523-526.

F. Kozak, V. Jenik, J. Machac, P. Hudec, “Microwave Radar Sensor Based on CRLH SIW Leaky-Wave Antennas”, *11th European Radar Conference (EuRAD) 2014*, Vol., No., pp. 8-10, 53, 56, Roma 5-10 Oct. 2014, doi: 10.1109/EuRAD.2014.6991205.

Cited in:

S. Gruszczynski, A. Rydosz, J. Sorocki, I. Slomian, P. Kaminski and K. Wincza, "Leaky-wave antenna in multilayer structure for sensor applications," *2015 International Symposium on Antennas and Propagation (ISAP)*, Hobart, TAS, 9-12 Nov. 2015, pp. 1-4. ISBN: 978-4-8855-2302-1
URL: http://ieeexplore.ieee.org/stamp/stamp.jsp?tp=&arnumber=7447315&isnumber=7447267

Patents

P. Hudec; V. Jenik, CW Radar Sensor with Additional Funcitonal. Czech Republic. Patent Application. CZ. PV 2011-727.

Publications Not Related to the Thesis

F. Kozak, M. Capek, V. Jenik, P. Hudec, Z. Skvor, Simulation of Electromagnetic Field of a Fast Moving Target Close to Antennas, *The 7th European Conference on Antennas and Propagation (EuCAP)*, page 294 – 298; ISBN 978-1-4673-2187-7, SWE, Gothenburg, 2013.